

## On hydrogen penetration into ruthenium

***Citation for published version (APA):***

Onwudinanti, C. (2021). *On hydrogen penetration into ruthenium: The role of tin in blistering of EUV mirrors*. Eindhoven University of Technology.

***Document status and date:***

Published: 08/09/2021

***Document Version:***

Publisher's PDF, also known as Version of Record (includes final page, issue and volume numbers)

***Please check the document version of this publication:***

- A submitted manuscript is the version of the article upon submission and before peer-review. There can be important differences between the submitted version and the official published version of record. People interested in the research are advised to contact the author for the final version of the publication, or visit the DOI to the publisher's website.
- The final author version and the galley proof are versions of the publication after peer review.
- The final published version features the final layout of the paper including the volume, issue and page numbers.

[Link to publication](#)

***General rights***

Copyright and moral rights for the publications made accessible in the public portal are retained by the authors and/or other copyright owners and it is a condition of accessing publications that users recognise and abide by the legal requirements associated with these rights.

- Users may download and print one copy of any publication from the public portal for the purpose of private study or research.
- You may not further distribute the material or use it for any profit-making activity or commercial gain
- You may freely distribute the URL identifying the publication in the public portal.

If the publication is distributed under the terms of Article 25fa of the Dutch Copyright Act, indicated by the "Taverne" license above, please follow below link for the End User Agreement:

[www.tue.nl/taverne](http://www.tue.nl/taverne)

***Take down policy***

If you believe that this document breaches copyright please contact us at:

[openaccess@tue.nl](mailto:openaccess@tue.nl)

providing details and we will investigate your claim.

# **ON HYDROGEN PENETRATION INTO RUTHENIUM**

**THE ROLE OF TIN IN BLISTERING OF EUV MIRRORS**

**CHIDOZIE ONWUDINANTI**

This research was carried out under project number T16010a in the framework of the Partnership Program of the Materials innovation institute M2i ([www.m2i.nl](http://www.m2i.nl)) and the Technology Foundation TTW ([www.stw.nl](http://www.stw.nl)), which is part of the Netherlands Organization for Scientific Research ([www.nwo.nl](http://www.nwo.nl)).



ISBN 978-94-6419-297-1

NUR 925

An electronic version of this dissertation is available from the TU Eindhoven library.

Cover: electron density (charge difference) on Ru surface with Sn & H adsorbed, created with VESTA software (<http://jp-minerals.org/vesta/en/>)

Printed by Gildeprint, The Netherlands Copyright © 2021 by C. Onwudinanti

# On hydrogen penetration into ruthenium

## The role of tin in blistering of EUV mirrors

### PROEFSCHRIFT

ter verkrijging van de graad van doctor aan de Technische Universiteit Eindhoven, op  
gezag van de rector magnificus prof.dr.ir. F.P.T. Baaijens, voor een commissie  
aangewezen door het College voor Promoties, in het openbaar te verdedigen op  
woensdag 8 september 2021 om 13:30 uur

door

Chidozie Onwudinanti

geboren te Umuahia, Nigeria.

Dit proefschrift is goedgekeurd door de promotoren en de samenstelling van de promotiecommissie is als volgt:

voorzitter: prof. dr. ir. G.M.W. Kroesen  
1<sup>e</sup> promotor: prof. dr. ir. J.M.V.A. Koelman  
2<sup>e</sup> promotor: prof. dr. G.H.L.A. Brocks  
co-promotor: dr. S.X. Tao  
leden: prof. dr. S. Calero  
prof. dr. J.W.M. Frenken (Universiteit van Amsterdam)  
prof. dr. K. Nordlund (University of Helsinki)  
dr. Y. Ferro (Aix-Marseille Université)  
dr. T.W. Morgan

Het onderzoek of ontwerp dat in dit proefschrift wordt beschreven is uitgevoerd in overeenstemming met de TU/e Gedragscode Wetenschapsbeoefening.

# SUMMARY

## ON HYDROGEN PENETRATION INTO RUTHENIUM

Across the world, in all areas of life, the demand for smaller, cheaper, and more powerful microprocessors is strong, and growing. The chip has progressed tremendously since its invention, approximately doubling transistor density every 18 months. This phenomenon is a consequence of continuous improvement in semiconductor fabrication techniques. Photolithography, the primary technique, is a process in which patterns are projected onto and fabricated on a substrate. A decisive factor in the size of features which can be reliably produced on a wafer is the wavelength of the light used. In general, shorter wavelengths allow smaller features sizes, and this has spurred the development of extreme ultraviolet (EUV) lithography.

EUV uses light with a wavelength of 13.5 nm, emitted by a tin plasma. The systems operate in near-vacuum, and the optical system uses multilayer mirrors, stacks of molybdenum and silicon layers capped with ruthenium. Hydrogen is used as a buffer gas, and together with the capping layer protects the mirror from tin plasma debris and other contaminants, and the hydrogen also reacts with contaminants on the surface, thus keeping the mirror clean.

The use of hydrogen has one important drawback. The light, small atom can pass through the top layer and accumulate at the interface between the ruthenium and the underlying layer. This accumulation results in the formation of blisters, bubbles of hydrogen gas under the surface. It has been observed that blistering is significantly more rapid when tin is present on the ruthenium surface. Blisters permanently reduce the reflectivity of the mirror, therefore understanding tin-facilitated blistering is of great importance to the operation and development of EUV technology. Atomistic computational modelling can be used to probe the interactions between tin and hydrogen atoms on the ruthenium surface, and the diffusion of hydrogen into ruthenium. In this dissertation, Density Functional Theory (DFT) and Molecular Dynamics (MD) are used to explore these interactions, to illuminate the effect of tin on the penetration of hydrogen through the ruthenium layer.

First-principles (DFT) calculations show that H adsorption on Ru is favourable, while on Sn it is not. The H<sub>2</sub> molecule tends to dissociate into separate atoms on the Ru surface. As blistering would be expected to start from H penetration through the surface, the energy barrier was tested in a number of different Sn-H configurations on the Ru surface. In all configurations with tin present, the energy barrier to H penetration into the Ru is reduced. When the diffusing H atom comes from an adsorbed stannane molecule, the

barrier is as low as 25% of the value without tin. An analysis of the bonding interactions shows electron transfer at the surface, from Sn to the more electronegative Ru and H. The accumulation of electrons at the surface explains the tendency towards lower energy states with H in the subsurface.

H solubility in Ru is low, as shown by positive energies of hydride formation. However, the formation of blisters filled with H<sub>2</sub> means that a significant number of H atoms pass through the Ru layer. An investigation of H diffusion in the region of Ru immediately beneath the surface shows that access to the H surface is limited, as the surface adsorption sites are rapidly saturated by atomic H above the surface. The adsorption of Sn enhances the site-blocking effect. Direct recombination with H adsorbed on the surface also faces a large energy barrier. The result is that subsurface H is more likely to diffuse to the opposite interface to form blisters.

The afore-mentioned effects were shown to occur with adsorbed Sn atoms or hydride molecules. The case with larger amounts of Sn has also been investigated, by looking at the nature of Sn deposition on the Ru surface, and the consequences for H diffusion. First it is shown that a single atomic layer of Sn forms readily on the Ru surface, bonding strongly with the substrate, with a preference to form three-dimensional islands after the first wetting layer. Thus the Stranski-Krastanov growth mode is demonstrated. Further calculations show that one layer of Sn allows H to pass through to the Ru surface and below, but multiple layers impede the progress of H. On the basis of these results, the conditions for H penetration can be summarised as follows: penetration is negligible through a clean Ru surface, since the energy barrier is high, but a Ru surface with Sn atoms, Sn hydrides, or a single Sn wetting layer will result in a lowering of the barrier to entry.

The transport of H through the Ru film is studied in a series of molecular dynamics simulations, for which an interatomic potential (force field) in the ReaxFF method was developed using first-principles data. Simulations of H transport were performed in three structures: pristine hexagonal close-packed Ru, Ru with a symmetric tilt grain boundary, and Ru with a twist grain boundary. Grain boundaries were shown to be very favourable for H occupation. The consequence is that diffusion trajectories lie mainly within the grain boundaries. The diffusion coefficients suggest that grain boundaries would cause slightly slower diffusion in bulk Ru at around room temperature. However, for the thin films used in EUV mirrors, tilt grain boundaries may provide paths for short-circuit diffusion.

In sum, the role of tin and tin hydrides in the formation of hydrogen-filled blisters in EUV mirrors is shown using atomistic modelling and simulation. Tin is shown to aid the transition of hydrogen from the surface to the subsurface of ruthenium. It also contributes to blocking the out-diffusion of hydrogen from the subsurface. The nature of tin deposition on ruthenium suggests that blister formation is favoured when a small amount of tin is present. The diffusion of hydrogen within the ruthenium film is governed by the number and nature of grain boundaries. These findings contribute to the

---

understanding of tin-aided blistering, and will guide the design and implementation of mitigation strategies for EUV lithography tools.



*To my parents, from whom I learned to strive.*

*Nne ewu na-ata igu, ụmụ ya a na-ele ya anya n'ọnu.  
(When the goat chews palm fronds, her kids watch her mouth.)*

Igbo proverb



# CONTENTS

<b>Summary</b>	<b>v</b>
<b>1 Introduction</b>	<b>1</b>
1.1 Photolithography . . . . .	2
1.2 Multilayer mirrors for EUV lithography . . . . .	3
1.3 Contamination of EUV optics . . . . .	5
1.4 Hydrogen-induced blistering . . . . .	7
1.5 Outline of the thesis. . . . .	8
References . . . . .	11
<b>2 Methods</b>	<b>15</b>
2.1 Density Functional Theory . . . . .	15
2.2 Molecular Dynamics . . . . .	19
References . . . . .	25
<b>3 Tin, the enabler – hydrogen diffusion into ruthenium</b>	<b>27</b>
3.1 Introduction . . . . .	28
3.2 Computational Methods . . . . .	29
3.3 Results . . . . .	32
3.4 Discussion . . . . .	43
3.5 Conclusions. . . . .	45
References . . . . .	46
<b>4 Hydrogen diffusion out of ruthenium — an <i>ab initio</i> study of the role of adsorbates</b>	<b>51</b>
4.1 Introduction . . . . .	52
4.2 Computational details . . . . .	53
4.3 Results . . . . .	54
4.4 Discussion . . . . .	59
4.5 Conclusion . . . . .	61
References . . . . .	62
<b>5 Tin deposition on ruthenium and its influence on hydrogen permeation</b>	<b>65</b>
5.1 Introduction . . . . .	66
5.2 Computational methods . . . . .	67
5.3 Results and Discussion . . . . .	68

---

5.4 Conclusion . . . . .	76
References . . . . .	77
<b>6 A molecular dynamics study of hydrogen diffusion in ruthenium</b>	<b>83</b>
6.1 Introduction . . . . .	84
6.2 Computational methods . . . . .	85
6.3 Results and discussion . . . . .	88
References . . . . .	99
<b>7 Conclusions and Outlook</b>	<b>109</b>
References . . . . .	113
<b>List of Publications</b>	<b>115</b>
<b>Acknowledgements</b>	<b>117</b>
<b>Curriculum Vitæ</b>	<b>119</b>

# 1

## INTRODUCTION

Of the myriad steps forward on the path of technological progress, few have been as consequential as the microchip. Since the development of the integrated circuit in the middle of the 20th century, the use of microchips has spread throughout the globe. Few endeavours remain, in the professional and personal spheres, in which devices with microprocessors are entirely absent. The relentless drive towards greater processing power and lower cost has brought about such profound change that the microchip is now an indispensable contributor to virtually all technological advancement.

The success of the microchip is a direct consequence of the decades-long trend known as Moore's Law: the observation and prediction by Gordon Moore, semiconductor expert, that transistor density on an integrated circuit doubles approximately every two years. Figure 1.1 shows nearly half a century of this phenomenon. Over the decades, the minimum feature size has shrunk from 1 micron to 10 nm, with a corresponding increase in the number of transistors which can fit onto each chip. Advances in semiconductor fabrication techniques, key among which is photolithography, have allowed the industry to keep progressing in step with the prediction. As a result, processing capacity and efficiency have continued to improve, even as cost has continued to trend downwards.

As they become smaller, more powerful, more efficient, the demand for chips continues to grow. After the rapid expansion in personal computing in the 1980s and 90s, the rise of the smartphone, as well as the emergence of wearable electronic devices, and the Internet of Things (IoT) ensure that the appetite for chips has not waned, but is expected to grow. Beyond the realm of consumer electronics, the convergence of machine learning, automation, embedded systems, etc, means that chips are ever more involved in fields ranging from agriculture to medicine. This means that there is tremendous interest in the development of semiconductor fabrication technologies which will satisfy

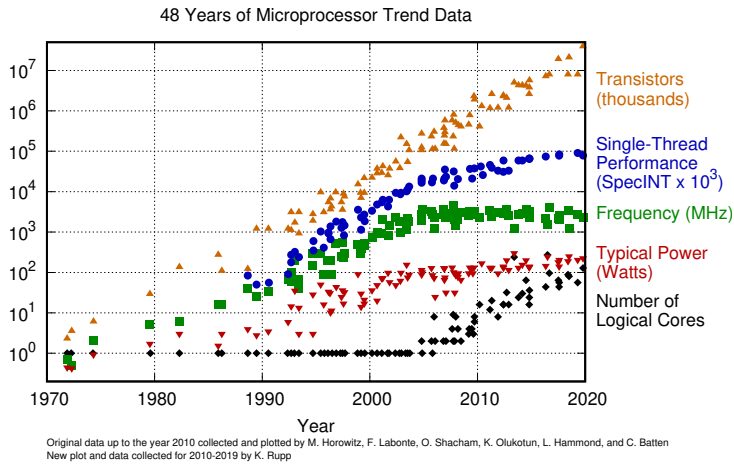


Figure 1.1: Microprocessor trends from 48 years of Moore's Law. Image reproduced with permission from Ref [1]

the demand.

This chapter introduces photolithography, and the latest evolution of the manufacturing technology for the next generation of microchips. A description is given of the multilayer mirrors used in the latest photolithographic machines. Finally, the main motivation for the research presented in this dissertation is explained, which is the problem of hydrogen-induced blistering of the mirrors.

## 1.1. PHOTOLITHOGRAPHY

The primary technique of microchip fabrication is photolithography. Photolithography is a process via which patterns are projected and fabricated on a substrate. Light, typically in the ultraviolet region, is used to transfer patterns from a photomask to a light-sensitive chemical photoresist on the substrate, also referred to as the wafer. Chemical treatments are then applied either to etch the pattern into the material or to allow deposition of a new material in the desired pattern on the material under the photoresist. These patterns can be extremely detailed and complicated. By repeating the exposure and treatment cycle many times, complex integrated circuits can be manufactured.

One of the most important measures of a lithography system's capability is its resolution. The resolution of an optical system is the minimum distance between objects at which they can still be distinctly reproduced separately. Beyond this limit, the image of the objects blur into one another. In a microprocessor, such blurring will lead to defective components and connections, which will result in a defective or inoperable product. The smallest features that can be reliably projected by a lithographic system are approx-

imately determined by the formula:

$$CD = k_1 \frac{\lambda}{NA} \quad (1.1)$$

where  $CD$  is the critical dimension (the smallest feature size),  $k_1$  is a coefficient determined by the manufacturing process,  $\lambda$  is the wavelength of the light used, and  $NA$  is the numerical aperture of the lens from the wafer. This equation shows the direct proportionality of the feature size and wavelength.

Until very recently, most of the enormous volume of microchip manufacturing was accomplished using deep ultraviolet (DUV) lithography, which uses laser sources of 248 and 193 nm wavelengths. Although sophisticated techniques such as immersion lithography and multiple patterning can improve feature density, shorter wavelengths eventually become necessary in order to make significant progress. As ultraviolet lithography reaches its technological limit, Extreme Ultraviolet (EUV) lithography has emerged as the leading technological solution to extend Moore's law[2, 3]. EUV systems use light with a wavelength of 13.5 nm. This short wavelength means that it is possible to achieve smaller features, and therefore greater transistor density than attainable by the 193 nm wavelength of the older argon fluoride laser systems.

## 1.2. MULTILAYER MIRRORS FOR EUV LITHOGRAPHY

Lithography is, at its core, a projection technique. The quality and accuracy of the fabricated pattern depends on precise control of the image projected onto the photoresist. The introduction of EUV entails a departure from the lens-based projection of DUV, because the short-wavelength high-energy EUV photons are readily absorbed by refractive optics, and even by air. For this reason, EUV requires near-vacuum conditions, and the optical system (Figure 1.2) consists entirely of reflective elements, i.e. mirrors.



Figure 1.2: Main chamber of EUV machine, with optical path highlighted. Image reproduced with permission from Ref [4].

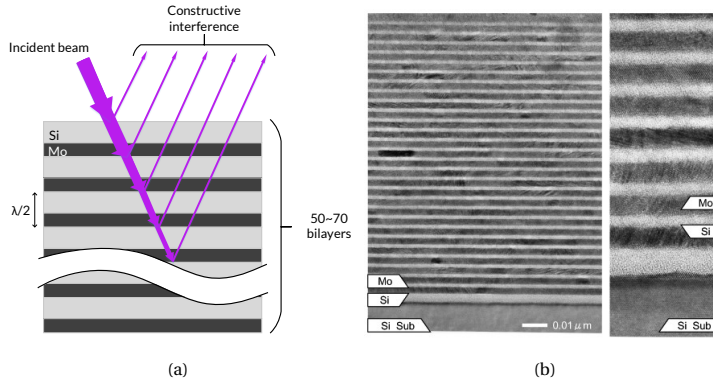


Figure 1.3: (a) Principle of operation of Bragg reflector and (b) cross-section of a multilayer mirror (MLM). Image reproduced with permission from Ref [5].

The reflective optical elements of EUV are multilayer mirrors (MLMs) which operate on the principle of constructive interference (Figure 1.3a), which results when the so-called Bragg condition is met. Bragg diffraction occurs when radiation undergoes specular scattering by the atoms of a crystal in such a way that the photons undergo constructive interference. This will occur when the wavelength of the incoming radiation is comparable to the spacing between layers of atoms in the crystal. The Bragg condition is:

$$2d \sin \Theta = n\lambda \quad (1.2)$$

where  $d$  is the spacing between atomic layers,  $n$  is the diffraction order (a positive integer),  $\Theta$  is the angle between the plane of atoms and the incoming radiation (glancing or grazing angle), and  $\lambda$  is the wavelength. With the cumulative effect of reflection from multiple layers of the crystal, the interference effect intensifies, reaching its peak for the wavelength/angle/spacing combination determined per Equation 1.2. For normal incidence ( $\Theta = \pi/2$ ), the condition is satisfied for a minimum spacing of half the wavelength,  $\lambda/2$ .

Each MLM consists of 50-70 molybdenum/silicon bilayers, approximately 7 nm thick. The alternating molybdenum and silicon layers have high and low refractive indices respectively. When the thickness of the alternating layers is selected accordingly for the required wavelength, the incident optical wave is partially reflected at each interface, and the numerous reflections undergo constructive interference. Thus together they form a Bragg structure which reflects a large part of the incident light.

A thin film of ruthenium serves as a capping layer[6, 7], to protect the bilayer stack from EUV- and plasma-induced damage, which we discuss in the following section. The molybdenum/silicon multilayer mirrors were initially terminated with silicon, which forms a thin stable oxide layer in air. Under good vacuum conditions, the multilayer mir-

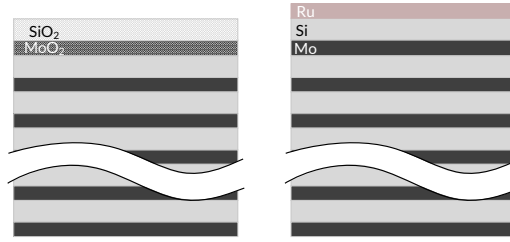


Figure 1.4: Silicon-terminated and ruthenium-capped multilayer mirrors.

irror terminated with silicon showed stable reflectivity after long-term exposure[8]. However, in tests simulating the EUV operating conditions of an unbaked vacuum, oxidation of the silicon layer was observed, as well as the underlying molybdenum. An ideal multilayer would be terminated with molybdenum, but the molybdenum layer was shown to oxidise completely to  $\text{MoO}_2$  and  $\text{MoO}_3$ , and to be susceptible to contamination by carbonaceous compounds[9]. Ruthenium thin films, on the other hand, are resistant to oxidation; they are also easily reduced in the event of oxidation of the surface[10]. A ruthenium-capped mirror was shown to have a lifetime 40 times that of a silicon-terminated one[6].

A number of exacting quality standards must be met by the mirrors. To achieve reflection as close as possible to the theoretical maximum of approximately 73%, the layers must be exceptionally smooth. The interfaces between the layers must be distinct, so the manufacture of the mirrors employs state-of-the-art deposition techniques and interlayers such as  $\text{B}_4\text{C}$  and  $\text{C}$ , which keep intermixing under control. Finally, the surface must be clear of contaminants, debris, and damage to keep losses in the optical path to a minimum. The optical chain shown in Figure 1.2 includes 10 mirrors, which means that a maximum of 4.3% will be delivered to the end of the chain with unblemished mirrors. This makes even minute losses in reflectivity very costly, and management of contamination crucial.

### 1.3. CONTAMINATION OF EUV OPTICS

Contaminants in the EUV system can come from a variety of sources. The chamber of the machine includes the entire optical system, as well as an array of sensors, actuators, etc. In the near-vacuum, outgassing from the numerous components, as well as volatiles produced during the operation of the machine contribute to a mixture of gases including oxygen, water, and hydrocarbons. Particulate contaminants such as silicon dioxide and aluminium dioxide may also be transported to surfaces in the chamber[11]. Under the EUV radiation, deposited molecules can decompose on the surface of the reflector, populating it with contaminants. Carbon is a leading contaminant, resulting from the decomposition of hydrocarbons[12–14].

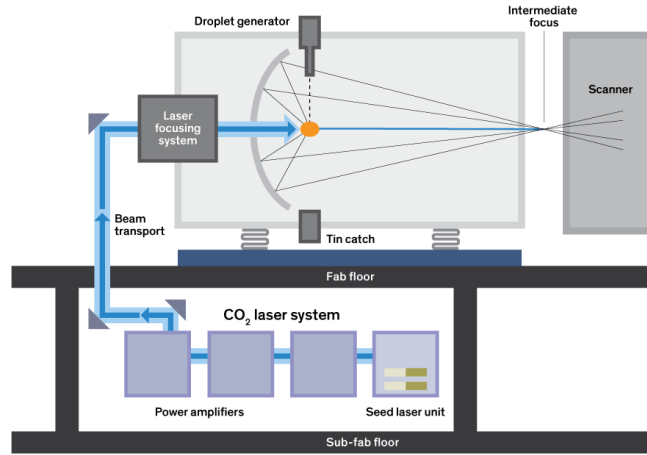


Figure 1.5: Schema of the tin-based laser-produced plasma (LPP) source. Image reproduced with permission from Ref [15]

The other important contaminant is tin, from the EUV source. Current EUV sources create light by exciting droplets of tin with a  $\text{CO}_2$  laser to generate a plasma[16]. The ionised Sn emits EUV photons which are then focused by a multilayer reflector, the collector. The plasma is a source of ions and particles with energies up to several keV. Surfaces in proximity are exposed to this flux, which can result in sputtering of the surface, implantation, or deposition. The result is a loss of reflectivity, should they occur on the multilayer reflector. Therefore techniques to minimise the number of particles reaching the surface must be deployed.

The current solution is the use of a buffer gas to shield the surface[17]. In EUV tools, hydrogen gas serves as the buffer; collisions with the gas molecules slow down the high-energy ions which can cause irreversible damage to the optics through sputtering or implantation. Furthermore, the neutral Sn atoms are also diverted, and are less likely to deposit on the optics. Nevertheless, some debris does successfully arrive at the mirror surface[18], and tin which is diverted from the mirror can deposit on other surfaces within the machine, whence it can be transported to other mirrors.

The accumulation of contaminants such as carbon and tin shortens the operational lifetime of the optical components, and leads to uneconomical outcomes due to stop-pages for maintenance and defective products. For this reason, cleaning of the optical system *in situ* is a necessary measure. Hydrogen also serves as a cleaning agent, supplying radicals which can etch away contaminants from the surface of the mirrors. Other cleaning media have been proposed, such as molecular oxygen, ozone, or oxygen plasma[19, 20], but atomic hydrogen[21, 22] has the advantage of removing carbon deposits efficiently, while also countering the oxidation of the optics.

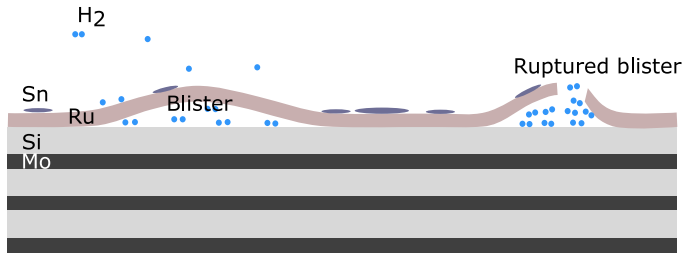


Figure 1.6: Hydrogen-induced blistering.

Compared to oxides and carbon, tin removal with hydrogen is more challenging. Much like the hydrocarbons formed when hydrogen reacts with the carbon, stannane ( $\text{SnH}_4$ ) is formed when tin is exposed to atomic hydrogen:



Stannane is volatile at room temperature, with a boiling point of 221 K. Furthermore, the molecule is quite unstable, and will decompose on chemically active surfaces to yield tin[23, 24]. It therefore acts as a vector of tin transport in the lithography tool[25]. A number of reasons have been proposed for the low efficiency of tin removal. Oxidation of the tin to  $\text{SnO}$  and  $\text{SnO}_2$  may be an obstacle to tin removal, as the oxide resists etching[26]. Previously etched tin may also be redeposited, leading to a lower rate of etching[27]. In general, etching of tin from a ruthenium surface was found to be incomplete[28]. In addition to the persistence of tin on ruthenium, the use of hydrogen comes with one important disadvantage: the presence of tin on the ruthenium surface spurs the development of hydrogen-filled bubbles under the ruthenium layer, referred to as “blisters”.

#### 1.4. HYDROGEN-INDUCED BLISTERING

Hydrogen-induced blistering refers to the formation of hydrogen-filled subsurface cavities in a material or structure. These cavities are generally undesirable, as they alter the properties of the metals and alloys in which they form, leading to a deterioration of their ability to fulfill their function. Although the exact mechanisms are still unclear, it is believed that blisters form when hydrogen interacts with defects in the host material or structure. This purportedly proceeds in the following manner: (i) hydrogen penetrates the surface and diffuses within the host material; (ii) due to its low solubility in the host material, it segregates into defects and voids, where it recombines to form molecular hydrogen; (iii) the accumulation of molecular hydrogen increases the pressure to the point of decohesion, and a blister is formed; (iv) further accumulation of hydrogen may lead to rupture of the blister[29]. For a ruthenium-capped mirror, the site of formation of the bubbles is usually at the interface between the ruthenium layer and the substrate.

Hydrogen, the lightest and smallest atom, poses a problem in other technological applications due to its ability to permeate through materials. For example, it can perme-

ate through steel, aluminium alloys, titanium, magnesium alloys, etc, and change their properties, leading to so-called hydrogen embrittlement[30]. Hydrogen can be introduced into a material via chemical means, for instance through a reaction or exposure to the gas, or through implantation, which occurs when high energy ions strike the material, for instance from a plasma[31]. Hydrogen is unique in this regard, because while penetration as a chemical process is uncommon for other gases, implantation is achievable with many different gases. For instance, helium ions have been shown to form blisters in tungsten blocks in nuclear fusion studies[32]. Implantation is also used in the ion-cutting process[33], to fabricate silicon heterostructures. In these examples, high energy ions ( $> 100$  eV) penetrate the surface and precipitate into bubbles in the near-surface region, due to the low solubility of hydrogen in the material. In MLMs, blister formation occurs under exposure to EUV-induced radicals at much lower energy levels than above, usually not exceeding 10 eV, and chemical interactions with the surrounding atomic species are of greatest relevance.

Although hydrogen-induced blistering has received a great deal of attention, questions remain about the exact way in which this process occurs in EUV conditions. Multilayer mirrors are thin-film heterostructures, and so differ quite significantly from bulk metals which have been studied extensively with respect to this phenomenon[34]. Blistering in mirrors has been shown to depend on such factors as temperature, ion energy, and mechanical strain[29, 35, 36], but these findings do not probe the effect of tin. Indeed, the focus has been primarily on the efficiency of tin removal. Direct study of blistering with experimental techniques is challenging, as the processes of interest occur at the atomic/molecular level. Computational techniques can shed light on the promotion of blistering by tin, and guide further experimental efforts and mitigation measures. Blisters cause permanent loss of reflectivity in EUV mirrors, reducing their operational lifetime. Since reflectivity loss of a few percent is sufficient to move the mirror out of specification[6], mitigation of the blistering process is of great importance. Therefore a thorough understanding is required of the steps via which hydrogen permeates through the ruthenium layer and accumulates at the interface in sufficient quantity to form the pockets of gas. An understanding of the mechanism of tin-facilitated blistering is the primary motivation for this research project.

## 1.5. OUTLINE OF THE THESIS

Due to the high cost of malfunctions and stoppages – millions of euro daily – it is critical to combat the blistering of the mirrors. It is equally important to be able to make confident estimates of the operating lifetime of each element, given its operating conditions, to minimise downtime. These concerns lead to the main research question tackled in this dissertation:

What are the mechanisms via which tin facilitates the blistering of ruthenium-capped multilayer mirrors?

Tracking the progress of hydrogen from the gas/plasma phase to the molecular state within the blisters leads to the following series of questions:

How does hydrogen enter the ruthenium film, and how does the presence of tin affect this phenomenon?

How does the amount and distribution of tin on the film affect the hydrogen penetration, and therefore the severity of blistering?

What is the nature of hydrogen transport through ruthenium?

Atomistic modelling and simulations, using the combination of Density Functional Theory (DFT) and Molecular Dynamics (MD), have been applied to seek answers to these questions. Within the framework of DFT, the Climbing Image Nudged Elastic Band (CINEB) algorithm, transition state searches have been carried out for relevant hydrogen adsorption, desorption, and diffusion on and in ruthenium, in the presence and absence of tin. An interatomic potential has been developed under the ReaxFF framework, which allows the study of larger ensembles at a fraction of the cost of quantum-mechanical models. Molecular Dynamics simulations in ReaxFF have been used to examine hydrogen transport in perfect ruthenium lattices and along grain boundaries. These computational approaches are described in detail in Chapter 2.

Chapter 3 tackles the question of hydrogen penetration into the ruthenium subsurface. It establishes the basic energies of hydrogen and ruthenium interaction on the surface and in the bulk, and discusses the energy barriers faced by hydrogen in migration between energy minima on and in ruthenium. Results of calculations for the interaction between hydrogen and tin are also presented. The effects of tin on the energy landscape on the ruthenium surface and on the key hydrogen penetration barrier are studied, showing that tin proximity results in a lower barrier to entry into Ru.

In Chapter 4, the subsequent diffusion of hydrogen in the ruthenium subsurface is explored. The cases for subsurface diffusion with and without tin present on the surface are studied, with the finding that a surface saturated with tin and hydrogen will inhibit diffusion of hydrogen out of the ruthenium. This shows the second aspect of tin-facilitated blistering, since saturation of surface sites is more likely with the difficult-to-etch tin.

Chapter 5 examines the nature of tin deposition on ruthenium. The growth mode of tin is shown to follow a layer-plus-islands pattern, in a fashion that allows ample hydrogen access to the ruthenium surface at lower coverages. The interaction of hydrogen with multiple layers of tin is modelled, showing that hydrogen permeation through thick layers of tin is unlikely, such that layers with thick tin layers will block hydrogen out, and not allow hydrogen penetration into the Ru beneath.

In Chapter 6, molecular dynamics simulations of hydrogen diffusion in ruthenium are reported. The simulations are conducted for intact bulk ruthenium crystals as well as for structures with grain boundaries. The results indicate that the nature and direction

of hydrogen diffusion in ruthenium are governed by the number and nature of grain boundaries in a given sample.

Chapter 7 summarises the results of the research and discusses the implications of the findings presented in this work, and explores the prospects of further research on its basis.

**REFERENCES**

- [1] K. Rupp, *42 Years of Microprocessor Trend Data*, (2018).
- [2] H. Meiling, V. Banine, P. Kurz, B. Blum, G. J. Heerens, and N. Harned, *The EUV program at ASML: an update*, Conference on Emerging Lithographic Technologies VII **5037**, 24 (2003).
- [3] V. Banine, *EUV Lithography: Historical perspective and road ahead*, (2014).
- [4] ASML, *Lithography Principles: Lenses and Mirrors*, (2021).
- [5] NTTAT, *NTTAT EUV Multilayer Mirrors*, (2021).
- [6] S. Bajt, H. N. Chapman, N. Nguyen, J. B. Alameda, J. C. Robinson, M. E. Malinowski, E. Gullikson, A. Aquila, C. Tarrío, and S. Grantham, *Design and performance of capping layers for EUV multilayer mirrors*, Proc. SPIE **5037**, 236 (2003).
- [7] S. Bajt, N. V. Edwards, and T. E. Madey, *Properties of ultrathin films appropriate for optics capping layers exposed to high energy photon irradiation*, Surface Science Reports **63**, 73 (2008).
- [8] D. P. Gaines, R. C. Spitzer, N. M. Ceglio, M. Krumrey, and G. Ulm, *Radiation hardness of molybdenum silicon multilayers designed for use in a soft-x-ray projection lithography system*, Applied Optics **32**, 6991 (1993).
- [9] J. H. Underwood, E. M. Gullikson, and K. Nguyen, *Tarnishing of Mo/Si multilayer x-ray mirrors*, Applied Optics **32**, 6985 (1993).
- [10] Y. B. He, A. Goriachko, C. Korte, A. Farkas, G. Mellau, P. Dudin, L. Gregoratti, A. Barinov, M. Kiskinova, A. Stierle, N. Kasper, S. Bajt, and H. Over, *Oxidation and reduction of ultrathin nanocrystalline Ru films on silicon: Model system for Ru-capped extreme ultraviolet lithography optics*, Journal of Physical Chemistry C **111**, 10988 (2007).
- [11] M. A. van de Kerkhof, A. Yakunin, V. Kvon, F. van de Wetering, S. Cats, L. Heijmans, A. Nikipelov, A. Lassise, and V. Banine, *Understanding EUV-induced plasma and application to particle contamination control in EUV scanners*, , 29 (2020).
- [12] K. Boller, R. P. Haelbich, H. Hogrefe, W. Jark, and C. Kunz, *Investigation of carbon contamination of mirror surfaces exposed to synchrotron radiation*, Nuclear Instruments and Methods In Physics Research **208**, 273 (1983).
- [13] T. Naito, M. Tadano, N. Terunuma, J. Urakawa, E. Nakamura, M. Hasumoto, H. Sakai, T. Shibuya, F. Sakai, H. Ohgaki, and N. Sei, *Investigation of carbon contamination on SR-irradiated devices*, Nuclear Instruments and Methods in Physics Research, Section A: Accelerators, Spectrometers, Detectors and Associated Equipment **527**, 624 (2004).

- [14] G. Kyriakou, D. J. Davis, R. B. Grant, D. J. Watson, A. Keen, M. S. Tikhov, and R. M. Lambert, *Electron impact-assisted carbon film growth on Ru(0001): Implications for next-generation EUV lithography*, *Journal of Physical Chemistry C* **111**, 4491 (2007).
- [15] R. Courtland, *Leading Chipmakers Eye EUV Lithography to Save Moore's Law*, (2016).
- [16] I. Fomenkov, D. Brandt, A. Ershov, A. Schafgans, Y. Tao, G. Vaschenko, S. Rokitski, M. Kats, M. Vargas, M. Purvis, R. Rafac, B. La Fontaine, S. De Dea, A. LaForge, J. Stewart, S. Chang, M. Graham, D. Riggs, T. Taylor, M. Abraham, and D. Brown, *Light sources for high-volume manufacturing EUV lithography: technology, performance, and power scaling*, *Advanced Optical Technologies* **6**, 173 (2017).
- [17] D. J. W. Klunder, M. M. J. W. van Herpen, V. Y. Banine, and K. Gielissen, *Debris mitigation and cleaning strategies for Sn-based sources for EUV lithography*, *Emerging Lithographic Technologies IX* **5751**, 943 (2005).
- [18] D. B. Abramenko, M. V. Spiridonov, P. V. Krainov, V. M. Krivtsun, D. I. Astakhov, V. V. Medvedev, M. Van Kampen, D. Smeets, and K. N. Koshelev, *Measurements of hydrogen gas stopping efficiency for tin ions from laser-produced plasma*, *Applied Physics Letters* **112** (2018), 10.1063/1.5025914.
- [19] M. E. Malinowski, P. A. Grunow, C. Steinhaus, W. M. Clift, and L. E. Klebanoff, *Use of molecular oxygen to reduce EUV-induced carbon contamination of optics*, in *Emerging Lithographic Technologies V*, Vol. 4343, edited by E. A. Dobisz (2001) pp. 347–356.
- [20] S. Graham, C. Steinhaus, M. Clift, and L. Klebanoff, *Radio-frequency discharge cleaning of silicon-capped Mo/Si multilayer extreme ultraviolet optics*, *Journal of Vacuum Science and Technology B: Microelectronics and Nanometer Structures* **20**, 2393 (2002).
- [21] S. Graham, Jr., C. A. Steinhaus, W. M. Clift, L. E. Klebanoff, and S. Bajt, *Atomic hydrogen cleaning of EUV multilayer optics*, *Emerging Lithographic Technologies VII* **5037**, 460 (2003).
- [22] H. Oizumi, A. Izumi, K. Motai, I. Nishiyama, and A. Namiki, *Atomic Hydrogen Cleaning of Surface Ru Oxide Formed by Extreme Ultraviolet Irradiation of Ru-Capped Multilayer Mirrors in H<sub>2</sub>O Ambience*, *Japanese Journal of Applied Physics* **46**, L633 (2007).
- [23] K. Tamaru, *The Thermal Decomposition of Tin Hydride*. *Journal of Physical Chemistry* **60**, 610 (1956).

- [24] A. Manhard, T. Schwarz-Selinger, M. Balden, T. Durbeck, H. Maier, and R. Neu, *Deuterium retention in solid and liquid tin after low-temperature plasma exposure*, Nuclear Fusion **60** (2020), 10.1088/1741-4326/aba801.
- [25] N. Faradzhev and V. Sidorkin, *Hydrogen mediated transport of Sn to Ru film surface*, Journal of Vacuum Science & Technology A: Vacuum, Surfaces, and Films **27**, 306 (2009).
- [26] D. T. Elg, G. A. Panici, S. N. Srivastava, and D. N. Ruzic, *Study of Sn removal processes for in-situ collector cleaning*, Extreme Ultraviolet (EUV) Lithography VII **9776**, 97760M (2016).
- [27] D. T. Elg, J. R. Sporre, G. A. Panici, S. N. Srivastava, and D. N. Ruzic, *In situ collector cleaning and extreme ultraviolet reflectivity restoration by hydrogen plasma for extreme ultraviolet sources*, Journal of Vacuum Science & Technology A: Vacuum, Surfaces, and Films **34**, 021305 (2016).
- [28] M. Pachecka, J. M. Sturm, R. W. E. van de Kruijs, C. J. Lee, and F. Bijkerk, *Electronegativity-dependent tin etching from thin films*, AIP Advances **6**, 075222 (2016).
- [29] R. A. Van Den Bos, V. Reshetniak, C. J. Lee, J. Benschop, and F. Bijkerk, *A model for pressurized hydrogen induced thin film blisters*, Journal of Applied Physics **120** (2016), 10.1063/1.4972221.
- [30] B. N. Popov, J.-W. Lee, and M. B. Djukic, *Hydrogen Permeation and Hydrogen-Induced Cracking*, in *Handbook of Environmental Degradation of Materials* (Elsevier, 2018) third edit ed., pp. 133–162.
- [31] J. B. Condon and T. Schober, *Hydrogen bubbles in metals*, Journal of Nuclear Materials **207**, 1 (1993).
- [32] Y. Ueda, J. Coenen, G. De Temmerman, R. Doerner, J. Linke, V. Philipps, and E. Tsitrone, *Research status and issues of tungsten plasma facing materials for ITER and beyond*, Fusion Engineering and Design **89**, 901 (2014).
- [33] B. Terreault, *Hydrogen blistering of silicon: Progress in fundamental understanding*, physica status solidi (a) **204**, 2129 (2007).
- [34] A. Turnbull, *Hydrogen diffusion and trapping in metals*, in *Gaseous Hydrogen Embrittlement of Materials in Energy Technologies* (Elsevier, 2012) pp. 89–128.
- [35] A. S. Kuznetsov, R. W. E. van de Kruijs, M. A. Gleeson, K. Schmid, and F. Bijkerk, *Hydrogen interaction with EUVL-relevant optical materials*, Journal of Surface Investigation. X-ray, Synchrotron and Neutron Techniques **4**, 563 (2010).

- [36] A. S. Kuznetsov, M. A. Gleeson, and F. Bijkerk, *Temperature dependencies of hydrogen-induced blistering of thin film multilayers*, *Journal of Applied Physics* **115**, 173510 (2014).

# 2

## METHODS

The computational tools used in this study are Density Functional Theory (DFT) and Molecular Dynamics (MD). DFT is a quantum-mechanical method of performing ground-state electronic structure calculations of many-body systems, such as atoms, molecules, and condensed phases. MD allows the study of a system's evolution in time, and complements the static calculations usually performed with DFT. This chapter details the computational approaches and tools.

### 2.1. DENSITY FUNCTIONAL THEORY

The primary tenet of quantum mechanics states that the totality of information about a system is contained in the wavefunction of the system, denoted by  $\Psi$ . The Schrödinger equation expresses the wavefunction of a quantum-mechanical system, and its general form describes the evolution over time of the wavefunction of a physical system:

$$i\hbar \frac{d}{dt} |\Psi(t)\rangle = \hat{H} |\Psi(t)\rangle \quad (2.1)$$

where  $t$  is time, and  $\hat{H}$ , the Hamiltonian operator, is an observable corresponding to the system's total energy. For systems in a stationary state, the time-independent equation is sufficient:

$$\hat{H}\Psi(\mathbf{r}_1, \mathbf{r}_2, \dots, \mathbf{r}_N; \mathbf{R}_1, \mathbf{R}_2, \dots, \mathbf{R}_M) = \tilde{E}\Psi(\mathbf{r}_1, \mathbf{r}_2, \dots, \mathbf{r}_N; \mathbf{R}_1, \mathbf{R}_2, \dots, \mathbf{R}_M), \quad (2.2)$$

where  $\mathbf{r}_i$  and  $\mathbf{R}_i$  represent the coordinates of the system's electrons and nuclei respectively, and  $\tilde{E}$  represents the total energy of the system. Given a system with electrons of

mass  $m$  and nuclei of mass  $M_j$ , the Hamiltonian is

$$\hat{H} = -\frac{\hbar^2}{2m} \sum_{i=1}^N \nabla_i^2 + \frac{1}{8\pi\epsilon_0} \sum_{i \neq j} \frac{e^2}{|\mathbf{r}_i - \mathbf{r}_j|} - \frac{1}{4\pi\epsilon_0} \sum_{i,j} \frac{Z_j e^2}{|\mathbf{r}_i - \mathbf{R}_j|} - \frac{\hbar^2}{2} \sum_{j=1}^M \frac{\nabla_j^2}{M_j} + \frac{1}{8\pi\epsilon_0} \sum_{i \neq j} \frac{Z_i Z_j e^2}{|\mathbf{R}_i - \mathbf{R}_j|}, \quad (2.3)$$

where  $\epsilon_0$  is the permittivity of free space,  $Z_j$  is the atomic number of the nuclei, and  $e$  is the elementary charge. The equation may be written more compactly as

$$\hat{H} = \hat{T}_e(\mathbf{r}) + \hat{V}_{ee}(\mathbf{r}) + \hat{V}_{en}(\mathbf{r}; \mathbf{R}) + \hat{T}_n(\mathbf{R}) + \hat{V}_{nn}(\mathbf{R}) \quad (2.4)$$

The terms in Equation 2.4 are, respectively: kinetic energy of electrons, the electrostatic potential energy of electron-electron repulsion, potential energy of electron-nucleus attraction, kinetic energy of nuclei, potential energy of nucleus-nucleus repulsion.

Although the above equations apply for any and all physical systems regardless of size, complete analytical solutions are in practice unattainable for all but the smallest and simplest systems. Solving the Schrödinger equation for a real physical system would require one to take into account the motion of all the nuclei and electrons in the system. There are, however, important differences between the nuclei and electrons, brought about by the much larger mass of the nuclei. The movement of electrons is near-instantaneous compared to that of nuclei, therefore the contribution of the ionic momentum operator to the electronic wavefunction may be neglected. The Born-Oppenheimer (BO) approximation separates the motion of the electrons from that of the nuclei[1]. To describe how the energy of the electronic degrees of freedom varies with changes in nuclear coordinates, a series of calculations for the electrons is performed in various stationary configurations of the nuclei. With the nuclear terms in Equation 2.4 excluded, the electronic Hamiltonian reads, for a fixed nuclear configuration:

$$\hat{H}_e(\mathbf{r}; \mathbf{R}) = -\frac{\hbar^2}{2m} \sum_{i=1}^N \nabla_i^2 - \frac{e^2}{4\pi\epsilon_0} \left( \sum_{i,j} \frac{Z_j}{|\mathbf{r}_i - \mathbf{R}_j|} - \frac{1}{2} \sum_{i \neq j} \frac{1}{|\mathbf{r}_i - \mathbf{r}_j|} \right) \quad (2.5)$$

$$\hat{H}_e = \hat{T}_e(\mathbf{r}) + \hat{V}_{ee}(\mathbf{r}) + \hat{V}_{en}(\mathbf{r}; \mathbf{R}) \quad (2.6)$$

The electronic wavefunction  $\psi_e$  is computed as the stationary solution to the electronic Schrödinger equation:

$$\hat{H}_e(\mathbf{r}; \mathbf{R})\psi_e(\mathbf{r}; \mathbf{R}) = E_e(\mathbf{R})\psi_e(\mathbf{r}; \mathbf{R}); \quad (2.7)$$

where the electronic wavefunction obtained depends upon the nuclear positions  $\mathbf{R}$ . The energy of the system is recovered by including the nuclear repulsion term from Equation 2.3 which depends on nuclear coordinates  $\mathbf{R}$ .

Despite the separation of the nuclear and electronic degrees of freedom through the Born-Oppenheimer approximation, computing the electronic wavefunction remains challenging due to the large number of electrons and interactions between them. DFT reduces this complexity by considering not the many-electron wavefunction, but the electron density distribution  $n(\mathbf{r})$ . The foundational principle of DFT states that the electron density and electronic Hamiltonian have a functional relationship, which allows the

computation of all ground-state properties of a many-body system. This principle was put forward by Hohenberg and Kohn in two theorems[2]. The Hohenberg-Kohn theorems apply for a system of electrons under the influence of an external potential.

Theorem I: The external potential, and therefore the total energy, is a unique functional of the electron density.<sup>1</sup>

The first theorem states that there is a one-to-one correspondence of the ground-state electron density and the ground-state wave function. In other words, the ground-state energy  $E$  can be expressed as the functional  $E[n(\mathbf{r})]$ , where  $n(\mathbf{r})$  represents the electron density. This means that the Schrödinger equation can be solved by computing a function of 3 spatial variables rather than a function of  $3N$  variables, where  $N$  is the number of electrons.

Theorem II: The functional which delivers the ground-state energy of a system gives the lowest energy if, and only if, the input density is the true ground-state density.

The second theorem states an important property of the functional. If the true form of the functional were known, it could be found using the variational principle – changing the electron density until the energy given by the functional reaches a minimum. The actual form of the functional is, however, unknown. Therefore the variational principle is used in practice with numerous approximations of the functional.

Kohn and Sham proposed a practical implementation of DFT in which a real system of interacting electrons in an external potential is mapped onto a fictitious system of independent non-interacting electrons which generate the same density as the real system.

$$\left[ -\frac{\hbar^2}{2m}\nabla^2 + v_s(\mathbf{r}) \right] \psi(\mathbf{r}) = \epsilon_i \psi(\mathbf{r}) \quad (2.8)$$

$$v_s(\mathbf{r}) = V_{ext}(\mathbf{r}) + \frac{e^2}{4\pi\epsilon_0} \int \frac{n(\mathbf{r}')}{|\mathbf{r}-\mathbf{r}'|} d\mathbf{r}' + \frac{\delta E_{xc}[n(\mathbf{r})]}{\delta n(\mathbf{r})} \quad (2.9)$$

Equation 2.8 is an eigenvalue representation of the Kohn-Sham equation, where  $v_s(\mathbf{r})$  is the fictitious effective potential, and  $\epsilon_i$  is the orbital energy of the corresponding Kohn-Sham orbital  $\psi(\mathbf{r})$ . The electron density for the non-interacting system is given by

$$n(\mathbf{r}) = \sum_{i=1}^N |\psi(\mathbf{r})|^2. \quad (2.10)$$

With the Kohn-Sham equations, the problem is reduced to a series of coupled single-body problems. Every component of a Kohn-Sham DFT energy can be computed exactly, with the exception of the exchange-correlation,  $E_{xc}[n(\mathbf{r})]$ . The true form of the

<sup>1</sup>While a function takes a number (or a collection of numbers) as input and returns another number, a functional takes a *function* as input and returns a number.

exchange-correlation energy functional is unknown. DFT implementations therefore use approximations of the exchange-correlation functional. There are numerous approximations available, which range from the simple (e.g. local density approximation (LDA)) to the sophisticated (e.g. B3LYP hybrid functional). These approximations may be arranged in a hierarchy, referred to as Jacob's ladder[3], with the LDA at the lowest rung, and subsequent additions and modifications ascending the rungs of the ladder towards the ideal of chemical accuracy. Each rung will typically incorporate elements of the lower rungs, with additions which increase accuracy and, usually, computational effort. In practice, one chooses the best available functional on the basis of suitability to the task and system under investigation, within the constraints of computational cost.

A basic approximation of the exchange correlation is the local density approximation (LDA), in which the electrons are treated as a homogeneous electron gas of uniform density, giving

$$E_{xc}^{LDA}[n(\mathbf{r})] = \int n(\mathbf{r})\epsilon_{xc}n(\mathbf{r})d^3\mathbf{r}. \quad (2.11)$$

where  $\epsilon_{xc}$  is the exchange-correlation energy per electron of a homogeneous electron gas. The LDA functional is, however, inadequate for all but a small subset of systems, as it tends to under- and over-estimate the exchange and correlation energies respectively. The generalised gradient approximation (GGA) addresses the shortcomings of the uniform density approach. It expands upon the LDA in terms of the gradient ( $\nabla$ ) of the electron density; this takes into account the non-homogeneity of the real electron density. In its general form, it is

$$E_{xc}^{GGA}[n(\mathbf{r})] = \int f[n(\mathbf{r}), \nabla n(\mathbf{r})] d^3\mathbf{r} \quad (2.12)$$

The Perdew-Burke-Enzerhof(PBE)[4] functional, which is the GGA implementation used in this work, may be expressed as

$$E_{xc}^{GGA}[n(\mathbf{r})] = \int n(\mathbf{r})\epsilon_x(n(\mathbf{r}))F_{xc}(r_s, \zeta, s)d^3\mathbf{r} \quad (2.13)$$

where  $\epsilon_x$  is the local exchange of a uniform electron gas;  $F_{xc}$  is the so-called PBE enhancement factor;  $r_s$  is the local Seitz radius;  $\zeta$  is the relative spin polarisation

$$\zeta = \frac{(n_{\uparrow} - n_{\downarrow})}{n}; \quad (2.14)$$

and  $s$  is a scaled dimensionless density gradient

$$s = \frac{|\nabla n(\mathbf{r})|}{2(3\pi^2)^{1/3}n(\mathbf{r})^{4/3}}. \quad (2.15)$$

A complete discussion of the form of  $F_{xc}$  can be found in Ref [4]. GGA generally leads to improved total energies and energy barriers, the latter of which is key to the calculations performed in this work.

## 2.2. MOLECULAR DYNAMICS

Molecular dynamics (MD) is a method of studying the physical movements of atoms and molecules. In a molecular dynamics simulation, a collection of atoms is allowed to interact for a certain duration, to observe how the system evolves over time. The simulation consists of the numerical solution at preset intervals (timesteps) of the classical equations of motion

$$m_i \ddot{\mathbf{r}}_i = \mathbf{f}_i, \quad (2.16)$$

where  $m$  is the mass of the particle,  $\mathbf{r}$  is its position, and  $\mathbf{f}$  is the force acting on it. These forces are usually derived from the potential energy of the system as

$$\mathbf{f}_i = -\frac{\partial}{\partial \mathbf{r}_i} U \quad (2.17)$$

where  $U$  is the potential energy which depends on the complete set of coordinates of particles in the system. Using interatomic potentials, referred to also as force fields, the forces between the interacting atoms and molecules are calculated. By solving Newton's equations of motion at each time step, the trajectory of each particle is determined. From these trajectories, macroscopic properties of the simulated system can be extracted.

Molecular dynamics employs numerical techniques, as analytical solutions for the typically large number of particles in a simulation are not feasible. Restating the classical equations of motion as

$$\dot{\mathbf{r}}_i = \frac{\mathbf{p}_i}{m_i}, \quad \text{and} \quad \dot{\mathbf{p}}_i = \mathbf{f}_i \quad (2.18)$$

where  $\mathbf{p}$  represents the momenta of the particles, we get a system of coupled ordinary differential equations, for which many numerical integration algorithms exist. The choice of algorithm takes into account several factors. These equations are typically stiff, limiting the acceptable intervals between evaluations to small values. To sample a larger phase space, larger timesteps are desirable. Furthermore, the computation of the forces requires summing over numerous pairs of atoms, and is therefore expensive, so the number of force evaluations is best kept to a minimum. The duration of a simulation must also significantly exceed the correlation times of the properties of interest. The preference is for low order algorithms, i.e. those which do not require storage of higher derivatives of coordinates and velocities. For these reasons, the most common algorithm in use for MD simulations is the Verlet algorithm which is used in the simulations reported in this work. The Verlet scheme, specifically the velocity Verlet variant, may be written as follows:

$$\mathbf{p}_i(t + \frac{1}{2}\delta t) = \mathbf{p}_i(t) + \frac{1}{2}\delta t \mathbf{f}_i(t) \quad (2.19)$$

$$\mathbf{r}_i(t + \delta t) = \mathbf{r}_i(t) + \frac{1}{m_i} (\delta t \mathbf{p}_i(t + \frac{1}{2}\delta t)) \quad (2.20)$$

$$\mathbf{p}_i(t + \delta t) = \mathbf{p}_i(t + \frac{1}{2}\delta t) + \frac{1}{2}\delta t \mathbf{f}_i(t + \delta t) \quad (2.21)$$

The expensive force evaluation is carried out once after the step in Equation 2.20, after which the coordinates and momenta are advanced over the timestep  $\delta t$ , and the cycle repeats.

The force evaluation calls on the critical component of any MD simulation, the inter-atomic potential/force field. Since it determines the forces between particles, it determines the evolution of the system. A great deal of effort has been devoted to the development of different types of force fields, which are suited to the simulation of different systems and properties. They operate at different levels of accuracy and computational cost, and range from the classical treatment of inter-particle interactions to quantum mechanical methods, also including classical/quantum-mechanical hybrids. Examples include the Lennard-Jones potential, the embedded-atom method (EAM), and *ab initio* molecular dynamics. The simulations in this work employ the ReaxFF force field described in the following section.

### REAXFF: REACTIVE FORCE FIELD

Classical MD force fields typically use pre-defined bonding arrangements which remain unchanged throughout the course of the simulation; i.e. molecules remain molecules, and atoms remain discrete, as set at the start of a simulation. Therefore such force fields cannot model the formation and breaking of chemical bonds. For systems which require explicit modelling of bonding, a number of solutions exist, including those based on the bond order formalism. Bond order potentials can describe multiple bonding states for an atom, so can model chemical reactions with some accuracy. They are based on the principle that the strength of a bond is determined by the bonding environment. The number of bonds, their lengths, and also angles and torsions can all be included in the force field.

ReaxFF[5–7] is a general bond-order-dependent force field whose potential curves for dissociation and reaction derive from quantum mechanical methods. In ReaxFF, all atom pairs have non-bonded interactions; it treats van der Waals and Coulombic interactions explicitly, which is crucial for predicting the structures and properties of complex systems. Bonds, angle, torsions, etc are introduced to model complex molecules. This allows simulations at scales much larger than QM methods, trading some accuracy for much lower computational cost.

In ReaxFF, the energy of a system, from which the forces on each atom are derived, is composed of multiple partial energy contributions:

$$E_{system} = E_{bond} + E_{over} + E_{under} + E_{lp} + E_{val} + E_{pen} + E_{tors} + E_{vdW} + E_{Coulomb} + E_{spec} \quad (2.22)$$

$E_{bond}$  represents the energy of the bonds between atom pairs.  $E_{over}$  and  $E_{under}$  are the penalties for over- and under-coordination respectively (a large energy penalty would be applied for a H atom with more than one covalent bond).  $E_{lp}$ ,  $E_{val}$ , and  $E_{tors}$  are the contributions of the lone pair, valence angle, and torsion.  $E_{vdW}$  and  $E_{Coulomb}$  stand for the non-bonding van der Waals and Coulombic energies. For a number of special cases,

such as hydrogen bonds and electron lone pairs, system-specific energy contributions are included ( $E_{Spec}$ ). Figure 2.1 illustrates the energy calculation scheme.

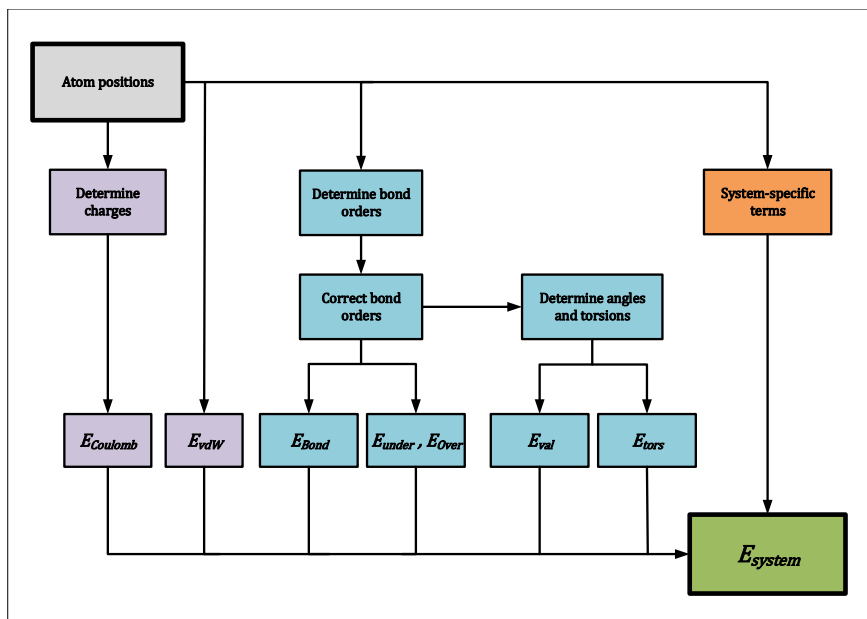


Figure 2.1: ReaxFF energy composition. Figure adapted from [8].

The potential energy contributions are grouped into bond-order-dependent and -independent. A central feature of ReaxFF is that bond order is calculated directly from the interatomic distance, per the formula:

$$\begin{aligned}
 BO_{ij} &= BO_{ij}^{\sigma} + BO_{ij}^{\pi} + BO_{ij}^{\pi\pi} \\
 &= \exp \left[ p_{bo1} \left( \frac{r_{ij}}{r_0^{\sigma}} \right)^{p_{bo2}} \right] + \exp \left[ p_{bo3} \left( \frac{r_{ij}}{r_0^{\pi}} \right)^{p_{bo4}} \right] + \exp \left[ p_{bo5} \left( \frac{r_{ij}}{r_0^{\pi\pi}} \right)^{p_{bo6}} \right]; \quad (2.23)
 \end{aligned}$$

where  $BO_{ij}$  is the bond order between atoms  $i$  and  $j$ ,  $r_{ij}$  is the interatomic distance,  $r_0^{\sigma}$ ,  $r_0^{\pi}$ ,  $r_0^{\pi\pi}$  are the equilibrium bond distances for sigma, pi, double-pi bonds respectively, and the  $p_{bo}$  terms are empirical parameters. The definition in Equation 2.23 is a continuous function which yields a differential potential energy surface, from which interatomic forces are computed. The bond-order is corrected to remove over- and under-coordination relative to each atom's preset valency; this eliminates spurious bond definitions for non-bonded neighbouring atoms. Bond energies and angle strains are calculated from the corrected bond order. The non-bonding van der Waals and Coulombic interactions are calculated for all pairs in the system. Van der Waals interactions are calculated using a shielded Morse potential, according to parameters set for each atom type. The Coulombic contribution is calculated from partial atomic charges determined via the electronegativity-equalisation method (EEM)[9].

The calculation of energies and forces in ReaxFF is governed by the set of force field parameters for each atom type (element) and for the interactions between atom pairs. In principle, these parameters can be selected and adjusted in accordance with empirical data, thus determining the optimal values. In practice, however, the parameters are obtained through optimisation relative to reference data from *ab initio* methods. Using global optimisation algorithms, a ReaxFF parameter set can be fit to adequately reproduce the energies, charges, and geometries of quantum mechanical calculations. The parametrisation process seeks to minimise an objective function of the form:

$$Error = \sum_{i=1}^n \left[ \frac{x_{i,ref} - x_{i,ReaxFF}}{\sigma_i} \right]^2 \quad (2.24)$$

where  $x_{i,ref}$  and  $x_{i,ReaxFF}$  are the reference value of the property and the value from ReaxFF respectively,  $\sigma_i$  is the weighting of the property, and the sum is over all the entries in the training set.

Although the earliest ReaxFF parameters were largely optimised through successive single-parameter optimisations, this method has become less widespread due to its pitfalls. This method involves picking one parameter  $p$  at a time, then making a parabolic fit of the objective function to the parameter  $p$  with perturbations  $\pm\delta p$ , and minimising the parabola. The procedure is repeated with other parameters until the error no longer decreases. This will involve several passes over all parameters until convergence, since they are inter-dependent. The likelihood of trapping in a local minimum is high. Moreover, the error surface is not necessarily parabolic, and the obtained parameter set may be a poor estimation.

Global optimisation algorithms have been developed which employ stochastic behaviour to better locate global minima on the multi-dimensional error surface. The most common are the covariance matrix adaptation evolution strategy (CMA-ES) algorithm and the Monte Carlo force field (MCFF) optimiser, the latter of which is used in this work. The MCFF optimiser uses a simple Metropolis Monte Carlo algorithm to sample the parameter space in a range determined by the user, following a procedure akin to the cooling of a system over time – simulated annealing. In this method, the optimisation is started at a high temperature, and a set of parameter values is randomly generated. The particles in the system, i.e. the parameters, move rapidly at random, and the *Error* is evaluated at each step. Parameter sets are accepted with a probability

$$P_a = \min[1, e^{(-\beta\Delta Error)}] \quad (2.25)$$

where  $\beta$  is the thermodynamic inverse temperature  $\frac{1}{k_B T}$ . With this acceptance condition, the parameter space is sampled more widely early on in the optimisation using small beta values, and gradually settles into a minimum as beta is increased. Due to the large number of parameters and minima, many different instances of the optimisation are executed in parallel, and the best-performing set is retained. The fit can be adjusted through the weighting  $\sigma_i$ , cooling rates, and target acceptance rates.

For an accurate description of the modelled materials, the training set generated with quantum-mechanical methods must cover a broad range of states, and configurations. For a solid such as ruthenium, the training set would include equations of state (EOS) curves for the typical metal crystal lattices, such as the native hexagonal close-packed (hcp) structure, the face-centred cubic (fcc), and the body-centred cubic (bcc). Other phases such as the diamond lattice and the simple cubic (sc) may also be included. Slab configurations to model the formation of surfaces are necessary as are amorphous structures, atom clusters, and defects. For interactions with other elements, bond length scans, valence angles, and charges are combined with the geometries and energies in the training set. Validation of the force field is achieved by applying it to a subset of the reference data which is excluded from the parametrisation, thus ensuring transferability to structures and states beyond the training set.

## MD SIMULATION ENSEMBLES<sup>2</sup>

The ergodic hypothesis states that over a sufficiently long duration, the time spent by a system in a certain region of phase space of microstates will be proportional to the size of that region. Stated differently, the average over a sufficiently long time of a quantity will be the same as the average over the statistical ensemble. An MD trajectory is a single sample of a process moving towards equilibrium from its starting configuration. If the trajectory is long enough, the simulation will have sampled the equilibrium distribution, one in which each configuration occurs with a frequency proportional to its Boltzmann factor. Such a system is referred to as ergodic. On the basis of this hypothesis, the time averaged quantities from a simulation of the system can be related to the ensemble-averaged quantities of an experiment.

An MD simulation in which the total energy  $E$  is a constant of motion, will sample an isolated system, a so-called microcanonical ensemble. With constant number  $N$  of particles, volume  $V$  of the system, and energy  $E$ , this is also known as an NVE ensemble. It is, however, more convenient to perform simulations in other ensembles, such as NVT (constant volume  $V$  and temperature  $T$ ) or NPT (constant pressure  $P$  and temperature  $T$ ), since real-world experiments are seldom conducted in constant energy conditions. An NVT-ensemble (canonical ensemble) is achieved by allowing the simulated system to exchange energy with a heat bath at a set temperature, such that the energy of the system may vary, while keeping the temperature constant. An NPT ensemble (isobaric-isothermal ensemble) has, in addition to the heat bath, a pressure bath, via which a constant pressure is maintained while allowing the system volume to change. A brief description of the operation of heat and pressure baths follows.

Temperature regulation in MD simulations is performed using algorithms known as thermostats. Given a system with  $N$  particles of mass  $m_i$  and velocity  $v_i$ , the temperature

---

<sup>2</sup>This section is largely adapted from Refs [10, 11]

of the system is given by

$$T = \frac{2}{3Nk_B} \left\langle \sum_{i=1}^N \frac{m_i v_i^2}{2} \right\rangle, \quad (2.26)$$

where the angled brackets indicate a time-averaged quantity. An average over a snapshot of an MD simulation would give the instantaneous temperature per the equipartition theorem. This instantaneous temperature will not necessarily be equal to the time-averaged temperature; in the canonical ensemble, it will fluctuate around the target temperature. Thermostats operate by making adjustments to the Newtonian equations of motion, such that the velocities yield the desired average temperature. Thermostats differ in the way these adjustments are implemented. They may be deterministic or stochastic, affect the whole system (global) or a subset (local). A widely-used option is the Nosé-Hoover thermostat. It introduces an additional, fictitious degree of freedom with a given mass, which may be changed to interact with the system in a predictable and reproducible fashion while maintaining the canonical ensemble. In order to enhance ergodicity, particularly with small systems, Nosé-Hoover thermostats can be linked in a chain giving the most common implementation of this thermostat: the Nosé-Hoover chain (NHC)[12].

Barostats control the pressure, and are commonly used in conjunction with a thermostat which maintains the target temperature. The barostat operates in a manner similar to the thermostat. In a basic implementation, a simple volume rescaling algorithm will scale the volume of the system each time the barostat is executed, in such a way that the resulting instantaneous pressure is exactly equal to the target pressure. Since this does not sample the proper ensemble, and does not approach the target pressure smoothly, it is not suitable for production sampling. The Berendsen barostat[13] ameliorates the shortcomings of simple volume rescaling by coupling the system to a weakly-interacting pressure bath. The bath executes periodic scaling of the volume by a scaling factor, producing more realistic fluctuations in pressure while approaching the target value. While the Berendsen sampling is not well-defined or suitable for production sampling, it is adequate for initial preparatory equilibration.

The molecular dynamics simulations in this work employ both NPT and NVT ensembles. The initial stage of the simulation, during which the system is brought to equilibrium, is done under the NPT ensemble with a Berendsen barostat and NHC thermostat. Thereafter, during the data production and collection stage for the properties of interest, the NVT ensemble with the NHC thermostat is used.

**REFERENCES**

- [1] M. Born and R. Oppenheimer, *Zur Quantentheorie der Molekeln*, *Annalen der Physik* **389**, 457 (1927).
- [2] P. Hohenberg and W. Kohn, *Inhomogeneous Electron Gas*, *Physical Review* **136**, B864 (1964).
- [3] J. P. Perdew, *Jacob's ladder of density functional approximations for the exchange-correlation energy*, **1**, 1 (2003).
- [4] J. D. Perdew, K. Burke, and M. Ernzerhof, *Generalized Gradient Approximation Made Simple*, *Physical Review Letters* **77**, 3865 (1996).
- [5] A. C. T. van Duin, S. Dasgupta, F. Lorant, and W. A. Goddard, *ReaxFF: A Reactive Force Field for Hydrocarbons*, *The Journal of Physical Chemistry A* **105**, 9396 (2001).
- [6] K. Chenoweth, A. C. Van Duin, P. Persson, M. J. Cheng, J. Oxgaard, and W. A. Goddard, *Development and application of a ReaxFF reactive force field for oxidative dehydrogenation on vanadium oxide catalysts*, *Journal of Physical Chemistry C* **112**, 14645 (2008).
- [7] M. F. Russo and A. C. Van Duin, *Atomistic-scale simulations of chemical reactions: Bridging from quantum chemistry to engineering*, *Nuclear Instruments and Methods in Physics Research, Section B: Beam Interactions with Materials and Atoms* **269**, 1549 (2011).
- [8] T. P. Senftle, S. Hong, M. Islam, S. B. Kylasa, Y. Zheng, Y. K. Shin, C. Junkermeier, R. Engel-herbert, M. J. Janik, H. M. Aktulga, T. Verstraelen, A. Grama, and A. C. T. V. Duin, *The ReaxFF reactive force- field : development , applications and future directions*, *Nature Publishing Group* (2016), 10.1038/npjcompumats.2015.11.
- [9] W. J. Mortier, S. K. Ghosh, and S. Shankar, *Electronegativity Equalization Method for the Calculation of Atomic Charges in Molecules*, *Journal of the American Chemical Society* **108**, 4315 (1986).
- [10] D. Frenkel and B. Smit, *Molecular Dynamics in Various Ensembles*, *Understanding Molecular Simulation* , 139 (2002).
- [11] E. Braun, J. Gilmer, H. B. Mayes, D. L. Mobley, J. I. Monroe, S. Prasad, and D. M. Zuckerman, *Best Practices for Foundations in Molecular Simulations [Article v1.0]*, *Living Journal of Computational Molecular Science* **1**, 1 (2019).
- [12] G. J. Martyna, M. L. Klein, and M. Tuckerman, *Nosé-Hoover chains: The canonical ensemble via continuous dynamics*, *The Journal of Chemical Physics* **97**, 2635 (1992).

- [13] H. J. Berendsen, J. P. Postma, W. F. Van Gunsteren, A. Dinola, and J. R. Haak, *Molecular dynamics with coupling to an external bath*, The Journal of Chemical Physics **81**, 3684 (1984).

# 3

## TIN, THE ENABLER – HYDROGEN DIFFUSION INTO RUTHENIUM

*Hydrogen interaction with ruthenium is of particular importance for the ruthenium-capped multilayer reflectors used in extreme ultraviolet (EUV) lithography. Hydrogen causes blistering, which leads to a loss of reflectivity. This problem is aggravated by tin. This study aims to uncover the mechanism via which tin affects the hydrogen uptake, with a view to mitigation. We report here the results of a study of hydrogen interaction with the ruthenium surface in the presence of tin using Density Functional Theory and charge density analyses. Our calculations show a significant drop in the energy barrier to hydrogen penetration when a tin atom or a tin hydride molecule ( $\text{SnH}_x$ ) is adsorbed on the ruthenium surface; the barrier has been found to drop in all tested cases with tin, from 1.06 eV to as low as 0.28 eV in the case of stannane ( $\text{SnH}_4$ ). Analyses show that, due to charge transfer from the less electronegative tin to hydrogen and ruthenium, charge accumulates around the diffusing hydrogen atom and near the ruthenium surface atoms. The reduced atomic volume of hydrogen, together with the effect of electron–electron repulsion from the ruthenium surface charge, facilitates subsurface penetration. Understanding the nature of tin’s influence on hydrogen penetration will guide efforts to mitigate blistering damage of EUV optics. It also holds great interest for applications where hydrogen penetration is desirable, such as hydrogen storage.<sup>1</sup>*

---

<sup>1</sup>This chapter has been published as: Onwudinanti, C., Tranca, I., Morgan, T., & Tao, S. (2019). Tin, the enabler – hydrogen diffusion into ruthenium. *Nanomaterials*, 9(1), 129. <https://doi.org/10.3390/nano9010129>

### 3.1. INTRODUCTION

Hydrogen interacts with metal surfaces in many varied and important technological applications. This occurs in catalysis [1, 2], as well as hydrogen separation [3, 4], storage [5], and sensors [6]. The ability of the small atom to permeate metals and change their properties gives hydrogen–metal systems added significance; for instance, embrittlement of metals remains an obstacle to the transport and storage of hydrogen [7, 8]. In this case, as in separation and purification, diffusion into the subsurface and bulk of the metal is quite important [9]. This interaction has been studied extensively, particularly with transition metals, and the field maintains a high level of scientific interest and relevance [10–13]. The addition of a second metal creates a so-called bimetallic surface. This often introduces significant changes to the electronic structure and characteristics of that surface relative to the single metal [14–17], with consequences for its technological applications.

The use of ruthenium on reflective optics is one such application, with a bimetallic system interacting with hydrogen. The multi-layer reflectors used in the optical systems of extreme ultraviolet (EUV) lithography employ a ruthenium capping layer [18, 19]; this surface may be contaminated by tin debris from the laser-pulsed tin plasma, the source of the EUV photons. Hydrogen used for cleaning the optics comes into contact with the surface and debris. It may penetrate the surface and diffuse to the interfaces of the multi-layer structure, where it recombines to form pockets of gas. When these pockets reach a critical pressure, the layers separate, which results in blistering of the mirror and loss of reflectivity [20, 21]. This process appears to be facilitated by tin [22].

Ruthenium has been the subject of many studies [23], as it is used in diverse chemical processes. The Ru-Sn bimetallic catalyst has been studied as a promising option for selective hydrogenation of the carbonyl group [24, 25], which is important in the production of unsaturated alcohols [26]. It is also a candidate for hydrogen production via glycerol steam reforming [27]. Hydrogen does not readily permeate ruthenium [28], but the existence of subsurface hydrogen has been demonstrated in ruthenium [29, 30] and other metals [31], and it may be considered a precursor to dissolved or hydridic hydrogen in the bulk.

On the one hand, the undesirable effects of hydrogen penetration, i.e., blistering of the reflector, make it necessary to study the penetration process and possible solutions. On the other, the facilitation of diffusion into the ruthenium crystal opens the door to potential applications such as separation and purification. The latter is made especially attractive by the significantly lower cost of ruthenium and tin relative to palladium.

In this study, we focus on the tin-mediated hydrogen penetration of the Ru(0001) surface. Using Density Functional Theory (DFT), we demonstrate that tin affects the energy barriers to diffusion in a manner that facilitates penetration into the ruthenium. We show that adsorbed tin atoms and tin hydrides cause hydrogen to bond to the surface with a more compactly distributed charge, and also cause charge accumulation on the metal surface. The result is a lower energy barrier to subsurface diffusion.

The article is organised as follows: in the next section, we present details of the computational methodology employed. Thereafter, we report the results of calculations for hydrogen on the Ru(0001) surface, and in the ruthenium subsurface and bulk. A number of relevant ruthenium-tin-hydrogen interactions are then considered, and we discuss the changes observed upon introducing tin. Finally, we present a comprehensive analysis of the electronic charge density distributions in the examined interactions, and discuss the implications of the results.

## 3.2. COMPUTATIONAL METHODS

### 3.2.1. DFT CALCULATIONS

The results presented in this work are based on computations performed within the framework of DFT, as implemented in the Vienna Ab Initio Simulation Package (VASP) [32–34]. The calculations were performed with the generalized gradient approach as proposed by Perdew, Burke, and Ernzerhof (PBE) [35], with the following key convergence parameters: a kinetic energy cutoff of 400 eV, residual force criterion of  $1 \times 10^{-2}$  eV/Å, and a  $1 \times 10^{-5}$  eV energy convergence criterion. Slab calculations were performed with a  $(9 \times 9 \times 1)$   $\Gamma$ -centred  $k$ -points grid, while bulk calculations were done with a  $(9 \times 9 \times 9)$  grid; all atoms were allowed to relax in the optimization process. In order to account for long-range dispersive interactions, all calculations were performed with the DFT-D3 dispersion correction proposed by Grimme et al. [36]. Transition state calculations were carried out using the Climbing Image Nudged Elastic Band (CINEB) algorithm [37], with a force criterion of  $1 \times 10^{-2}$  eV/Å and three (3) intermediate geometries for the transition state search.

The calculated lattice parameters for hexagonal close-packed (hcp) ruthenium are  $a = 2.69$  Å and  $c/a = 1.58$ , which are in good agreement with experimental results, 2.71 Å and 1.58, respectively [38]. The surface is modelled by a slab of seven layers using a  $(2 \times 2)$  cell, with  $\sim 15$  Å of vacuum between the periodic images in the  $z$ -direction. The number of layers and the vacuum height were found to give accurate results at reasonable computational cost — the calculated surface energy for the  $(2 \times 2)$  cell changes by less than 2% from 5 layers to 11 layers.

Lattice parameters  $a = 5.82$  Å and  $b = 3.17$  Å for solid tin in the  $\beta$ -Sn crystal structure were found to be in good agreement with measured values, 5.83 Å and 3.18 Å, respectively [38]. Slab calculations for Sn(001) and Sn(010) surfaces were performed with  $(1 \times 1 \times 3)$  and  $(1 \times 3 \times 1)$  cells of 7-layer slabs, with  $\sim 15$  Å vacuum.

For hydrogen, the energy of adsorption is computed per the definition

$$E_{ads} = \frac{1}{n} \left( E_{nH,surf} - E_{surf} - \frac{n}{2} E_{H_2} \right), \quad (3.1)$$

where  $E_{nH,surf}$ ,  $E_{surf}$ , and  $E_{H_2}$  stand respectively for the total energies of the ruthenium slab with  $n$  adsorbed hydrogen atoms, clean ruthenium slab, and the energy of the hydrogen molecule. The formation energy of interstitial hydrogen, normalised to the

hydrogen concentration, is calculated according to the definition

$$\Delta E_{H_2} = \left( E_{M_x H_y} - x E_M - \frac{y}{2} E_{H_2} \right) / \frac{y}{2}, \quad (3.2)$$

where  $x, y$  are respectively the number of metal atoms and the number of hydrogen atoms, while  $E_{M_x H_y}$ ,  $E_M$ , and  $E_{H_2}$  stand respectively for the total energy of the metal hydride, the energy of each bulk metal atom, and the energy of a hydrogen molecule.

Jump frequencies for the hydrogen diffusion were extracted from the transition state calculations. The jump rate for a diffusing hydrogen atom may be expressed as

$$\nu = \nu_0 e^{-E_b / k_B T}, \quad (3.3)$$

where  $E_b$  is the energy difference between the transition state and ground state. For bulk diffusion, the pre-exponential factor  $\nu_0$  in Equation (3.3) may be approximated by the expression [39]

$$\nu_0 = \frac{\prod_{i=1}^N \omega_i}{\prod_{i=1}^{N-1} \omega_i^*}, \quad (3.4)$$

where  $\omega_i$  and  $\omega_i^*$  are the vibrational frequencies in the initial and transition states respectively, obtained by determining the the Hessian matrix (matrix of the second derivatives of the energy with respect to atomic positions).

Due to the low mass of the hydrogen atom, its adsorption and diffusion behaviour is, in general, influenced by zero-point energy (ZPE). The ZPE is calculated by the relation

$$ZPE = \frac{\sum_i \hbar \nu_i}{2}, \quad (3.5)$$

where  $\nu_i$  is a real normal mode frequency. The zero point energy for a hydrogen molecule ( $H_2$ ) calculated thus is 0.27 eV (0.135 eV per H atom), corresponding to a vibrational mode of  $4354 \text{ cm}^{-1}$ , in good agreement with the experimentally-determined value of  $4401 \text{ cm}^{-1}$  [40]. However, ZPE contributions are not explicitly included in this work, as they do not affect the computed energies and barriers to a significant degree, particularly in relation to one another.

### 3.2.2. ELECTRONIC STRUCTURE AND BONDING ANALYSIS

In addition to the energy calculations, we have carried out an in-depth analysis of the chemical bonding for a thorough understanding of the interaction between species. The bonds of main interest are those between the diffusing hydrogen atom and the surface ruthenium atoms. We investigated the Bader atomic charges and volumes [41–44], the Density Derived Electrostatic and Chemical (DDEC6) bond orders and net atomic charges [45, 46], the electron density and Laplacian at bond critical points (BCP) [47], and also the Crystal Orbital Hamilton Population (COHP) and Crystal Orbital Overlap Population (COOP) functions [48–51].

The Bader charge is a measure of the electron occupation on an atom, and indicates charge transfer, while the Bader volume is an indication of how closely the charge associated with each atom is localised around the nucleus. The bond-critical points (BCPs) were assigned to saddle-points of electron density along the bond-paths. The electron density value at the BCP shows the covalent energy contribution to the chemical bond. The covalent nature of the bond is reflected in the bond order, with a higher value showing a stronger covalent bond. The sum of bond orders for each atom, its total bond order, is an indication of the activity of the atom in that particular configuration. The ionic contribution of a bond can be characterized by net atomic charge, which quantifies the charge transfer between atoms. The Laplacian, the scalar derivative of the gradient vector field of the electron density, indicates where the electronic charge is locally concentrated or depleted. The sign and value of the Laplacian at the BCP provide information on the nature of a bond, with a negative sign indicating a shared interaction (e.g., covalent bonding), while a positive sign indicates a non-covalent interaction such as ionic, hydrogen, or van der Waals [52, 53].

The COOP and COHP enable the extraction of information about bonding in the system on the basis of Partial Density of States (PDOS) and Bond Order Overlap Population density. They allow us to identify bonding, non-bonding, and anti-bonding interaction domains for pairs of atoms (or orbitals). The COOP is defined according to the formula:

$$\text{COOP}_{ij}(E) = S_{ij} \sum_n c_i^n c_j^{*n} \delta(E - E_n), \quad (3.6)$$

where  $S_{ij} = \langle \varphi_i | \varphi_j \rangle$  is the overlap of atomic orbitals  $\varphi_i$  and  $\varphi_j$ , and  $c_i$  and  $c_j$  are respectively the coefficients of these atomic orbitals in the molecular orbital  $\psi_n$ . Positive and negative COOP values indicate bonding and anti-bonding interactions, respectively, while a zero value represents a non-bonding interaction. The closely-related COHP is defined thus:

$$-\text{COHP}_{ij}(E) = H_{ij} \sum_n c_i^n c_j^{*n} \delta(E - E_n), \quad (3.7)$$

where  $H_{ij}$  represents the Hamiltonian matrix element between atomic orbitals  $\varphi_i$  and  $\varphi_j$ . In replacing the  $S_{ij}$  matrix with the  $H_{ij}$ , the COHP values are reversed: negative for bonding and positive for anti-bonding, with zero values again representing a non-bonding interaction. More thorough discussions of the COOP and COHP techniques can be found in the cited literature [48–51].

Combining these analytical tools allows us to carry out a comprehensive examination of the relevant bonds in each modelled system and reveal the underlining reaction mechanisms. Recently, computational studies using a combination of these electronic structure analysis techniques have led to an improved understanding of the reactivity and scaling laws on transition metal surfaces [13].

### 3.3. RESULTS

In this section, we present the results of DFT calculations of hydrogen adsorption and diffusion. In the first two subsections, we report the results for hydrogen interaction with ruthenium and tin, respectively. For the former, we show the stable configurations and their energies of formation, and also present the results of CINEB transition state calculations for hydrogen diffusion and the corresponding energy barriers. In Section 3.3.3, to show the influence of the tin on the H–Ru interaction, we present the range of calculations performed for hydrogen–ruthenium–tin interactions on the Ru(0001) surface. The calculations cover adsorption, surface diffusion, and subsurface penetration of hydrogen.

#### 3.3.1. HYDROGEN AND RUTHENIUM

##### SURFACE, SUBSURFACE, AND BULK

We calculated adsorption energies of hydrogen atoms on the ruthenium surface to identify the relative stability of different adsorption sites. The Ru(0001) surface is chosen as it has the lowest surface energy  $\gamma$  and is therefore the most commonly-exposed; it is well-studied and represented in the literature. We calculated the energy of adsorption of hydrogen at  $\frac{1}{4}$  monolayer (ML), i.e., one hydrogen atom for four surface ruthenium atoms in our  $(2 \times 2)$  cell. Four sites are considered for adsorbed hydrogen atoms on the pure Ru(0001) surface, as shown in Figure 3.1: *top*, *bridge*, *hcp*, and *fcc* sites. We have also identified the subsurface and bulk interstitial sites for hydrogen in ruthenium. The results of the calculations are summarised in Table 3.1.

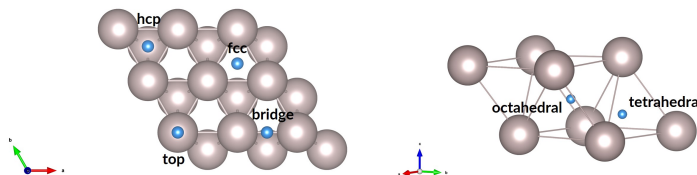


Figure 3.1: Surface adsorption and bulk interstitial sites for hydrogen on Ru(0001) and in Ru bulk. Blue spheres represent hydrogen atoms.

For Ru(0001), the *fcc* site was found to be most favourable with  $E_{ads} = -0.64$  eV, a slight energy advantage of 0.06 eV relative to the *hcp* site. The top site is the least favourable at  $-0.15$  eV. Nonetheless, the overall result for the four adsorption modes indicates that adsorption readily occurs on the ruthenium surface, as all sites have negative values for  $E_{ads}$ . The trend in energies and the preference for the *fcc* site is in agreement with the results reported in the literature [54, 55]; the differences can be attributed to the different software, functionals, parameters, and convergence criteria used in the computations.

Table 3.1: Energies and structure parameters for adsorbed and interstitial hydrogen on Ru(0001) and in ruthenium bulk. Adsorption energies correspond to  $\frac{1}{4}$  ML hydrogen coverage, while hydride formation energies are for hydrogen concentration (H/Ru) equal to  $\frac{1}{6}$ . Sites marked “\*” correspond to calculations done with one (1) Sn adatom in an *hcp* site; *fcc\_Sn* is the *fcc* site closest to the Sn adatom in an *hcp* site.

	$E_{ads}$ [eV]			$\Delta E_{H_2}$ [eV]	
	This work	Other		This work	Other
top	-0.15	-0.14 [55], -0.09 [54]	T <sub>bulk</sub>	0.76	
bridge	-0.45	-0.44 [55], -0.43 [54]	O <sub>bulk</sub>	0.21	
hcp	-0.58	-0.50 [55], -0.52 [54]	T <sub>sub</sub>	0.90	1.04 [55]
fcc	-0.64	-0.59 [55], -0.55 [54]	O <sub>sub</sub>	0.15	0.37 [55]
top *	0.01				
hcp *	-0.52				
fcc *	-0.58				
fcc_Sn *	-0.33				

An interstitial hydrogen atom in ruthenium bulk can occupy one of the two sites shown in Figure 3.1, octahedral or tetrahedral, within the voids found in the *hcp* crystal structure. The results presented in Table 3.1 show that the interstitial sites have positive energies of formation with relative to H<sub>2</sub>; therefore, interstitial hydride formation is unfavourable in ruthenium at this concentration (eight ruthenium atoms per hydrogen atom). This aligns with experimental data, which show very low hydrogen solubility in ruthenium due to the highly endothermic nature of the reaction [28].

Overall, hydrogen readily adsorbs on the Ru(0001) surface, as shown by the calculated adsorption energies. According to Luppi et al., the H<sub>2</sub> molecule does not face a large barrier to dissociation on the ruthenium surface: from 0.013 eV to 0.436 eV, depending on the initial configuration and exchange-correlation functional used in the computations [56]. Therefore, dissociative adsorption of molecular hydrogen on ruthenium occurs easily. However, our results show that interstitial hydrogen in the ruthenium bulk is not thermodynamically favoured.

### DIFFUSION

In order to acquire a more complete picture of the hydrogen–ruthenium interaction on the surface and in the bulk of the metal, we performed transition state calculations using the CINEB method. For a number of diffusion scenarios, we calculated transition states and energy barriers to hydrogen diffusion, covering (i) surface diffusion, (ii) bulk diffusion, and (iii) subsurface penetration.

For surface diffusion, we have found the transition state for diffusion of an adsorbed hydrogen atom from an *fcc* site to a neighbouring *hcp* site, and vice versa. Both transition states are found to be more or less the bridge adsorption mode, in which the hydrogen

atom is equidistant from two neighbouring surface Ru atoms, above the axis joining the atoms. We found the energy barrier to be 0.18 eV for the *fcc* to *hcp* jump; the barrier for the reverse transition (*hcp* to *fcc*) is even lower, at 0.12 eV, due to the 0.06 eV difference in adsorption energies of the *hcp* and *fcc* sites. These values indicate a largely favourable energy landscape for diffusion of adsorbed hydrogen across the Ru(0001) surface, and this conclusion agrees with the findings reported elsewhere [57, 58].

## 3

The picture for bulk diffusion is somewhat more complicated. As Figure 4.4 illustrates, the two stable interstitial sites (octahedral and tetrahedral sites) imply four diffusion paths: (i) tetrahedral to octahedral (TO), (ii) tetrahedral to tetrahedral (TT), (iii) octahedral to octahedral (OO), and (iv) octahedral to tetrahedral (OT). The transition state for each path has the diffusing atom passing through a triangle formed by three ruthenium atoms. The energy barriers for all four paths are listed in Figure 4.4, as are the jump frequencies derived from the vibrational analyses of the interstitial hydrogen states and the transition states. The energy barriers for the jumps (0.21–0.75 eV) and the jump frequencies suggest that hydrogen diffusion in the ruthenium bulk is quite rapid. For the most important diffusion event, subsurface penetration, we have looked at one key diffusion path: from the *fcc* site on the surface to the octahedral interstitial site in the subsurface. As these sites represent the most favourable locations for hydrogen on the surface and in the subsurface void, we believe that this is the most likely path for hydrogen penetration into the metal. The energy barrier is found to be 1.06 eV, which indicates that this diffusion step is unfavourable from a thermodynamic standpoint, although it remains accessible. Most importantly, this is the largest energy barrier faced by a hydrogen atom in going from the molecule in vacuum to the metal surface, across the surface, and into the metal bulk.

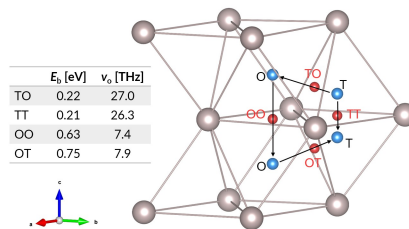


Figure 3.2: Interstitial hydrogen diffusion paths and transition states. Blue spheres represent interstitial sites, while red spheres indicate transition states. O and T correspond to octahedral and tetrahedral sites; OO, OT, TO, and TT show the corresponding diffusion path ways between these sites. The accompanying table shows energy barriers and jump frequencies (per Equation (3.4)) for the interstitial diffusion paths, for hydrogen concentration (H/Ru) equal to  $\frac{1}{16}$ .

### 3.3.2. HYDROGEN AND TIN

We evaluated hydrogen adsorption on tin surfaces by calculating adsorption energies for a number of sites on the Sn(100) and Sn(010) surfaces. The tin slab for both surfaces is a  $1 \times 1$  cell of a  $\beta$ -Sn structure with seven layers. At  $\frac{1}{4}$  ML and  $\frac{1}{2}$  ML hydrogen coverage for the Sn(100) and Sn(010) surfaces respectively, all adsorption sites without exception have positive energies relative to  $H_2$ , i.e., dissociation on these tin surfaces is entirely unfavourable. This points to the conclusion that tin deposited on the ruthenium surface does not provide a site of increased dissociation/adsorption of hydrogen molecules.

Tin, however, forms volatile hydrides. Stannane ( $SnH_4$ ) and possibly other hydride compounds are formed when tin is etched from a ruthenium surface by hydrogen. Stannane readily evaporates, adsorbs, and dissociates on the ruthenium surface, which results in the persistence of tin on the ruthenium surface [22, 59, 60].

### 3.3.3. THE EFFECT OF TIN

We continue our investigation of the hydrogen-tin-ruthenium interaction on the Ru(0001) surface by calculating the adsorption energies for  $\frac{1}{4}$  ML of tin on the Ru(0001) surface, finding that the *hcp* site is thermodynamically most favoured at this coverage, with  $E_{ads} = -1.49$  eV. The adsorption energy for the *fcc* site differs by 0.09 eV from that of the *hcp* site, while the *top* site is 0.55 eV higher in energy. We found the energy barrier for tin migration from the *hcp* to the *fcc* site to be 0.13 eV. The barrier for the reverse jump is 0.04 eV; the difference is entirely due to the relative adsorption energies of the sites. Therefore, neither tin nor hydrogen faces a large energy barrier to diffusion on the Ru(0001) surface.

We consider the adsorption and diffusion of hydrogen on the Ru(0001) surface with tin present. A tin atom is located at its preferred *hcp* site on a  $2 \times 2$  Ru(0001) slab, and the adsorption energies are calculated for the subsequent adsorption of hydrogen to the surface. In addition to the earlier-described *top*, *hcp*, and *fcc* sites, a second type of *fcc* site (*fcc\_Sn*) is found, which has the hydrogen atom in the *fcc* site closest to the Sn atom. The calculated adsorption energies are given in Table 3.1. As with the clean ruthenium surface, the *fcc* site is lowest in energy ( $E_{ads} = -0.58$  eV); the *top* site is least favoured, with its slightly positive adsorption energy of 0.01 eV. Overall, the hydrogen atom tends to occupy sites which are not in close proximity to the tin atom. These surface adsorption results are similar to findings for PtSn surface alloys [61], on which hydrogen adsorption sites near tin are higher in energy. The *fcc\_Sn* site ( $-0.33$  eV) is higher in energy than the *hcp* and *fcc* sites, and the barrier faced by hydrogen in jumping to this site is higher than the barrier when jumping to a site not next to the tin atom. This preference for ruthenium has important consequences for hydrogen diffusion across the Ru(0001) surface in the presence of tin, as the hydrogen jump trajectory becomes more convoluted (see Figure 3.3) due to the change in the energy landscape and blockage of sites by tin atoms. It follows that the surface mobility of hydrogen is reduced by this obstacle, with consequences for hydrogen diffusion into the subsurface.

The presence of tin also results in a substantial change in the energy barrier to sub-

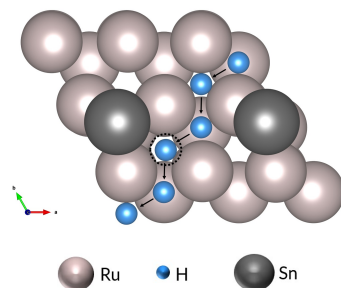


Figure 3.3: Example jump trajectory of H atom on Ru(0001) with  $\frac{1}{4}$  ML Sn. The highlighted site (dashed circle) is the *fcc* site next to an Sn atom (*fcc\_Sn*).

surface penetration. Figure 3.4 shows a comparison of the energy barriers for the migration of a hydrogen atom from the *fcc* site on the surface to a subsurface octahedral site in the presence and absence of tin. These cases correspond to adsorption and dissociation of progressively more hydrogenated tin hydrides ( $\text{SnH}$ ,  $\text{SnH}_2$ ,  $\text{SnH}_3$ ,  $\text{SnH}_4$ ) or co-adsorption of tin and varying quantities of hydrogen. The energy barrier drops to 0.28 eV when the stannane molecule is the source of the diffusing atom.

It is important to note that the studied scenarios are not a simple progression from low hydrogen levels to high. The cases for  $\text{SnH}$  and  $\text{SnH}_2$  are very similar, differing only in the presence of a second hydrogen atom at a considerable distance from the tin atom. Their transition states are similar, with the diffusing hydrogen atom located in the centre of a triangle formed by three Ru surface atoms. The relative position of the tin atom is unchanged. However, the  $\text{SnH}_3$  case is different from the previous two in that its transition state and final state have the tin atom at the *fcc* site, above the penetrating hydrogen atom. In this, it is similar to the transition state of the case with the stannane molecule. Despite the clear differences in geometry and energies for all the scenarios, the initial and final positions of the diffusing hydrogen atom are the same in all cases: *fcc* site and octahedral site, respectively (see Figure 3.4). In all cases, the penetrating atom is found in the midst of three surface atoms in the transition state.

One other modelled case, which differs from all of those described in the preceding paragraph, is the case for a vertically-oriented  $\text{SnH}_2$  molecule ( $\text{SnH}_2^*$ ), with a hydrogen atom above the *fcc* site. As shown in Figure 3.5, the molecule does not adsorb on the Ru(0001) surface; rather, at the end of the relaxation calculation, the hydrogen atom which is initially closer to the metal surface is located in the octahedral subsurface site. The tin atom ends up at the *fcc* site, with the second hydrogen atom adsorbed on top of the tin atom. Therefore, what our calculations show is a more or less barrier-less penetration through the surface when the molecule approaches the surface in this configuration.

As mentioned earlier, the energy barrier to subsurface penetration for hydrogen on

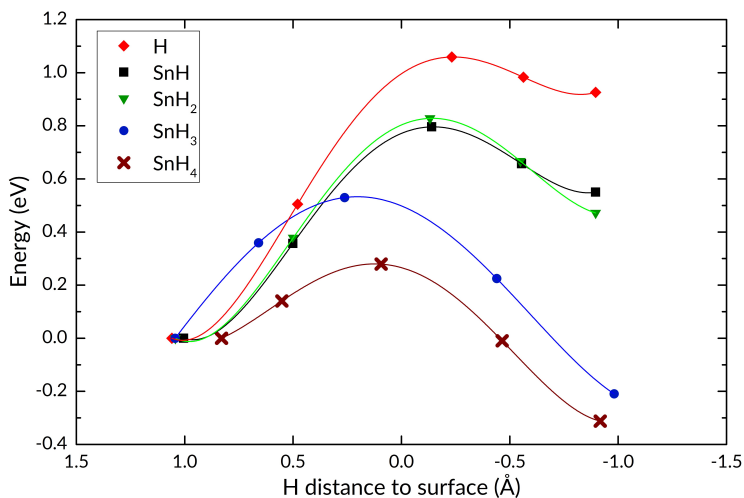
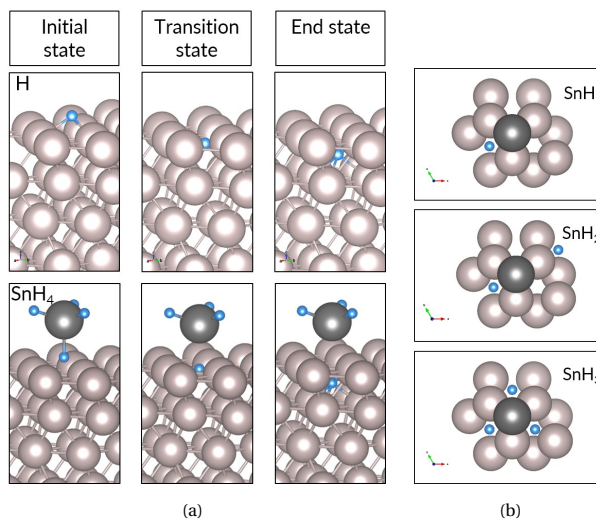


Figure 3.4: (a) initial, transition, and end states of hydrogen subsurface diffusion for a hydrogen atom (top row) and for SnH<sub>4</sub> (bottom row) on Ru(0001); (b) top view of adsorbed SnH, SnH<sub>2</sub>, and SnH<sub>3</sub> configurations; (c) energy profiles for diffusion of a hydrogen atom from an *fcc* site to a subsurface octahedral site. Negative distance values indicate that the H atom is beneath the ruthenium surface.

an otherwise clean Ru(0001) surface equals 1.06 eV. When tin is present, the energy barrier is lower in all the different test cases: 0.80 eV for SnH, 0.83 eV for SnH<sub>2</sub>, 0.53 eV for SnH<sub>3</sub>, and 0.28 eV when the hydrogen atom is taken from the adsorbed SnH<sub>4</sub>

molecule, which is a considerable drop from the value for hydrogen on Ru(0001) with no tin present. For subsurface penetration at sites far from the tin atom, the energy barrier is essentially unchanged. In other words, the diffusion of a hydrogen atom from the *fcc* site on the Ru(0001) surface to the underlying octahedral void in the subsurface is made significantly easier by the proximity of a tin atom.

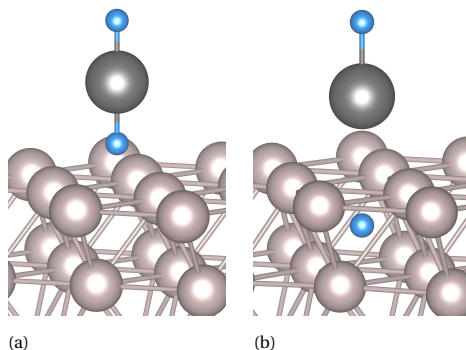


Figure 3.5: (a) Initial and (b) end states for  $\text{SnH}_2^*$  (vertically-oriented  $\text{SnH}_2$  molecule) on Ru.

### 3.3.4. CHARGE DENSITY ANALYSIS

A deeper look into the effect of tin on the subsurface penetration is obtained by analysing the electronic charge density, based on the output of the DFT calculations. In the various penetration scenarios, the bonds which are formed and broken affect the energy barrier to H penetration, and so do the electronic configurations of the participating H, Sn, and Ru surface atoms. Via bond order, Bader charge, and topological analyses, we examined the changes in charge density which accompany the changes in the energy barriers. The main focus is on the bonds between the diffusing hydrogen atom and the three surrounding ruthenium atoms, because of their direct relevance to the transition from the surface *fcc* site to the subsurface site, and the analyses reveal trends in various characteristics of the Ru–H bonds in the initial adsorbed state (Table 3.2). The salient ones—energy barrier, reaction energy, atomic volume and bond order of the hydrogen atom—are plotted in Figure 3.6 for each diffusion scenario we explored. We find that the sum of bond orders for hydrogen is inversely proportional to the barrier to diffusion, while a smaller H atomic volume and more negative reaction energy correspond to lower diffusion barriers. We consider these trends and their implications in more detail in the Discussion section.

An illustration of one of the differences in bonding is provided in Figure 3.7. The topological analysis of the electron density distribution shows a symmetrical allocation of bonds between the H atom in the *fcc* position and three surrounding Ru atoms on the Ru(0001) surface (Figure 3.7a). The central triangle shows the extent of the electron density associated with the adsorbed H atom. When an  $\text{SnH}_4$  molecule is adsorbed on

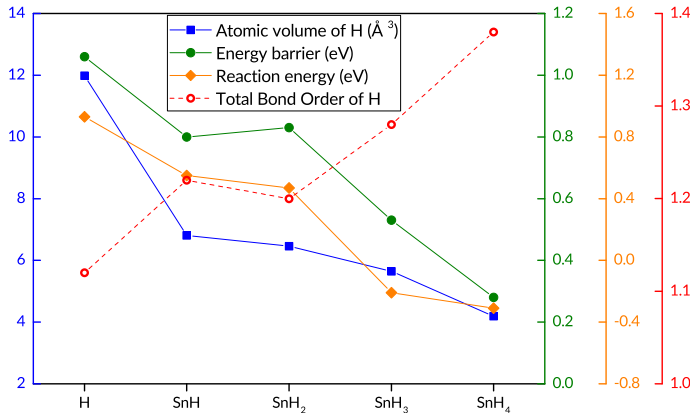


Figure 3.6: Energy barrier, formation energy, atomic volume and sum of the bond orders of the diffusing hydrogen atom in the initial state for each modelled diffusion scenario.

the surface, with one hydrogen atom oriented downwards, the bonds formed between the ruthenium atoms and the hydrogen atom are nearly identical to those formed by the lone H atom, with the important difference being the bond critical points' location closer to the hydrogen atom; the triangle demarcating the H atom's basin is perceptibly smaller in area in Figure 3.7c (SnH<sub>4</sub> on Ru) than in Figure 3.7a (H on Ru). This indicates that the charge associated with the hydrogen atom is located in a smaller region, and this is confirmed by the calculated atomic volume of hydrogen (Table 3.2, Figure 3.6). In the transition state, in which the hydrogen atom is surrounded by three (3) Ru atoms in the plane of the Ru(0001) surface, the electron density concentrated around the diffusing hydrogen atom is confined within similar size volumes, irrespective of the structure considered (Figure 3.7d–f).

Table 3.2: Characteristics of diffusing H atom and bonds between H atom and surrounding Ru surface atoms in the initial state. Values for SnH<sub>2</sub>\* do not correspond to clearly-defined initial and transition states (see text). Inter-atomic distances ( $d_{H-Ru}$ ), bond critical point (BCP) distances ( $d_{H-BCP}$ ), electron density and its Laplacian at BCPs are average values for 3 Ru–H bonds. Net atomic charge (NAC) for Ru is sum over 4 surface Ru atoms in (2 × 2) unit cell.

	$d_{H-Ru}/$ $d_{H-BCP}$ [Å]	Total Bond Order	Electron Density	Laplacian	Bader Volume [Å <sup>3</sup> ]	NAC			$\Delta E$ [eV]	Barrier [eV]
						H	Ru	Sn		
H	1.90/0.69	1.12	0.50	2.79	11.98	-0.051	-0.01	-	0.93	1.06
SnH	1.89/0.68	1.22	0.50	3.59	6.81	-0.059	-0.26	0.22	0.55	0.80
SnH <sub>2</sub>	1.88/0.68	1.20	0.52	3.56	6.46	-0.061	-0.20	0.25	0.47	0.83
SnH <sub>3</sub>	1.89/0.68	1.28	0.51	3.53	5.65	-0.075	-0.14	0.33	-0.21	0.53
SnH <sub>4</sub>	1.82/0.63	1.38	0.56	3.86	4.19	-0.062	-0.23	0.57	-0.31	0.28
SnH <sub>2</sub> *	1.93/0.70	1.54	0.45	3.54	3.54	-0.061	-0.20	0.25	-	-

Charge density difference ( $\Delta\rho$ ) plots paint a three-dimensional picture of the influ-

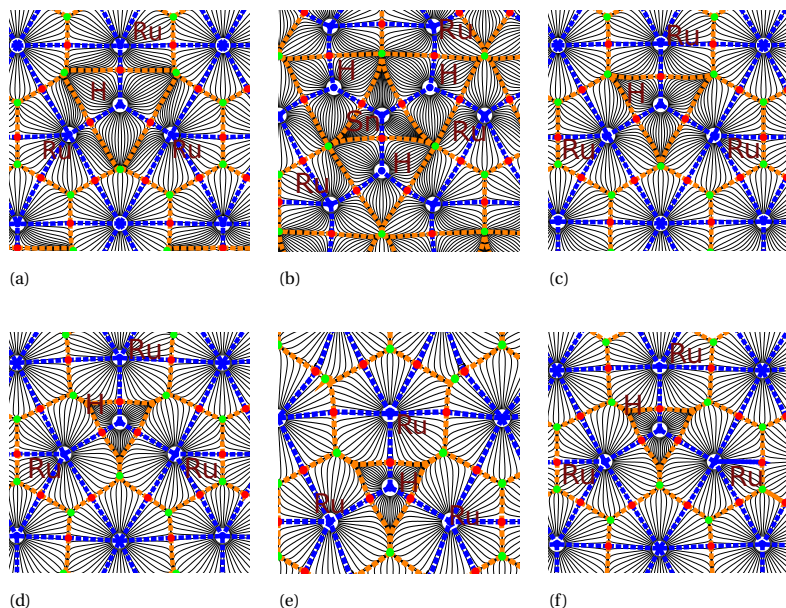


Figure 3.7: Topological analysis of the electron density for (a–c) H on Ru(0001), SnH<sub>3</sub> on Ru, and SnH<sub>4</sub> on Ru, respectively; (d–f) transition states with H from the adsorbate (H, SnH<sub>3</sub>, and SnH<sub>4</sub> respectively) between three ruthenium surface atoms. The figures show the horizontal plane through the diffusing hydrogen atom. Atomic basins are circumscribed by dashed orange lines. Within each atomic basin, the blue dot marks the position of the nucleus. Bond paths are shown with dashed blue lines. Along each bond path, the red dot represents the bond critical point (BCP). The green dots represent the ring critical points.

ence of tin on the charge density distribution. Figure 3.8 shows the charge difference for the initial and transition states for the H, SnH<sub>3</sub>, and SnH<sub>4</sub> cases. In Figure 3.8a, which shows an adsorbed H atom at the *fcc* site on the Ru(0001) surface, the H atom is surrounded by a region of accumulation; this indicates a net transfer of charge density to the hydrogen from the areas of depletion around the three surrounding Ru atoms. There are also small regions of increased density near the Ru atoms, beneath the surface. The transition state in Figure 3.8d is quite similar, with smaller regions of depletion on the Ru atoms. For the SnH<sub>4</sub> case (Figure 3.8c,d), the charge density donated to the hydrogen's 1s orbital is taken not only from the ruthenium, but in large part from the region between the H and Sn atoms. This points to the transfer of charge to the more electronegative hydrogen. Furthermore, the small regions of charge accumulation on the Ru atoms are now positioned above the ruthenium surface. The transition state shows redistribution of the charge to regions between the Ru atoms and the Sn atom, with a large depletion region above the penetrating H atom.

Due to the number of atoms on the ruthenium surface, SnH<sub>3</sub> on Ru presents the most complex interactions, which is evident from Figure 3.8b,e. The donation to the hydrogen is again present, but the source of the transferred charge is different. Each ruthenium

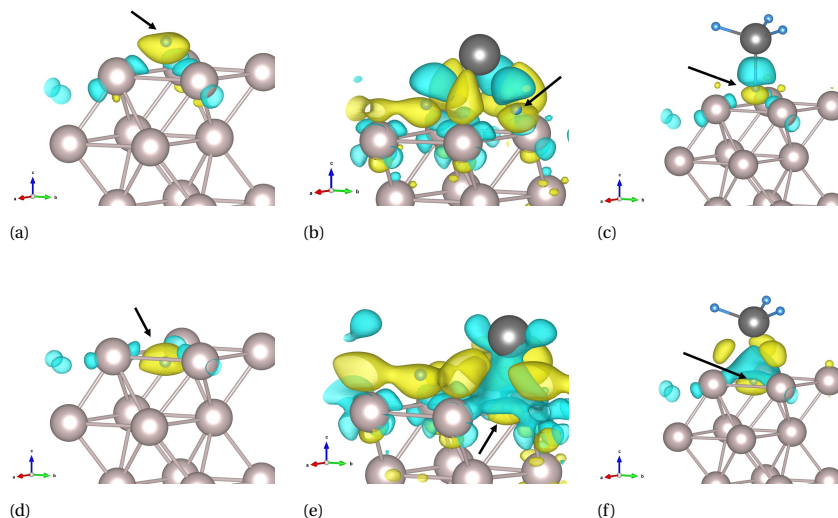


Figure 3.8: Charge difference for (a–c) H on Ru(0001), SnH<sub>3</sub> on Ru, and SnH<sub>4</sub> on Ru, respectively; (d–f) transition states with H from the adsorbate (H, SnH<sub>3</sub>, and SnH<sub>4</sub>, respectively) between three ruthenium surface atoms. In all the figures, the yellow isosurface is for charge density  $-0.004 \text{ e } \text{Å}^{-3}$ , and shows regions of charge accumulation, while the cyan is for  $+0.004 \text{ e } \text{Å}^{-3}$ , and shows regions of charge depletion. The black arrow shows the location of the diffusing hydrogen atom.

nium atom on the surface has several small depletion zones, but the charge redistribution has resulted in large accumulation zones between the Sn atom and the surrounding Ru atoms, interleaved with depletion zones above the adsorbed hydrogen atoms, which are also surrounded by areas of increased charge density. There appears to be significant charge transfer from the Sn atom, both to the hydrogen atoms and the surface ruthenium atoms. In the transition state, a large depletion zone similar to that found in Figure 3.8f is found above the diffusing hydrogen atom, also surrounded by zones of increased charge density. The implication is that electron–electron repulsion in the SnH<sub>3</sub> and SnH<sub>4</sub> cases makes the transition state more accessible, and makes the end state more energetically favourable, which is reflected in the exothermic nature of the reactions.

Using the LOBSTER code [51], we performed density-of-states and COHP/COOP calculations. We extracted the total and projected densities of states for the various cases and computed the orbitalwise COHP and COOP for the hydrogen atom and the surface ruthenium atoms. In Figure 3.9, we present the projected densities of states (PDOS) curves for the *d*-band electrons of the ruthenium atoms on the surface, with different adsorbates; the COHP for the interaction between the key hydrogen atom and one of the three surrounding ruthenium atoms are also given.

The main differences in the density-of-states can be observed in the lowest energy levels (below  $-5 \text{ eV}$ ), where the adsorbed hydrogen and tin atoms cause the appearance and/or shift of peaks. The centre of the *d* band distribution is lower when the Sn atom

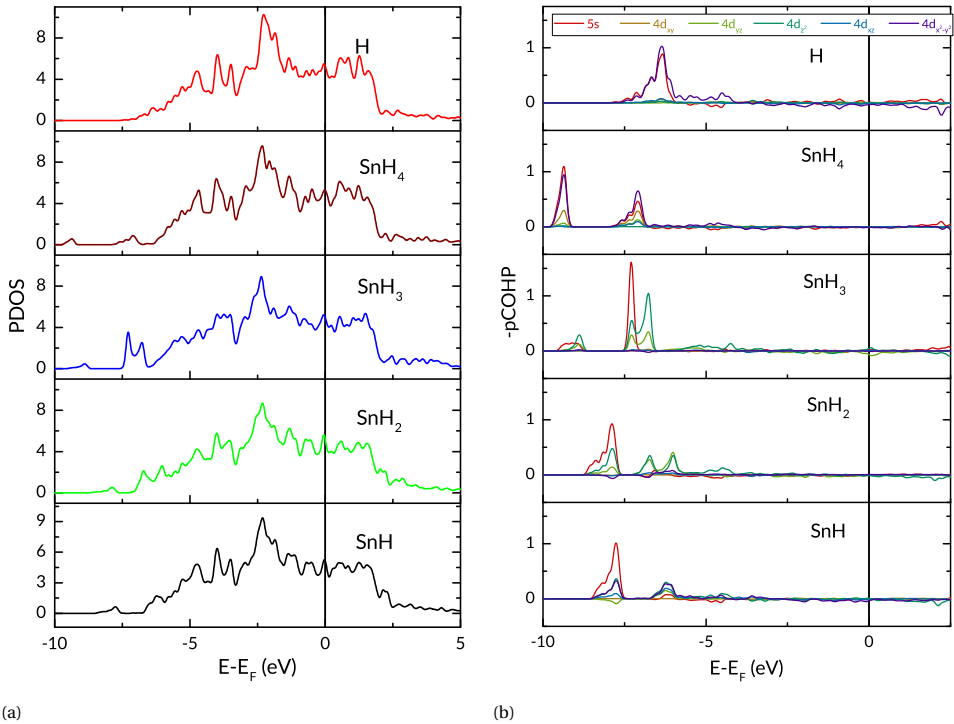


Figure 3.9: (a) projected Density of States for  $d$ -band of ruthenium surface atoms with different adsorbates; and (b) projected COHP for Ru–H interaction. i.e., one ruthenium atom and the adsorbed hydrogen atom. For clarity, the COHP for the weakest interactions are not shown. In all cases, the initial structure is considered.

is adsorbed on the Ru(0001) surface, and moves progressively lower with the adsorption of more hydrogen atoms. The  $d$  band width increases as the band centre is shifted downward. In the COHP plots ( $-p\text{COHP}$ , to be precise), significant differences can be seen in the orbitals which contribute to the bonding between the atoms. We show in Figure 3.9 the COHP for the key hydrogen atom and one of the surface Ru atoms surrounding it. Whereas both the  $5s$  and  $4d_{x^2-y^2}$  orbitals dominate the bonding and very slight anti-bonding populations for the H and SnH<sub>4</sub> adsorbates, the  $5s$  contribution is much reduced for the other cases with a tin atom on the ruthenium surface, in which the  $4d_{z^2}$  interaction with the hydrogen comes to prominence as more hydrogen atoms are added. The COHP for the other Ru–H pairs in the same scenario are not necessarily identical to those in Figure 3.9 because the tin affects the surrounding Ru atoms to different degrees, based on their distance and arrangement. Taken together, the COHP and the  $\Delta\rho$  plots of Figure 3.8 confirm that the electrons participating in the bonding generally originate from different orbitals for different adsorbates. This is especially apparent when the SnH<sub>3</sub> case is compared to the others.

### 3.4. DISCUSSION

A number of observations can be made upon comparing the results of the charge density analyses with the results of the NEB calculations (Table 3.2). First, it can be seen that the energy barrier is higher when the distance between the adsorbed H atom and each of the surface Ru atoms is greater; topological analyses show that the same is true for the distance between the H atom and the bond critical point. The difference is not stark: the adsorbed SnH<sub>4</sub> has the hydrogen atom in the *fcc* site at an average distance 4% smaller than the average distance between a lone H atom and the surrounding Ru atoms; the difference in the H-BCP distance is 9%. The barrier–distance relationship is not necessarily enough to predict a difference in energy barriers, since the three cases with Sn coadsorbed with H on the surface (SnH, SnH<sub>2</sub>, and SnH<sub>3</sub> in Table 3.2) have the same bond lengths and BCP distances, but different barriers to penetration.

A second, clearer correlation can be observed between the total bond order of the hydrogen atom and the calculated energy barrier. Taking into account all of the bonds in which the hydrogen atom of interest participates, we have calculated the sum of bond orders, and find that the changes in this value correspond to the changes in energy barrier quite neatly: a larger total bond order for H corresponds to a lower subsurface penetration barrier. The total bond order of the hydrogen atom in the SnH and SnH<sub>2</sub> cases are quite close, 1.22 and 1.20, respectively, as are the energy barriers, 0.80 and 0.83 eV, respectively. Moreover, the inverse proportionality is maintained. The trend holds for all the examined scenarios, suggesting that a key factor in the observed barrier differences is the state of the adsorbed and subsequently diffusing hydrogen atom itself, as characterised by its bonds and associated electron density.

The results of Bader charge analysis on the charge density shows a third trend, which relates the charge density distribution and the energy barrier. Recall that Bader's definition of an atom uses zero-flux surfaces to divide atoms, thereby associating a certain region of the electronic charge density with each atom in the system. In our system, the atomic volume computed for the adsorbed H atom of interest is generally larger for the cases with higher energy barriers, with the smallest volume corresponding to the lowest energy barrier. This supports the inference that the smaller atomic volume of H in a certain adsorption mode leads to a lower energy barrier to subsequent diffusion into the subsurface.

We can discern yet another link when comparing the energy barriers to the reaction energies, i.e., the total energy difference between the initial adsorbed state and the final state with hydrogen in the subsurface. Whereas the subsurface penetration event is endothermic for a hydrogen atom on Ru(0001), it is made progressively less so in the presence of tin, and is ultimately exothermic when the hydrogen is taken from a stannane molecule. Moreover, as seen in Figure 3.4, the SnH<sub>3</sub> and SnH<sub>4</sub> cases have early transition states, which contrasts with the late transition states of the other cases.

We note that some of the other characteristics we examined do not show such a clear trend when taken in isolation. For instance, the charge on the H atom as calculated by

the Bader method does not match the trend in energy barriers. The trend of net atomic charges (NAC) calculated via the DDEC6 approach is also inconclusive, as are the trends of electronic density (ED) and charge density Laplacians at the bond critical point. Nevertheless, viewed together with the trends found in the hydrogen BCP, bond order, and atomic volume, these characteristics indicate that the hydrogen atom is in a state with more localised charge in the scenarios with lower penetration barriers. In the transition states, the area of the triangle formed by the surrounding ruthenium atoms is in fact smaller for the  $\text{SnH}_4$  case than for the lone hydrogen atom. It appears that the localisation of the charge around the H nucleus is of more importance than the actual charge on the atom.

We speculate that the lower electronegativity of tin (1.96) relative to hydrogen (2.2) leads to the more compact localisation of charge around the hydrogen nucleus, i.e., the shared electrons are drawn closer to the hydrogen atom, which results in the reduced atomic volume found in our calculations. The introduction of tin results in charge transfer to the hydrogen atom, which can be seen in the more negative values of net atomic charge (NAC in Table 3.2) of the hydrogen atom in the scenarios with tin. Ruthenium's electronegativity is 2.2, equal to that of hydrogen, and the ruthenium atoms also show a more negative net atomic charge when tin is present. The tin atom therefore donates charge to the hydrogen and ruthenium atoms, as made evident by its positive NAC, and the charge accumulation above the ruthenium surface pushes the hydrogen into the surface due to electron–electron repulsion. The charge accumulation and repulsion also account for the preference of hydrogen for adsorption sites farther from tin, as seen in Section 3.3.3. The lower electronegativity of tin has also been put forward as the key factor in the difficulty of tin removal from ruthenium using hydrogen [60].

The barrier-less penetration of the Ru(0001) surface by the hydrogen atom from the vertically-oriented  $\text{SnH}_2$  appears to support the conclusion that the hydrogen atom is in a decisively different state of bonding and charge localisation when the subsurface penetration is more facile. Both the total bond order and Bader volume (see Table 3.2) suggest that the energy barrier would be lower in this case than in the  $\text{SnH}_4$  scenario; the bond order is 1.54, the highest value, while the Bader volume is 3.54, the lowest value. The charge difference ( $\Delta\rho$ ) in the initial geometry of the relaxation also shows charge accumulation around the hydrogen and above the ruthenium surface, in a manner similar to the transition state for  $\text{SnH}_4$ . Indeed, this calculation finds its local minimum with the hydrogen atom below the surface, showing that the hydrogen atom attached to tin is in a most advantageous state for passing through the surface ruthenium atoms.

These results together indicate that a closer, shorter bond exists between the hydrogen atom and the surface ruthenium atoms in the presence of tin, with a smaller atomic volume for the H atom in the adsorbed state, which is corroborated by the trend in calculated Bader volumes. The surrounding ruthenium atoms are moved apart to a lesser extent (smaller change in area of the triangle, see Table 3.2) to arrive at the transition state, i.e., at a lower energy cost. The reduced atomic volume is likely due to the asymmetric

charge distribution relative to the less electronegative tin. The charge transfer from tin to hydrogen and ruthenium creates areas of charge accumulation around the hydrogen atom and on the ruthenium surface, and makes the subsurface interstitial site more energetically favourable. These conditions are most advantageous for the adsorbed  $\text{SnH}_3$  and  $\text{SnH}_4$ , with the result that the penetration of hydrogen is easiest in these cases.

### 3.5. CONCLUSIONS

In this work, we have investigated hydrogen penetration of the Ru(0001) surface in the presence and absence of tin, by means of DFT computations, chemical bonding, and charge density analysis. We showed that hydrogen faces a significant barrier to subsurface penetration in the absence of tin. We find that the energy barrier drops significantly in the presence of tin, be it as an adatom or as part of an adsorbed tin hydride molecule. The lowest energy barriers are found when a hydride molecule adsorbs on the Ru(0001) surface and subsequently loses a hydrogen atom. We performed charge density analyses on systems with and without tin, which revealed changes in the bonds formed between ruthenium and hydrogen under the influence of tin, as well as a change in charge distribution around the diffusing hydrogen atom, resulting in reduced energy barriers to penetration. The much higher barrier found for a hydrogen atom with no tin present allows us to conclude that tin hydrides play an important role in the increased blistering of EUV reflectors with tin debris on the surface.

These insights into the effect of charge transfer from tin have important implications for the development of blistering mitigation techniques, and prolonging the operational lifetime of EUV optics. Our findings may also have value in cases where hydrogen penetration needs to be improved, such as hydrogen storage or separation and purification.

**REFERENCES**

- [1] G. C. Bond, G. Webb, P. B. Wells, and J. M. Winterbottom, *Patterns of behavior in catalysis by metals*, Journal of Catalysis **1**, 74 (1962).
- [2] J. H. Sinfelt, *Heterogeneous catalysis by metals*, Progress in Solid-State Chemistry **10**, 55 (1975).
- [3] A. G. Knapton, *Palladium Alloys for Hydrogen Diffusion Membranes*. Platinum Metals Review **21**, 44 (1977).
- [4] N. A. Al-Mufachi, N. V. Rees, and R. Steinberger-Wilkens, *Hydrogen selective membranes: A review of palladium-based dense metal membranes*, Renewable and Sustainable Energy Reviews **47**, 540 (2015).
- [5] B. Sakintuna, F. Lamari-Darkrim, and M. Hirscher, *Metal hydride materials for solid hydrogen storage: A review*, International Journal of Hydrogen Energy **32**, 1121 (2007).
- [6] T. Hübert, L. Boon-Brett, G. Black, and U. Banach, *Hydrogen sensors - A review*, Sensors and Actuators, B: Chemical **157**, 329 (2011).
- [7] D. Herlach, C. Kottler, T. Wider, and K. Maier, *Hydrogen embrittlement of metals*, Physica B: Condensed Matter **290**, 443 (2000).
- [8] N. E. Nanninga, Y. S. Levy, E. S. Drexler, R. T. Condon, A. E. Stevenson, and A. J. Slifka, *Comparison of hydrogen embrittlement in three pipeline steels in high pressure gaseous hydrogen environments*, Corrosion Science **59**, 1 (2012).
- [9] U. Muschiol, P. K. Schmidt, and K. Christmann, *Adsorption and absorption of hydrogen on a palladium (210) surface: A combined LEEDS, TDS,  $\Delta\Phi$  and HREELS study*, Surface Science **395**, 182 (1998).
- [10] P. Nordlander, S. Holloway, and J. K. Nørskov, *Hydrogen adsorption on metal surfaces*, Surface Science **136**, 59 (1984).
- [11] M. A. Pick and K. Sonnenberg, *A model for atomic hydrogen-metal interactions - application to recycling, recombination and permeation*, Journal of Nuclear Materials **131**, 208 (1985).
- [12] S. M. Myers, P. M. Richards, W. R. Wampler, and F. Besenbacher, *Ion-beam studies of hydrogen-metal interactions*, Journal of Nuclear Materials **165**, 9 (1989).
- [13] R. A. Van Santen and I. Tranca, *How molecular is the chemisorptive bond?* Physical Chemistry Chemical Physics **18**, 20868 (2016).
- [14] J. H. Sinfelt, *Catalysis by Alloys and Bimetallic Clusters*, Accounts of Chemical Research **10**, 15 (1977).

- [15] J. A. Rodriguez, *Electronic and chemical properties of Pt, Pd and Ni in bimetallic surfaces*, *Surface Science* **345**, 347 (1996).
- [16] A. Ruban, B. Hammer, P. Stoltze, H. L. Skriver, and J. K. Nørskov, *Surface electronic structure and reactivity of transition and noble metals*, *Journal of Molecular Catalysis A: Chemical* **115**, 421 (1997).
- [17] J. G. Chen, C. A. Menning, and M. B. Zellner, *Monolayer bimetallic surfaces: Experimental and theoretical studies of trends in electronic and chemical properties*, *Surface Science Reports* **63**, 201 (2008).
- [18] Y. B. He, A. Goriachko, C. Korte, A. Farkas, G. Mellau, P. Dudin, L. Gregoratti, A. Barinov, M. Kiskinova, A. Stierle, N. Kasper, S. Bajt, and H. Over, *Oxidation and reduction of ultrathin nanocrystalline Ru films on silicon: Model system for Ru-capped extreme ultraviolet lithography optics*, *Journal of Physical Chemistry C* **111**, 10988 (2007).
- [19] S. Bajt, H. N. Chapman, N. Nguyen, J. B. Alameda, J. C. Robinson, M. E. Malinowski, E. Gullikson, A. Aquila, C. Tarrio, and S. Grantham, *Design and performance of capping layers for EUV multilayer mirrors*, *Proc. SPIE* **5037**, 236 (2003).
- [20] A. S. Kuznetsov, R. W. E. van de Kruijs, M. A. Gleeson, K. Schmid, and F. Bijkerk, *Hydrogen interaction with EUVL-relevant optical materials*, *Journal of Surface Investigation. X-ray, Synchrotron and Neutron Techniques* **4**, 563 (2010).
- [21] A. S. Kuznetsov, M. A. Gleeson, and F. Bijkerk, *Temperature dependencies of hydrogen-induced blistering of thin film multilayers*, *Journal of Applied Physics* **115**, 173510 (2014).
- [22] N. Faradzhev and V. Sidorkin, *Hydrogen mediated transport of Sn to Ru film surface*, *Journal of Vacuum Science & Technology A: Vacuum, Surfaces, and Films* **27**, 306 (2009).
- [23] C. Bruneau and P. H. Dixneuf, *Topics in Organometallic Chemistry*, *Topics in Organometallic Chemistry*, Vol. 48 (Springer International Publishing, 2014).
- [24] R. D. Adams and E. Trufan, *Ruthenium-tin cluster complexes and their applications as bimetallic nanoscale heterogeneous hydrogenation catalysts*, *Philosophical Transactions of the Royal Society A: Mathematical, Physical and Engineering Sciences* **368**, 1473 (2010).
- [25] E. Bonnefille, F. Novio, T. Gutmann, R. Poteau, P. Lecante, J. C. Jumas, K. Philippot, and B. Chaudret, *Tin-decorated ruthenium nanoparticles: A way to tune selectivity in hydrogenation reaction*, *Nanoscale* **6**, 9806 (2014).

- [26] S. Galvagno, A. Donato, G. Neri, R. Pietropaolo, and G. Capannelli, *Selective hydrogenation of cinnamaldehyde over Ru-Sn catalysts*, *Journal of Molecular Catalysis* **78**, 227 (1993).
- [27] A. Gallo, C. Pirovano, M. Marelli, R. Psaro, and V. Dal Santo, *Hydrogen production by glycerol steam reforming with ru-based catalysts: A study on sn doping*, *Chemical Vapor Deposition* **16**, 305 (2010).
- [28] A. Driessen, P. Sanger, H. Hemmes, and R. Griessen, *Metal hydride formation at pressures up to 1 Mbar*, *Journal of Physics: Condensed Matter* **2**, 9797 (1990).
- [29] J. T. Yates, C. H. Peden, J. E. Houston, and D. W. Goodman, *Subsurface penetration of chemisorbed hydrogen isotopes into the Ru(0001) crystal surface*, *Surface Science* **160**, 37 (1985).
- [30] C. H. F. Peden, D. W. Goodman, J. E. Houston, and J. T. Yates, *Subsurface hydrogen on Ru(0001): Quantification by Cu titration*, *Surface Science* **194**, 92 (1988).
- [31] M. Lagos, *Subsurface bonding of hydrogen to metallic surfaces*, *Surface Science* **122**, L601 (1982).
- [32] G. Kresse and J. Hafner, *Ab initio molecular-dynamics simulation of the liquid-metalamorphous- semiconductor transition in germanium*, *Physical Review B* **49**, 14251 (1994).
- [33] G. Kresse and J. Furthmüller, *Efficiency of ab-initio total energy calculations for metals and semiconductors using a plane-wave basis set*, *Computational Materials Science* **6**, 15 (1996).
- [34] D. Joubert, *From ultrasoft pseudopotentials to the projector augmented-wave method*, *Physical Review B - Condensed Matter and Materials Physics* **59**, 1758 (1999).
- [35] J. D. Perdew, K. Burke, and M. Ernzerhof, *Generalized Gradient Approximation Made Simple*, *Physical Review Letters* **77**, 3865 (1996).
- [36] S. Grimme, J. Antony, S. Ehrlich, and H. Krieg, *A consistent and accurate ab initio parametrization of density functional dispersion correction (DFT-D) for the 94 elements H-Pu*, *The Journal of Chemical Physics* **132**, 154104 (2010).
- [37] G. Henkelman, B. P. Uberuaga, and H. Jónsson, *Climbing image nudged elastic band method for finding saddle points and minimum energy paths*, *Journal of Chemical Physics* **113**, 9901 (2000).
- [38] H. King, *Crystal structures and lattice parameters of allotropes of the elements*, in *CRC Handbook of Chemistry and Physics* (CRC Press, 2012) pp. 15–18.

- [39] G. H. Vineyard, *Frequency factors and isotope effects in solid state rate processes*, Journal of Physics and Chemistry of Solids **3**, 121 (1957).
- [40] K. K. Irikura, *Experimental Vibrational Zero-Point Energies: Diatomic Molecules*, Journal of Physical and Chemical Reference Data **36**, 389 (2007).
- [41] W. Tang, E. Sanville, and G. Henkelman, *A grid-based Bader analysis algorithm without lattice bias*, Journal of Physics: Condensed Matter **21**, 084204 (2009).
- [42] E. Sanville, S. D. Kenny, R. Smith, and G. Henkelman, *Improved grid-based algorithm for Bader charge allocation*, Journal of Computational Chemistry **28**, 899 (2007).
- [43] G. Henkelman, A. Arnaldsson, and H. Jónsson, *A fast and robust algorithm for Bader decomposition of charge density*, Computational Materials Science **36**, 354 (2006).
- [44] M. Yu and D. R. Trinkle, *Accurate and efficient algorithm for Bader charge integration*, The Journal of Chemical Physics **134**, 064111 (2011).
- [45] T. A. Manz and N. G. Limas, *Introducing DDEC6 atomic population analysis: Part 1. Charge partitioning theory and methodology*, RSC Advances **6**, 47771 (2016).
- [46] T. A. Manz, *Introducing DDEC6 atomic population analysis: Part 3. Comprehensive method to compute bond orders*, RSC Advances **7**, 45552 (2017).
- [47] D. Vega and D. Almeida, *AIM-UC: An application for QTAIM analysis*, Journal of Computational Methods in Sciences and Engineering **14**, 131 (2014).
- [48] R. Hoffmann, *Interaction of Orbitals through Space and through Bonds*, Accounts of Chemical Research **4**, 1 (1971).
- [49] R. Dronskowski and P. E. Blöchl, *Crystal orbital hamilton populations (COHP). Energy-resolved visualization of chemical bonding in solids based on density-functional calculations*, Journal of Physical Chemistry **97**, 8617 (1993).
- [50] V. L. Deringer, A. L. Tchougréeff, and R. Dronskowski, *Crystal orbital Hamilton population (COHP) analysis as projected from plane-wave basis sets*, Journal of Physical Chemistry A **115**, 5461 (2011).
- [51] S. Maintz, V. L. Deringer, A. L. Tchougréeff, and R. Dronskowski, *LOBSTER: A tool to extract chemical bonding from plane-wave based DFT*, Journal of Computational Chemistry **37**, 1030 (2016).
- [52] C. F. Matta and R. J. Boyd, *An Introduction to the Quantum Theory of Atoms in Molecules*, in *The Quantum Theory of Atoms in Molecules* (Wiley-VCH Verlag GmbH & Co. KGaA, Weinheim, Germany, 2007) pp. 1–34.

- [53] R. F. W. Bader, *A quantum theory of molecular structure and its applications*, Chemical Reviews **91**, 893 (1991).
- [54] I. M. Ciobica, A. W. Kleyn, and R. A. Van Santen, *Adsorption and coadsorption of CO and H on ruthenium surfaces*, Journal of Physical Chemistry B **107**, 164 (2003).
- [55] I. Del Rosal, L. Truflandier, R. Poteau, and I. C. Gerber, *A density functional theory study of spectroscopic and thermodynamic properties of surfacic hydrides on Ru(0001) model surface: The influence of the coordination modes and the coverage*, Journal of Physical Chemistry C **115**, 2169 (2011).
- [56] M. Luppi, R. A. Olsen, and E. J. Baerends, *Six-dimensional potential energy surface for H<sub>2</sub> at Ru(0001)*, Phys. Chem. Chem. Phys. **8**, 688 (2006).
- [57] L. Kristinsdóttir and E. Skúlason, *A systematic DFT study of hydrogen diffusion on transition metal surfaces*, Surface Science **606**, 1400 (2012).
- [58] E. M. McIntosh, K. T. Wikfeldt, J. Ellis, A. Michaelides, and W. Allison, *Quantum Effects in the Diffusion of Hydrogen on Ru(0001)*, The Journal of Physical Chemistry Letters **4**, 1565 (2013).
- [59] M. M. J. W. van Herpen, D. J. W. Klunder, W. A. Soer, R. Moors, and V. Banine, *Sn etching with hydrogen radicals to clean EUV optics*, Chemical Physics Letters **484**, 197 (2010).
- [60] M. Pachecka, J. M. Sturm, R. W. E. van de Kruijs, C. J. Lee, and F. Bijkerk, *Electronegativity-dependent tin etching from thin films*, AIP Advances **6**, 075222 (2016).
- [61] J. Fearon and G. W. Watson, *Hydrogen adsorption and diffusion on Pt {111} and PtSn {111}*, Journal of Materials Chemistry **16**, 1989 (2006).

# 4

## HYDROGEN DIFFUSION OUT OF RUTHENIUM — AN *ab initio* STUDY OF THE ROLE OF ADSORBATES

*Hydrogen permeation into mirrors used in extreme ultraviolet lithography results in the formation of blisters, which are detrimental to reflectivity. An understanding of the mechanism via which hydrogen ends up at the interface between the top ruthenium layer and the underlying bilayers is necessary to mitigate the blistering damage. In this study, we use Density Functional Theory to examine the ways in which hydrogen, having entered the near-surface interstitial voids, can migrate further into the metal or to its surface. We show that with hydrogen and tin adsorbed on the ruthenium surface, diffusion to the surface is blocked for interstitial hydrogen in the metal, making diffusion further into the metal more likely than out-diffusion. This dependence on surface conditions matches and confirms similar findings on hydrogen permeation into metals. This suggests control and modification of surface conditions as a way to influence hydrogen retention and blistering.<sup>1</sup>*

---

<sup>1</sup>This chapter has been published as: Onwudinanti, C., Brocks, G., Koelman, V., Morgan, T., & Tao, S. (2020). Hydrogen diffusion out of ruthenium—an *ab initio* study of the role of adsorbates. *Physical Chemistry Chemical Physics*, 22(15), 7935–7941. <https://doi.org/10.1039/d0cp00448k>

## 4.1. INTRODUCTION

There are several things that can happen when a metal is exposed to hydrogen. A certain amount of the gas will usually adsorb on the metal surface, some may end up absorbed into the interstitial sites in the metal's crystal lattice, and in some cases the metal bonds with the hydrogen to form metal hydrides. The extent to which each of these possibilities occurs depends on the metal involved, and the amount and state of the hydrogen supplied to it. This metal-hydrogen interaction is of great importance for a number of technological systems, spanning a wide range from heterogeneous catalysis[1] to separation [2, 3], storage [4], and sensors [5]. Hydrogen plasma and metals also come in contact in nuclear fusion experiments and reactors[6].

The interaction of hydrogen and ruthenium has been studied extensively, particularly in the field of catalysis. In an altogether different technological application, the metal has found use as a capping layer on the multi-layer mirrors (MLMs) used in extreme ultraviolet (EUV) lithography[7, 8]. The MLM consists of 40-60 molybdenum/silicon bilayers, each about 6 to 7 nanometres thick, and is capped by a ruthenium layer. Tin plasma is the source of EUV photons for the lithographic system, and tin debris can be deposited on the mirror. Hydrogen is used as a buffer for the optics, and to etch away contaminants. It comes into contact with the metal, and may penetrate the surface. It can then diffuse through the bulk to the interface(s) of the multi-layer structure, where it recombines to form pockets of H<sub>2</sub> gas. When these pockets reach a critical pressure, the layers separate, resulting in blistering of the mirror and loss of reflectivity [9, 10]. This process appears to be facilitated by tin.

Ruthenium ought to be an ideal capping material, protecting the MLM against hydrogen. In addition to its suitable mechanical and optical properties, it also exhibits low H solubility[11]. Although H<sub>2</sub> dissociates and adsorbs on the surface[12], the resulting atoms do not penetrate the Ru lattice easily. In a previous publication[13], we reported that the energy of formation of interstitial hydrogen in ruthenium was found to be positive for both interstitial sites. Our calculations showed that the DFT-calculated energy barrier to subsurface penetration is large for hydrogen, but the presence of tin on the surface leads to a significant lowering of the barrier. These results, and the observed blistering after tin contamination, led to the question: since hydrogen exhibits low solubility in ruthenium, why does the hydrogen injected by tin (hydrides) remain in the ruthenium, and subsequently form blisters at the interface(s)?

We posit that the coverage of the ruthenium surface by adsorbates obstructs the exit of hydrogen from the near-surface region to the surface and the gas phase, thus playing an important role in the blistering process. A number of phenomena have their basis in such restriction of access to the surface. Livshits et al [14] linked superpermeability of a metal membrane to the presence of chemically active adlayers on the upstream surface. Carbon impurities in a hydrogen plasma were found to increase blistering in tungsten targets[15]. A palladium-gold alloy was shown to accumulate hydrogen in the near-surface region when the hydrogen exit path was affected by adsorbed CO[16]. This

effect also occurs without impurities; Soroka et al [17] proposed that the saturation of a ruthenium thin film surface with hydrogen inhibits hydrogen removal from the underlying yttrium hydride layer. In all these cases, the exit of hydrogen from the bulk metal is impeded by conditions on the surface which cause reduced bulk-to-surface diffusion, recombination, and desorption.

In this article, we examine the different paths and mechanisms through which hydrogen, having reached the interstitial sites in the metal, eventually leaves the bulk and ends up either in the gas phase above the ruthenium capping layer or in the pockets of molecular hydrogen which form the blisters. We show that the availability of sites on the metal surface plays a key role in the out-diffusion of hydrogen. Thus, saturation of the surface with adsorbed hydrogen hinders the removal of hydrogen from the bulk. Our calculations therefore indicate that near-complete coverage of the ruthenium surface will result in more hydrogen reaching the interface between the thin ruthenium layer and its substrate, where it can form blisters.

## 4.2. COMPUTATIONAL DETAILS

The results presented in this work are based on computations performed within the framework of DFT, as implemented in the Vienna Ab Initio Simulation Package (VASP)[18–20]. The calculations were performed with the generalized gradient approach as proposed by Perdew, Burke, and Ernzerhof (PBE)[21], with the following key convergence parameters: a kinetic energy cutoff of 400 eV, residual force criterion of  $1 \times 10^{-2}$  eV/Å, and a  $1 \times 10^{-5}$  eV energy convergence criterion. Slab calculations were performed with a  $(9 \times 9 \times 1)$   $\Gamma$ -centred  $k$ -points grid, while bulk calculations were done with a  $(9 \times 9 \times 9)$  grid; all atoms were allowed to relax in the optimization process. Transition state calculations were carried out using the Climbing Image Nudged Elastic Band (CINEB) algorithm[22], with a force criterion of  $1 \times 10^{-2}$  eV/Å and one (1) to five (5) intermediate geometries for the transition state search.

The calculated lattice parameters for hexagonal close-packed (hcp) ruthenium are  $a = 2.69$  Å and  $c/a = 1.58$ , which are in good agreement with experimental results, 2.71 Å and 1.58, respectively [23]. The Ru(0001) surface is modelled as a slab of seven layers using a  $(2 \times 2)$  cell, with  $\sim 15$  Å of vacuum between the periodic images in the  $z$ -direction. The number of layers and the vacuum height were found to give accurate results at reasonable computational cost — the calculated surface energy changes by less than 2% from 7 layers to 11 layers.

For hydrogen, the energy of adsorption is computed per the definition

$$E_{ads} = \frac{1}{n} \left( E_{nH,surf} - E_{surf} - \frac{n}{2} E_{H_2} \right), \quad (4.1)$$

where  $E_{nH,surf}$ ,  $E_{surf}$ , and  $E_{H_2}$  stand respectively for the total energies of the ruthenium slab with  $n$  adsorbed hydrogen atoms, clean ruthenium slab, and the energy of the hydrogen molecule. The formation energy of interstitial hydrogen, normalised to the

hydrogen concentration, is calculated according to the definition

$$\Delta E_{H_2} = \left( E_{M_x H_y} - x E_M - \frac{y}{2} E_{H_2} \right) / \frac{y}{2}, \quad (4.2)$$

where  $x, y$  are respectively the number of metal atoms and the number of hydrogen atoms, while  $E_{M_x H_y}$ ,  $E_M$ , and  $E_{H_2}$  stand respectively for the total energy of the metal hydride, the energy of each bulk metal atom, and the energy of a hydrogen molecule.

Due to the low mass of the hydrogen atom, its adsorption and diffusion behaviour is, in general, influenced by zero-point energy (ZPE). The ZPE is calculated by the relation

$$ZPE = \frac{\sum_i h \nu_i}{2}, \quad (4.3)$$

where  $\nu_i$  is a real normal mode frequency. The zero point energy for a hydrogen molecule ( $H_2$ ) calculated thus is 0.27 eV (0.135 eV per H atom), corresponding to a vibrational mode of  $4354 \text{ cm}^{-1}$ , in good agreement with the experimentally-determined value of  $4401 \text{ cm}^{-1}$  [24]. We have computed the ZPE for a hydrogen atom on the surface and in the interstitial sites, as well the transition states. The energy barriers reported in the subsequent chapters include ZPE corrections, which are also taken into account in the calculation of diffusion coefficients.

Diffusion coefficients are commonly expressed in the general form,

$$D = D_0 e^{\frac{-Q}{k_B T}}, \quad (4.4)$$

where  $D_0$  is a prefactor,  $Q$  is the activation energy,  $k_B$  is the Boltzmann constant, and  $T$  is the temperature. According to the approach proposed by Ishioka and Koiwa[25], two diffusion coefficients,  $D_{\perp}$  and  $D_{\parallel}$ , can be computed for interstitials with multiple jump frequencies in an hcp lattice with parameters  $a$  and  $c$ . These diffusion coefficients correspond to diffusion perpendicular to the  $c$  axis and parallel to it. The diffusion coefficients are obtained via the following formulae:

$$D_{\perp} = \frac{\omega_{TO}\omega_{OT}}{\omega_{TO} + 2\omega_{OT}} a^2 \quad (4.5)$$

$$D_{\parallel} = \frac{\omega_{TO}(3\omega_{OO}\omega_{TO} + 2\omega_{OO}\omega_{TT} + 3\omega_{TT}\omega_{OT})}{4(2\omega_{TT} + 3\omega_{TO})(\omega_{TO} + 2\omega_{OT})} c^2 \quad (4.6)$$

where  $a, c$  are the lattice parameters, and  $\omega_{xx} = \nu_{ij} e^{\frac{-E_b}{k_B T}}$  is the jump rate from one site to another, derived from  $\nu_{ij}$ , the effective frequency[26];  $E_b$ , the energy barrier;  $k_B$ , the Boltzmann constant; and  $T$ , the temperature. A linear fit of the diffusion coefficient curves against temperature gives the diffusion coefficient prefactors ( $D_{0\perp}$  and  $D_{0\parallel}$ ) and activation energies ( $Q_{\perp}$  and  $Q_{\parallel}$ ) according to the Arrhenius plot of Eq. 4.4.

### 4.3. RESULTS

## HYDROGEN ON THE SURFACE

Exposure of ruthenium to hydrogen will result in adsorption of hydrogen on the metal, and our study starts with consideration of adsorption. We choose to study the 0001 surface of ruthenium for two related reasons: first, this plane has the lowest surface energy, and will therefore dominate the exposed surface of a thin film; second, this surface is widely studied and represented in the literature, which allows a measure of validation of the computed energies and geometries.

The Ru(0001) surface offers a number of adsorption sites. Two of these sites, labelled *fcc* and *hcp* sites, allow three-fold coordination of H with surface Ru atoms, and have the most negative adsorption energies (see Figure 4.1). Indeed, all sites show negative adsorption energies, with the top site least favourable. The values remain negative at 100 % coverage, i.e. up to 1 H atom per surface Ru atom, with all *fcc* sites occupied. Previously-published first-principles calculations[27, 28] show a similar trend in energies of adsorption, with the slight variations in absolute values explained by differences in parameters and software used for the DFT calculations. We thus confirm that hydrogen adsorption on the ruthenium surface is favourable, and that exposing ruthenium to hydrogen will result in saturation of the surface by dissociated hydrogen atoms.

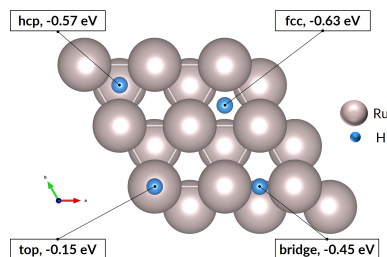


Figure 4.1: Adsorption sites for H on the Ru(0001) surface, with corresponding energies of adsorption.

## HYDROGEN IN THE BULK

Hydrogen in ruthenium is found as discrete atoms located in the interstices of the hexagonal close-packed lattice. An interstitial atom can occupy one of two sites, octahedral or tetrahedral, relative to the surrounding nearest neighbour metal atoms.

In the close-packed lattice, the octahedral sites, which are formed by 6 atoms at the vertices, are larger than the tetrahedral voids, formed by 4. The calculated formation energy of the interstitial hydride, shown at  $\frac{1}{54}$  concentration (H/Ru) in Figure 4.2, indicates that the octahedral site is preferable. Its 0.34 eV formation energy is much lower than the 0.84 eV of the tetrahedral site. For the subsurface octahedral site which we focus on subsequently, the energy value is nearly the same, 0.30 eV at  $\frac{1}{28}$  concentration; this is calculated for a slab, as opposed to the preceding bulk values. Nonetheless, we can conclude that the subsurface state is very similar to the bulk interstitial state. In general, the endothermic nature of interstitial hydride formation makes it unfavourable, and the

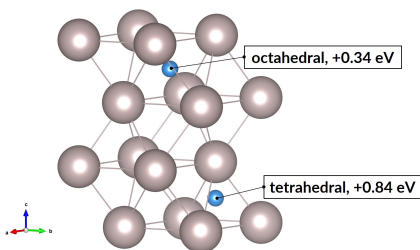


Figure 4.2: Interstitial sites and the corresponding hydride formation energies at hydrogen concentration (H/Ru) equal to  $\frac{1}{4}$ .

4

concentration of the interstitial hydrogen will remain low. An estimate of the fractional concentration of dissolved H atoms in ruthenium is  $10^{-9}$  relative to the gas, at 1 bar and room temperature; this is according to a lattice gas model with all H atoms in the lower-energy octahedral sites. The low solubility is confirmed by experimental data[11] and other computational studies[28].

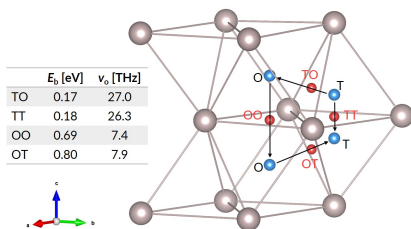


Figure 4.3: Jump paths, ZPE-corrected energy barriers, and effective frequencies for H in Ru. The blue spheres show the interstitial sites and the red spheres show transition states between the sites. Figure reproduced from Ref [13].

The elementary hops for hydrogen diffusion in the Ru lattice, as well as their effective frequencies and energy barriers are shown in Figure 4.3. We obtain for the diffusion prefactors the values  $D_{0\perp} = 1.44 \times 10^{-6} \text{ m}^2\text{s}^{-1}$  and  $D_{0\parallel} = 1.70 \times 10^{-7} \text{ m}^2\text{s}^{-1}$ . The corresponding activation energies are  $Q_{\perp} = 0.80 \text{ eV}$  and  $Q_{\parallel} = 0.69 \text{ eV}$ . Experimental values for hydrogen diffusion in ruthenium are lacking in the literature. However, our results are of comparable magnitude to those reported in *ab initio* studies for H diffusion in  $\alpha$ -titanium[29].

### HYDROGEN DIFFUSION IN THE NEAR-SURFACE REGION

A hydrogen atom in the first subsurface layer may diffuse in a number of directions, indicated by the arrows and labels in Figure 4.4: (1) within the subsurface layer, to an adjacent octahedral site (sideways); (2) to a deeper octahedral site (downwards); (3) to the surface (upwards). While the presence of hydrogen or tin (hydrides) on the metal surface

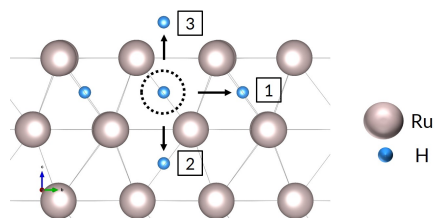


Figure 4.4: Diffusion paths for H atom in first Ru subsurface interstitial site. The sideways arrow shows one of six (6) possible diffusion paths within the same subsurface layer.

may alter the energies, barriers, and precise mechanics of the jumps, the picture remains essentially unchanged with respect to the possible migration paths. It should be noted that the tetrahedral sites may also be occupied by the interstitial atoms. However, due to the high energy of formation compared to the more stable octahedral sites, we have chosen to neglect the effect of tetrahedral site occupancy on the processes discussed.

4

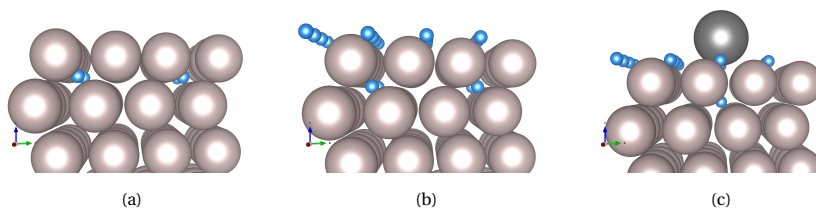


Figure 4.5: H in subsurface interstitial sites under a (a) clean Ru surface; (b) Ru surface with H adsorbed; and (c) Ru surface with Sn and H adsorbed.

We distinguish three main example surface/subsurface scenarios, and model the hydrogen atom jumps. As illustrated in Figure 4.5, these configurations are: (a) with the surface clear of hydrogen; (b) with adsorbed hydrogen; and (c) with adsorbed hydrogen and tin. For each case, the diffusion paths for the hydrogen atom in the subsurface are calculated using the Climbing Image Nudged Elastic Band (CINEB) algorithm. The results are presented in detail below, and summarised in Table 4.1.

#### **(a) Clean ruthenium surface**

The subsurface octahedral void is surrounded by six (6) identical voids in the same layer. The hydrogen atom may diffuse to any of these sites, across the same short distance and through identical transition states, if the surface and surrounding voids are not occupied. This diffusion step, with the Ru surface clean of adsorbates, is illustrated by Figure 4.6a; the energy barrier is 0.73 eV. Diffusion into the deeper bulk interstitial (downwards) is shown in Figure 4.6b. There is only one site directly accessible, and the barrier for this jump is slightly lower, at 0.78 eV. The H atom can also diffuse to the surface *fcc* site, as shown in Figure 4.6c, across the much lower barrier of 0.17 eV.

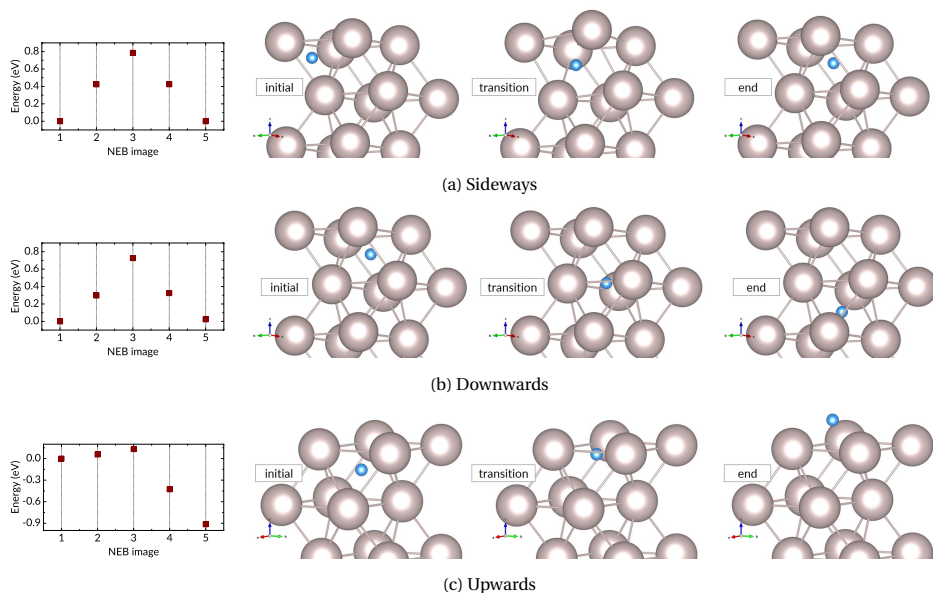


Figure 4.6: Diffusion paths for H atom in subsurface under a clean ruthenium surface. The results of 5-image NEB calculations, as well as initial, transition, and end states are shown for: (a) sideways diffusion within the layer; (b) downwards into a deeper layer; and (c) upwards to the surface.

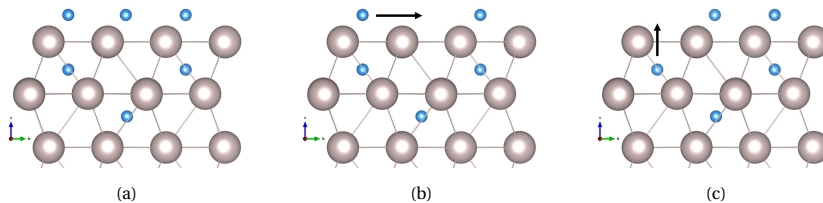


Figure 4.7: Multi-step diffusion from subsurface to surface. (a) Surface sites are all occupied, (b) adjacent site is vacated and adatom can move to it, (c) surface site is free and atom in interstitial site can move to the surface.

**(b) With hydrogen adsorbed**

The subsurface diffusion paths were simulated with 100% hydrogen coverage of the Ru(0001) surface, 1 H atom per surface Ru atom. Compared to the situation with a surface devoid of adsorbates, the interstitial hydrogen atom faces a similar energy barrier for diffusion within the layer, 0.78 eV, while the jump into a deeper octahedral void is over a reduced barrier of 0.48 eV. However, the path to the surface is blocked due to the occupation of the *fcc* site. Only upon diffusion or desorption of the adsorbed hydrogen can the subsurface hydrogen access the vacated site. An example of this multi-step dif-

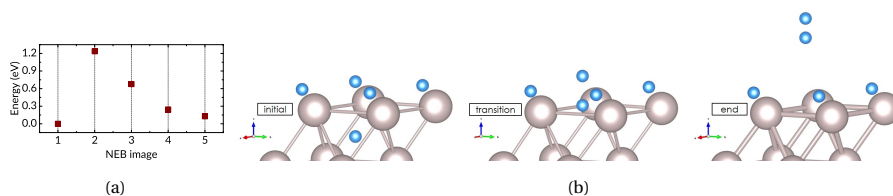


Figure 4.8: (a) The result of a 5-image NEB calculation; and (b) the initial, transition, and end states for associative desorption of hydrogen from subsurface octahedral and surface *fcc* sites, with 1 H atom adsorbed per surface Ru atom.

fusion to the surface is shown in Figure 4.7. As an alternative, the atom in the metal may recombine with the atom on the surface to form an H<sub>2</sub> molecule and desorb from the surface (Figure 4.8), but this entails overcoming a 1.20 eV energy barrier, much larger than the barrier for a solitary atom moving from subsurface to surface. Furthermore, with an otherwise clean surface and with all *fcc* sites occupied, this associative desorption ends in a state higher in energy than the starting point. In other words, the adsorbed atom is so low in energy ( $-0.63$  eV relative to a free H<sub>2</sub> molecule) that it compensates the energy cost of the interstitial atom ( $+0.34$  eV).

#### (c) With hydrogen and tin adsorbed

The energy barriers for the same three diffusion paths are changed further by the presence of tin on the surface. At this concentration – one tin atom per 16 ruthenium and 15 hydrogen – the energy barrier to deeper penetration into the metal is 0.56 eV. The sideways diffusion becomes more difficult, however, with its barrier now at 0.95 eV. This may be explained by the H atom interacting with the Sn atom on the surface. Most importantly, the associative desorption of hydrogen from the interstitial and surface sites faces a barrier of 1.89 eV. A direct comparison to the case with a clean Ru(0001) surface shows a starkly-changed energy landscape: the barrier to sideways diffusion within the near-surface layer is nearly twice as high as the barrier to deeper penetration, and the barrier to exit is even higher when no *fcc* site on the surface is free.

## 4.4. DISCUSSION

We have put forward a model of the diffusion of an H atom in the Ru lattice, focusing on the paths available to an atom in the near-surface region. Each of the diffusion steps presented in the preceding section faces its own peculiar combination of barriers and probabilities.

The sideways jump faces different barriers for the clear and occupied states of the surface, though the 0.05 eV difference is quite slight. In other words, the conditions for the atom diffusing within the layer are essentially unchanged by the presence of hydrogen on the surface. However, when Sn is present, this sideways diffusion changes: the barrier and  $\Delta E$  are higher. This is explained by the proximity of the Sn atom, as the

Table 4.1: Energy barriers to hydrogen diffusion from subsurface octahedral site.  $\Delta E$ , the difference in energy between the initial and end states, is given in brackets. The values in italics show associative desorption (AD) (see Figure 4.8).

	Energy barrier ( $\Delta E$ ) [eV]		
	clean surface	H adsorbed	H & Sn adsorbed
sideways	0.73 (+0.00)	0.78 (+0.00)	0.95 (+0.12)
downwards	0.78 (+0.02)	0.48 (−0.17)	0.56 (+0.06)
upwards	0.17 (−0.93)	-	-
<i>upwards (AD)</i>	-	<i>1.20 (+0.13)</i>	<i>1.89 (+0.03)</i>

4

change in energy is a result of the change in position relative to the Sn atom and its immediate neighbours.

Moving deeper into the bulk is a relatively simple one-step process, from one octahedral site to another, over a barrier of 0.48-0.78 eV. There is only one destination site, directly below the initial site. If this site happens to be occupied, this migration becomes impossible. This site is unlikely to be occupied, however, owing to the +0.34 eV formation energy and the consequent low solubility of H in Ru. It is notable that this downwards hop results in a lowering of energy (−0.17 eV) relative to the subsurface site when the surface is covered with hydrogen, tilting the situation in favour of deeper migration.

The interstitial atom can also move to the *fcc* site on the surface, over a barrier that is only 0.13 eV when the surface is clear of adsorbates. This is a much lower barrier than the others faced by the diffusing atom, much more likely to be scaled. Moreover, due to the lower total energy of the adsorbed state, this is an exothermic process, with the end state 0.93 eV lower in energy than the starting point in the interstitial site. However, this escape is contingent on the *fcc* site being unoccupied. In the case of an occupied surface site, the subsurface-to-surface transition becomes a multi-step process which must involve the vacation of a surface site for the H atom, due to diffusion or recombination. When there is a steady supply of H atoms and molecules to the surface (as is the case when the mirror is exposed to plasma), the interstitial H atom is also in competition for surface sites with this H supply. Each of these conditions reduces the probability of escape, and increases the likelihood of deeper penetration.

A similar site-blocking effect has been proposed to explain the retarded dissociation of  $YH_3$  under a Ru film[17]. Soroka et al observed that the unavailability of surface sites prevented the escape of hydrogen. By raising the temperature of the sample above the desorption temperature, the hydrogen atoms released from the  $YH_3$  layer were able to diffuse to the surface much more rapidly, allowing the decomposition of the yttrium trihydride to proceed. In this instance, only hydrogen adatoms were present. In other studies, the presence of other species, such as carbon or chemically active gases, will reinforce the blocking effect not just by occupying the surface but also by impeding the

recombination and desorption of hydrogen[14, 15].

In the case of a ruthenium thin film exposed to plasma containing a large fraction of atomic hydrogen, the availability of surface sites is limited. Hydrogen readily adsorbs on the ruthenium surface. This means that any hydrogen which ends up within the ruthenium faces an obstacle to escape. The “injection” of hydrogen into the subsurface is caused by the presence of tin, which lowers the penetration barrier[13]. The diffusion coefficients we have calculated indicate that hydrogen diffusion within the ruthenium proceeds at a rate similar to that of hydrogen in other metals, and poses no great obstacle. Tin on the surface also affects surface diffusion of hydrogen, i.e. it may reduce the rate at which sites are freed [13]. Thus the likelihood of diffusion to the interface and subsequent blistering is greatly increased when the concentration of hydrogen in the subsurface is significantly raised. In this way, the surface site blocking effect of hydrogen and tin plays a key role in the blistering of the ruthenium film. To be perfectly accurate in answering our initial question: the hydrogen which enters the ruthenium thin film does eventually leave; it simply ends up in the blisters at the opposite face.

## 4.5. CONCLUSION

In this article we have presented the case for the influence of surface saturation on hydrogen diffusion to the interface between a ruthenium thin film and its substrate, via an examination of the diffusion paths available to a hydrogen atom in the interstitial site just beneath a Ru(0001) surface. By performing transition state calculations of the key hydrogen migrations, we have shown a clear effect of surface occupancy on the energy barriers to diffusion of a hydrogen atom in the near-surface interstices. Our results indicate that the blocking of access to the surface results in increased likelihood of diffusion deeper into the metal lattice. In conjunction with the reduced energy barrier to subsurface penetration in the presence of tin, this effect leads to accumulation of hydrogen in the metal and interface, and subsequent blistering of the ruthenium thin film. This indicates that modifying and controlling the surface coverage may be an effective method of controlling the amount of hydrogen retained in the metal and underlying layers.

## REFERENCES

- [1] C. Bruneau and P. H. Dixneuf, *Topics in Organometallic Chemistry*, Topics in Organometallic Chemistry, Vol. 48 (Springer International Publishing, 2014).
- [2] A. G. Knapton, *Palladium Alloys for Hydrogen Diffusion Membranes*. Platinum Metals Review **21**, 44 (1977).
- [3] N. A. Al-Mufachi, N. V. Rees, and R. Steinberger-Wilkens, *Hydrogen selective membranes: A review of palladium-based dense metal membranes*, Renewable and Sustainable Energy Reviews **47**, 540 (2015).
- [4] B. Sakintuna, F. Lamari-Darkrim, and M. Hirscher, *Metal hydride materials for solid hydrogen storage: A review*, International Journal of Hydrogen Energy **32**, 1121 (2007).
- [5] T. Hübert, L. Boon-Brett, G. Black, and U. Banach, *Hydrogen sensors - A review*, Sensors and Actuators, B: Chemical **157**, 329 (2011).
- [6] Y. Ueda, J. Coenen, G. De Temmerman, R. Doerner, J. Linke, V. Philipps, and E. Tsitroni, *Research status and issues of tungsten plasma facing materials for ITER and beyond*, Fusion Engineering and Design **89**, 901 (2014).
- [7] Y. B. He, A. Goriachko, C. Korte, A. Farkas, G. Mellau, P. Dudin, L. Gregoratti, A. Barinov, M. Kiskinova, A. Stierle, N. Kasper, S. Bajt, and H. Over, *Oxidation and reduction of ultrathin nanocrystalline Ru films on silicon: Model system for Ru-capped extreme ultraviolet lithography optics*, Journal of Physical Chemistry C **111**, 10988 (2007).
- [8] S. Bajt, H. N. Chapman, N. Nguyen, J. B. Alameda, J. C. Robinson, M. E. Malinowski, E. Gullikson, A. Aquila, C. Tarrío, and S. Grantham, *Design and performance of capping layers for EUV multilayer mirrors*, Proc. SPIE **5037**, 236 (2003).
- [9] A. S. Kuznetsov, R. W. E. van de Kruijs, M. A. Gleeson, K. Schmid, and F. Bijkerk, *Hydrogen interaction with EUVL-relevant optical materials*, Journal of Surface Investigation. X-ray, Synchrotron and Neutron Techniques **4**, 563 (2010).
- [10] A. S. Kuznetsov, M. A. Gleeson, and F. Bijkerk, *Temperature dependencies of hydrogen-induced blistering of thin film multilayers*, Journal of Applied Physics **115**, 173510 (2014).
- [11] R. B. McLellan and W. A. Oates, *The solubility of hydrogen in rhodium, ruthenium, iridium and nickel*, Acta Metallurgica **21**, 181 (1973).
- [12] P. Feulner and D. Menzel, *The adsorption of hydrogen on ruthenium (001): Adsorption states, dipole moments and kinetics of adsorption and desorption*, Surface Science **154**, 465 (1985).

- [13] C. Onwudinanti, I. Tranca, T. Morgan, and S. Tao, *Tin, The Enabler—Hydrogen Diffusion into Ruthenium*, *Nanomaterials* **9**, 129 (2019).
- [14] A. I. Livshits, M. E. Notkin, and A. A. Samartsev, *Physico-chemical origin of super-permeability - Large-scale effects of surface chemistry on "hot" hydrogen permeation and absorption in metals*, *Journal of Nuclear Materials* **170**, 79 (1990).
- [15] Y. Ueda, T. Shimada, and M. Nishikawa, *Impacts of carbon impurities in hydrogen plasmas on tungsten blistering*, *Nuclear Fusion* **44**, 62 (2004).
- [16] S. Ogura, M. Okada, and K. Fukutani, *Near-surface accumulation of hydrogen and CO blocking effects on a Pd-Au alloy*, *Journal of Physical Chemistry C* **117**, 9366 (2013).
- [17] O. Soroka, J. M. Sturm, R. W. van de Kruijs, C. J. Lee, and F. Bijkerk, *Control of YH<sub>3</sub> formation and stability via hydrogen surface adsorption and desorption*, *Applied Surface Science* **455**, 70 (2018).
- [18] G. Kresse and J. Hafner, *Ab initio molecular-dynamics simulation of the liquid-metalamorphous- semiconductor transition in germanium*, *Physical Review B* **49**, 14251 (1994).
- [19] G. Kresse and J. Furthmüller, *Efficiency of ab-initio total energy calculations for metals and semiconductors using a plane-wave basis set*, *Computational Materials Science* **6**, 15 (1996).
- [20] D. Joubert, *From ultrasoft pseudopotentials to the projector augmented-wave method*, *Physical Review B - Condensed Matter and Materials Physics* **59**, 1758 (1999).
- [21] J. D. Perdew, K. Burke, and M. Ernzerhof, *Generalized Gradient Approximation Made Simple*, *Physical Review Letters* **77**, 3865 (1996).
- [22] G. Henkelman, B. P. Uberuaga, and H. Jónsson, *Climbing image nudged elastic band method for finding saddle points and minimum energy paths*, *Journal of Chemical Physics* **113**, 9901 (2000).
- [23] H. King, *Crystal structures and lattice parameters of allotropes of the elements*, in *CRC Handbook of Chemistry and Physics* (CRC Press, 2012) pp. 15–18.
- [24] K. K. Irikura, *Experimental Vibrational Zero-Point Energies: Diatomic Molecules*, *Journal of Physical and Chemical Reference Data* **36**, 389 (2007).
- [25] S. Ishioka and M. Koiwa, *Diffusion coefficient in crystals with multiple jump frequencies*, *Philosophical Magazine A: Physics of Condensed Matter, Structure, Defects and Mechanical Properties* **52**, 267 (1985).

- [26] G. H. Vineyard, *Frequency factors and isotope effects in solid state rate processes*, Journal of Physics and Chemistry of Solids **3**, 121 (1957).
- [27] I. M. Ciobica, A. W. Kleyn, and R. A. Van Santen, *Adsorption and coadsorption of CO and H on ruthenium surfaces*, Journal of Physical Chemistry B **107**, 164 (2003).
- [28] I. Del Rosal, L. Truflandier, R. Poteau, and I. C. Gerber, *A density functional theory study of spectroscopic and thermodynamic properties of surfacic hydrides on Ru (0001) model surface: The influence of the coordination modes and the coverage*, Journal of Physical Chemistry C **115**, 2169 (2011).
- [29] Y. Lu and P. Zhang, *First-principles study of temperature-dependent diffusion coefficients: Hydrogen, deuterium, and tritium in  $\alpha$ -Ti*, Journal of Applied Physics **113**, 193502 (2013).

# 5

## TIN DEPOSITION ON RUTHENIUM AND ITS INFLUENCE ON HYDROGEN PERMEATION

*An atomistic description of tin deposition on ruthenium and its effect on blistering damage is of great interest in extreme ultraviolet (EUV) lithography. In EUV machines, tin debris from the EUV-emitting tin plasma may be deposited on the mirrors in the optical path. Tin facilitates the formation of hydrogen-filled blisters under the ruthenium top layer of the multi-layer mirrors. We have used Density Functional Theory (DFT) to show that tin deposition on a clean ruthenium surface exhibits a film-plus-islands (Stranski-Krastanov) growth mode, with the first atomic layer bonding strongly to the substrate. We find that a single Sn layer allows hydrogen to reach the ruthenium surface and subsurface more easily than on clean ruthenium, but hydrogen penetration through the tin film becomes progressively more difficult when more layers are added. The results indicate that hydrogen penetration and blistering occur when only a thin layer of tin is present.<sup>1</sup>*

---

<sup>1</sup>This chapter has been published as: Onwudinanti, C., Brocks, G., Koelman, V., Morgan, T., & Tao, S. (2021). Tin deposition on ruthenium and its influence on blistering in multi-layer mirrors. *Physical Chemistry Chemical Physics*. <https://doi.org/10.1039/D1CP01082D>

## 5.1. INTRODUCTION

The undesirable formation of blisters, pockets of hydrogen gas under the top layer of mirrors in extreme ultraviolet (EUV) lithography machines, is a determining factor in the operational lifetime of these mirrors. Blistering causes a loss of reflectivity, the single most important property of the multi-layer mirrors (MLMs). This presents an obstacle to achieving high-volume manufacturing of next-generation integrated circuits.

The formation of blisters in EUV mirrors is a tale of three elements: ruthenium, hydrogen and tin. Ruthenium is used as the top layer in a stack of 40-60 molybdenum/silicon bilayers, each about 6 to 7 nanometres thick[1, 2]. Hydrogen is present, at near-vacuum pressure, to serve as a protective buffer for the surface and also to etch off impurities such as tin, carbon, and oxygen[3–5]. Tin is the source of EUV light in the machines, as tin droplets are excited by a laser to generate EUV-emitting tin plasma. Tin debris can then be deposited on other surfaces in the machine, including those of the multilayer collector and mirrors in the optical path. Hydrogen comes into contact with the ruthenium cap, and may penetrate the surface, diffuse through the bulk to the interface(s) of the multi-layer structure, and recombine to form pockets of H<sub>2</sub> gas. When these pockets reach a critical pressure, the layers separate, resulting in blisters and loss of reflectivity. [6, 7].

Our study of tin deposition on ruthenium and its effect on blistering is motivated by the observation that blistering proceeds more rapidly in the presence of tin debris. In previous publications, we examined the effect of tin on hydrogen penetration into ruthenium, and the mechanism via which hydrogen becomes trapped under the normally near-impermeable ruthenium[8, 9]. We found that the proximity of tin to a hydrogen atom on the surface resulted in a lowering of the energy barrier to its penetration into the subsurface; furthermore, we showed that the saturation of the surface with hydrogen and tin inhibited diffusion of hydrogen out of the ruthenium layer from the top surface. These computational studies of the effect of tin have so far been limited to the interactions of ruthenium and hydrogen with dispersed tin atoms and tin hydrides on the exposed ruthenium surface.

Tin has long been used as a protective coating for metals, and thin films have been reported to hinder hydrogen permeation into iron[10]. Tin deposition on ruthenium has been studied in experiment, exploring the effect of deposition temperature on the structure of deposited tin[11], and its surface alloying with lead[12]; *ab initio* studies have been reported for sub-monolayer tin films on ruthenium[13]. For the EUV application the interaction with atomic hydrogen is paramount, and this has been a topic of intense study for the past decade. These experiments focus primarily on the efficiency of Sn removal. Studies of tin etching from representative MLM samples show that both the rate of Sn removal and blistering of samples depend strongly on the nature of the top layer and the surface morphology of the tin layer; in these experiments, tin layers of up to 20 nm were etched from diverse materials[14–16]. To the best of our knowledge, no study of the atomistic interaction of hydrogen with multi-layer tin on ruthenium has been re-

ported. Our aim, therefore, is to examine how the presence of multiple layers affects the likelihood of hydrogen permeation and blistering.

In this study, we look at the energetics of tin growth on a ruthenium surface, and examine the paths of hydrogen through the tin on the ruthenium surface. Our calculations show that tin binds strongly to the clean ruthenium surface, with the energies indicating a film-plus-islands growth mode (the so-called Stranski-Krastanov mode). The monolayer of tin changes the energy landscape in such a manner that when the Sn/Ru surface is exposed to atomic hydrogen, the gas passes into the ruthenium subsurface relatively easily, with multiple layers of tin becoming progressively less permeable.

The article is structured thus: we report first the calculated structure for one densely-packed layer of tin on clean and hydrogen covered ruthenium surfaces. Thereafter we study the evolution of the structures and energies of layers of tin. This is followed by a look at the interaction of hydrogen with the tin-on-ruthenium system. Finally we perform transition state calculations for hydrogen diffusion through the tin overlayer(s), and discuss the implications of the computed energies for blistering in EUV mirrors.

## 5.2. COMPUTATIONAL METHODS

The calculations in this article employ DFT as implemented in the Vienna *ab initio* Simulation Package (VASP) [17–19]. We employed the generalized gradient approach proposed by Perdew, Burke, and Ernzerhof (PBE) [20], with the following convergence criteria: a kinetic energy cutoff of 400 eV, a residual force criterion between  $1 \times 10^{-2}$  eV/Å and  $5 \times 10^{-2}$  eV/Å<sup>-1</sup>, with  $1 \times 10^{-5}$  eV as the energy convergence criterion. Calculations for reference energies of bulk Sn and Ru were performed in a 2x2x2 unit cell, while slab calculations were done with a rectangular unit cell, as described in Section 5.3.1. Bulk calculations were done with a  $(9 \times 9 \times 9)$   $\Gamma$ -centred  $k$ -point grid, while slab calculations were performed with a  $(9 \times 9 \times 1)$   $\Gamma$ -centred  $k$ -point grid with at least the top 2 layers of the slabs allowed to relax in the optimization. Transition state calculations were carried out using the Climbing Image Nudged Elastic Band (CINEB) algorithm [21], with a force criterion between  $1 \times 10^{-2}$  and  $3 \times 10^{-2}$  eV/Å and one (1) to seven (7) intermediate geometries for the transition state search.

The calculated lattice parameters for hexagonal close-packed (hcp) ruthenium are  $a = 2.71$  Å and  $c/a = 1.585$ , which are in good agreement with experimental results, 2.71 Å and 1.58, respectively [22]. The Ru(0001) surface is modelled as a slab of seven (7) layers using a  $(\sqrt{3} \times 3)$  rectangular unit cell, with approximately 15 Å of vacuum between the periodic images in the  $z$ -direction.

The energy of adsorption is computed per the definition

$$E_{ads} = \frac{1}{n} (E_{nA,slab} - E_{slab} - nE_{Aref}), \quad (5.1)$$

where  $E_{nA,slab}$ ,  $E_{slab}$ , and  $E_{Aref}$  stand respectively for the total energies of the slab with  $n$  adsorbed atoms of element A, the slab without the adsorbed atom(s), and the refer-

ence energy of the adsorbed atom(s). This reference energy is half the energy of the  $H_2$  molecule for hydrogen, and the energy of one  $\beta$ -tin atom for adsorbed tin.

Due to the very low mass of the hydrogen atom, its diffusion is, in general, influenced by zero-point energy (ZPE). Therefore the energy barriers reported in the subsequent chapters include ZPE corrections. The ZPE is calculated by the relation

$$ZPE = \frac{1}{2} \sum_i h\nu_i, \quad (5.2)$$

where  $\nu_i$  is a real normal mode frequency. For example, the zero point energy for a hydrogen molecule ( $H_2$ ) calculated thus is 0.27 eV (0.135 eV per H atom), corresponding to a vibrational mode of  $4354 \text{ cm}^{-1}$ , in good agreement with the experimentally-determined value of  $4401 \text{ cm}^{-1}$  [23].

## 5.3. RESULTS AND DISCUSSION

### 5.3.1. STRUCTURE AND ENERGIES OF SN ON CLEAN RU

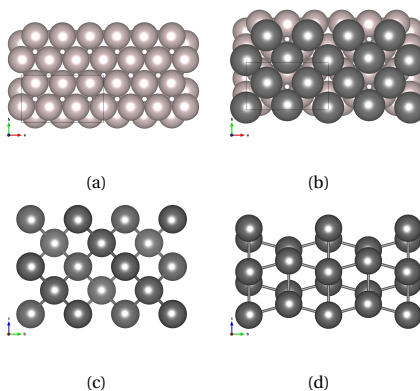


Figure 5.1: (a) Top view of Ru(0001) slab (black rectangle shows unit cell); (b) structure of  $\frac{1}{3}$ ML Sn on Ru; (c)  $\alpha$ -Sn crystal; (d)  $\beta$ -Sn. Dark spheres represent Sn, light spheres Ru.

Tin deposition on the Ru(0001) surface has been modelled in a series of DFT calculations. As the ruthenium and tin differ significantly both in crystal structure and atomic radius, an appropriate unit cell for the calculation must be chosen to minimise the mismatch. The rectangular unit cell (shown in Figure 5.1a) successfully accommodates the structure of the tin overlayer, which is not necessarily hexagonal (see Appendix for a comparison of Sn slabs in the rectangular unit cell and  $\beta$ -Sn lattice). The chosen reference state of tin is  $\beta$ -Sn shown in Figure 5.1d, the so-called white tin, which is stable at room temperature, close to the operating conditions of EUV machines. Although  $\alpha$ -Sn is most stable at low temperatures, the choice of reference state has no consequence for the calculations or conclusions.

We have carried out geometry optimisations for varying numbers of complete layers of Sn on the Ru surface. We first determine the structure of the single atomic layer of Sn, and subsequently find the lowest-energy configurations for each newly-added layer. We report the adsorption energies for the successive layers, and discuss the implications for the growth of tin on ruthenium.

### 1 LAYER

Due to the large size of the tin atom, the most dense packing of a tin layer on the Ru surface has 2 Sn atoms per 3 Ru atoms (giving 4 Sn atoms in the unit cell), which we designate  $\frac{2}{3}$ ML, shown in Figure 5.1b. To find the structure of this layer, we performed first a geometrical optimisation of a 7-layer Ru(0001) slab, then a further optimisation of the resulting slab with the Sn atoms on the surface, with all atoms permitted to relax. The result of this calculation, repeated with various starting positions of the Sn atoms, is the structure of the single Sn layer, illustrated in Figure 5.1b.

This coincides with the  $(\sqrt{3} \times \sqrt{3})$ -rect structure reported from experiment[11, 12] and first principles[13]. The atoms in the first layer show a large negative adsorption energy of  $-1.19$  eV, per Equation 5.1, with the energy of one  $\beta$ -Sn atom as the reference. For projected density of states of the Sn/Ru interface, see Appendix. The strong bond between the Sn and Ru atoms is attested by the difficulty of etching Sn completely from Ru[14].

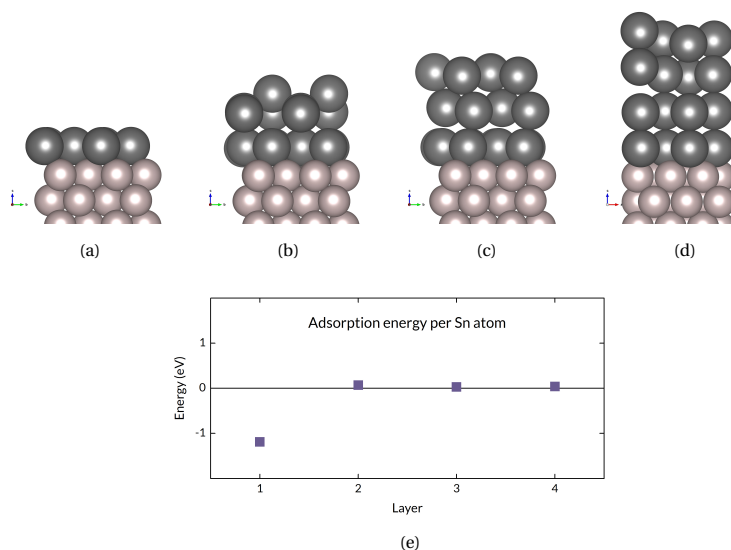


Figure 5.2: (a)-(d) Structures of Sn on Ru, with 1-4 layers (side view; dark spheres represent Sn, light spheres Ru), and (e) average energy of adsorption per atom in Sn layers, relative to  $\beta$ -tin (0 eV). Note that the adsorption energies are averaged over atoms in each successive layer from (a) to (d), thereby showing the strength of adsorption to the layer immediately beneath.

## 2 LAYERS

Several calculations were performed to ascertain the preferred structure of 2 layers of Sn on Ru. Varying configurations of 4 additional Sn atoms were placed on the single-layer structure of Figure 5.1b, and the resulting systems were allowed to relax in a standard geometry optimisation. The lowest-energy arrangement of 2 layers of Sn on Ru has the structure shown in Figure 5.2. A second energy minimum was found, in which the second tin layer is identical to the first. The total energy of this structure is only 0.04 eV higher than that of the first. Two key observations can be made: (1) for the lowest-energy structure, the arrangement of the second layer of tin departs significantly from that of the flat underlying layer, forming a staggered, undulating layer; and (2) the energy of the Sn atoms is markedly higher than those of the first layer, resulting in an adsorption energy that is slightly positive: +0.07 eV relative to bulk  $\beta$ -Sn. This is a sharp departure from the strongly negative adsorption energy of  $-1.19$  eV for atoms in the first layer. This implies that while the first layer adsorbs strongly to the underlying Ru surface, the second layer does not bind to the Sn layer beneath, and remains close in energy to the bulk state. The observed slightly positive adsorption energy for the second layer of Sn atoms indicates that there is no tendency for tin debris on a ruthenium surface to spread into a second smooth layer.

## 3 & 4 LAYERS

Both our calculations and previous experiments suggest a tendency of tin towards three-dimensional clustering. This means that there will be regions with multiple layers of tin, even when relatively small amounts of tin are deposited on a ruthenium film. We model these regions by adding multiple tin layers in our periodic supercell.

Calculations for a third layer of tin shows that it also forms an uneven sheet of atoms. This behavior extends to 4 layers, the most we have examined. Here too, we find that the energy per atom is slightly higher than the  $\beta$ -Sn reference. For both the 3rd and 4th layers, the adsorption energy is slightly positive, 0.03 eV. The observed minimum energy structures and corresponding energies (Figure 5.2) indicate that after the layer of tin in direct contact with the ruthenium surface, subsequent layers adopt a structure that is more like that of  $\beta$ -Sn. One peculiarity is notable: in the 4-layer structure shown, the two bottom layers are identical and flat, with the top two layers taking the aforementioned corrugated form. Considering that the 2-layer structure with identical layers was only 0.04 eV higher than the lowest-energy arrangement, the presence of the 3rd and 4th layers appears to have shifted the energies to favour such a structure.

## SN GROWTH ON RU

The energies and structures reported in the preceding sections prompt a number of conclusions. Sn binds strongly to the Ru surface, with a strongly negative adsorption energy, and with a smooth layer; therefore it confirms the conjecture by Paffet et al[11] that the Sn-Ru metal-metal bonding enthalpy is greater than that of Sn-Sn bonding. This strong bonding is entirely consistent with the finding that Sn cannot be etched completely from

a Ru substrate. However, subsequent Sn layers do not bind strongly to the Sn underneath. Furthermore, the atoms in the second and higher number of layer(s) are arranged in a distinctly different way (resembling the bulk Sn) from the first layer.

Taken together, these findings indicate that the deposition of tin on ruthenium should follow the so-called Stranski-Krastanov growth mode. Here we observe this mode of epitaxial growth via the formation of a single layer of complete tin film on the substrate, after which three-dimensional islands develop. We see in Figure 5.2e that there is a strong thermodynamic advantage to the formation of a single flat layer of tin. This advantage is absent for a second layer and subsequent layers, since a tin atom in the bulk, and therefore in 3D islands, is at approximately the same energy level.

### 5.3.2. SN ON H/RU

The main motivation for this study is the blistering of multi-layer mirrors observed when tin debris from the EUV source plasma lands on the ruthenium surface. Hydrogen plasma is used to etch Sn contamination from the surface of the optics. As hydrogen may be present before tin, we consider next the situation when the ruthenium surface is exposed to hydrogen prior to tin exposure.

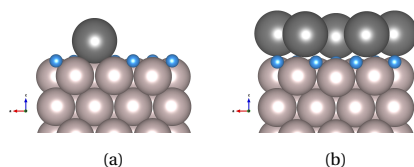


Figure 5.3: Sn on H/Ru(0001); (a) lone Sn atom (b) dense-packed layer of Sn. Dark grey spheres represent Sn, light grey spheres Ru, bright blue spheres H.

Hydrogen adsorbs and dissociates readily on the Ru(0001) surface[8, 24]. All adsorption sites for H atoms have negative adsorption energies, with a preference for the sites with 3-fold coordination, commonly referred to as the *fcc* and *hcp* sites. These have adsorption energies of  $-0.63$  and  $-0.57$  eV respectively. With H atoms exhibiting such affinity for the Ru surface, it is to be expected that this will affect the Sn-Ru interaction. This indeed proves to be the case. A single Sn atom on the H-covered Ru (at a concentration of 1 H atom per Ru atom) has a positive ( $+0.21$  eV) adsorption energy, with  $\beta$ -Sn as the reference (Figure 5.3). For a full Sn layer, the adsorption energy per atom is 0.13 eV. We have also performed a comparison of diffusion barriers calculated with the CINEB algorithm, and it shows a large difference in mobility. The potential energy surface for Sn adsorbed on Ru is quite flat[8, 13], and the energy barrier for diffusion from one 3-fold site to the next is at most 0.13 eV on a clean Ru surface. This changes to 1.0 eV for Sn on an H-covered surface.

Tin is therefore unlikely to spread and form a single-atom wetting layer on the hydrogen-passivated surface, and should remain in 3D islands instead. This appears to explain the

findings reported by Faradzhev and Sidorkin[25], who reported a Volmer-Weber mechanism of Sn growth on Ru.

### 5.3.3. H ON SN/RU

In previous studies, we examined the effect of adsorbed tin atoms and tin hydrides on the interaction of hydrogen and ruthenium, and found a considerable effect on the penetration of hydrogen into ruthenium. We go further here and calculate the energies for hydrogen on, in and under several layers of tin on the ruthenium. We consider also the implications of the computed energies for a multi-layer mirror exposed to atomic hydrogen, as found in the EUV-induced plasma in the lithographic machines of interest.

#### 1 LAYER

The adsorption of hydrogen on the tin overlayer is not energetically favourable. A hydrogen atom adsorbed directly on an Sn atom — the *top* site — has an adsorption energy of +0.7 eV. This can be interpreted to mean that dissociative adsorption of H<sub>2</sub> comes at a considerable energy cost, and also that hydrogen atoms on the Sn surface would tend to recombine and desorb from the unfavourable surface.

With only 2 Sn per 3 Ru atoms fitting into the densest packing of the deposited overlayer, the result is a porous Sn layer through which the small H atom can access the Ru surface. Figure 5.4 shows the computed structures. Although the number of available sites is reduced, H can adsorb at the favoured sites with 3-fold coordination, the *fcc* and *hcp* sites of the Ru(0001) surface. The preference for these sites is unchanged relative to pristine Ru, with one key difference: the adsorption energy relative to the H<sub>2</sub> is no longer negative (*hcp*: -0.58 eV; *fcc*: -0.63 eV), but positive (*hcp*: +0.17 eV; *fcc*: +0.18 eV).

Although these positive energies would indicate that dissociative adsorption of H<sub>2</sub> on Ru(0001) is hindered by the Sn layer, atomic hydrogen would favour the Ru surface. The hydrogen radicals in an (EUV-induced) plasma are at a much higher energy level than H in an H<sub>2</sub> molecule (2.27 eV higher), which means that the Sn/Ru surface is energetically favourable, and is rapidly populated when atomic hydrogen is supplied.

#### 2 LAYERS

The presence of a second layer of tin hardly changes the energy landscape of a hydrogen atom in the system. As in the case with a single layer, the lowest-energy state is the H<sub>2</sub> molecule. Adsorption of H on the Sn film remains unfavourable, with a positive adsorption energy for H on the *top* site shown in Figure 5.4d.

An additional tin layer presents the possibility of an interstitial state, as an H atom can occupy the subsurface sites between the atoms of the first and second layers of the deposited tin (Figure 5.4e). However, interstitial hydrogen in the tin is a relatively high-energy, unfavourable state, +0.7 eV above the H<sub>2</sub> reference. This is to be expected, as the solubility of hydrogen in tin is not high. This state is therefore unlikely to be occupied at any considerable concentration when the Ru/Sn is exposed to molecular hydrogen.

Here too the Ru surface sites with 3-fold coordination are the lowest in energy for an H atom. However, the adsorption energy becomes yet more positive, now +0.28 eV for *hcp*, +0.31 eV for *fcc* (Figure 5.4f).

The case with atomic hydrogen is of course different, with the hydrogen atom starting at a much higher energy level. All of the afore-mentioned sites on the surface of and between the layers of tin are lower in energy than a hydrogen radical, and the amount of hydrogen in those states would be greater than under only H<sub>2</sub>.

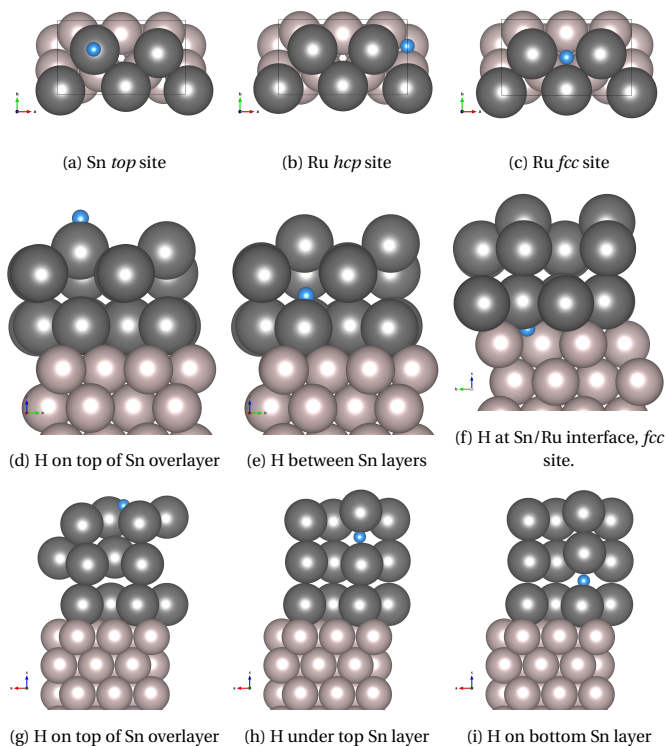


Figure 5.4: (a)-(c) H on  $\frac{1}{4}$ ML Sn/Ru, top view; (d)-(f) H on Sn/Ru  $\frac{1}{4}$ ML, side view; (g)-(i) H on 2MLSn/Ru, side view. Dark grey spheres represent Sn, light spheres Ru, bright blue spheres H.

### 3 LAYERS

At 3 layers of tin, a general picture emerges for the H-Sn-Ru interactions at the surface of the multi-layer mirror. H adsorption on the Sn film is unlikely, due to the positive adsorption energy, +0.6 eV adsorption energy for the hollow site. Atomic hydrogen should result in increased adsorption of H on the surface, but with the Sn overlayer present, hydrogen favours the molecular state more than the surface state and the interstitial states, both in the region directly under the surface Sn atoms and deeper.

### 5.3.4. THE PROGRESS OF H THROUGH SN AND RU

Using the CINEB algorithm, we performed transition state searches for hydrogen diffuse pathways between the minima described in the preceding sections. For overall comparison, we consider three key structures: a clean Ru(0001) surface, Ru +  $\frac{2}{3}$  ML of Sn (1 layer), and Ru + 2ML of Sn (3 layers). These are summarised in Figure 5.5.

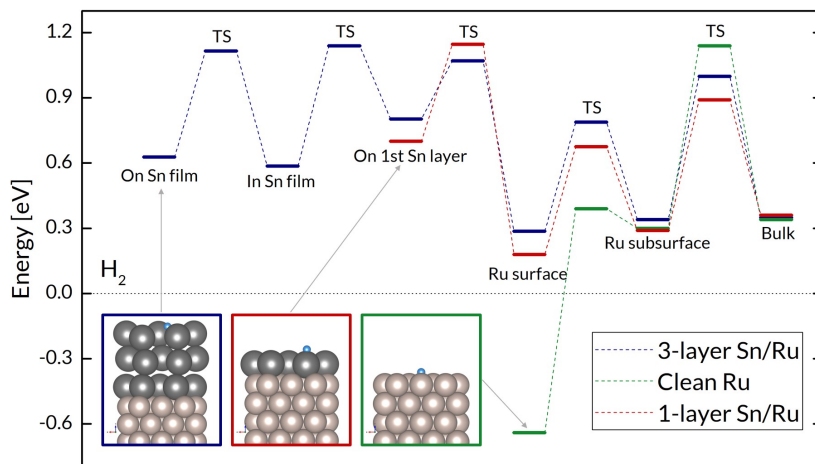


Figure 5.5: Energy profile of H on and in Sn on Ru with no Sn (green), 1 layer of Sn (red), and 3 layers of Sn (blue). The figures in boxes of corresponding colour show the starting point (leftmost marker) of the evaluated path of hydrogen from the surface to the ruthenium bulk.

With no tin on the Ru surface, the energies of hydrogen indicate a strong preference for the adsorbed, dissociated state. The negative adsorption energy ( $-0.63$  eV relative to the  $H_2$  molecule) puts this state far below all the other energy minima encountered in our calculations for H, Sn, and Ru. Moreover, the energy barrier between the adsorbed state and the subsurface interstitial state is  $1.06$  eV. This indicates a low likelihood of hydrogen permeation through the clean ruthenium. Also Ru has a  $+0.34$  eV energy of formation for hydride, where hydrogen locates at interstitial site. By all indications, hydrogen concentration in the ruthenium bulk, and at the interface underneath the ruthenium, should remain quite low.

The presence of a Sn overlayer causes two significant changes in the energy landscape. First, the Ru surface site (underneath Sn) remains the lowest in energy, although, at  $+0.18$  eV above the molecular state, it is not as favourable for hydrogen occupation as a clean Ru surface. The second change is in the energy barrier for hydrogen penetration, which falls to  $0.5$  eV. This halving of the energy barrier for hydrogen penetration is accompanied by an increase in the barrier of the reverse process. Thus, with the Sn present, hydrogen is more likely to go from the Ru surface to the subsurface, and less likely to go from the subsurface to the surface.

The progress of hydrogen through 3 layers of tin entails passing through several high-

energy states. First, the adsorption on the top layer is energetically unfavourable, lying 0.6 eV above the  $H_2$  molecular state. Then follow the interstitial states within the film, as well as the transition states between them, which are all above the reference state. The energy barriers in the path from the Sn surface to the Ru surface are, respectively in eV: 0.50, 0.56, 0.33. Compared to the case with only 1 relatively porous layer of tin, the likelihood of an H atom to travel through to the ruthenium surface is much reduced.

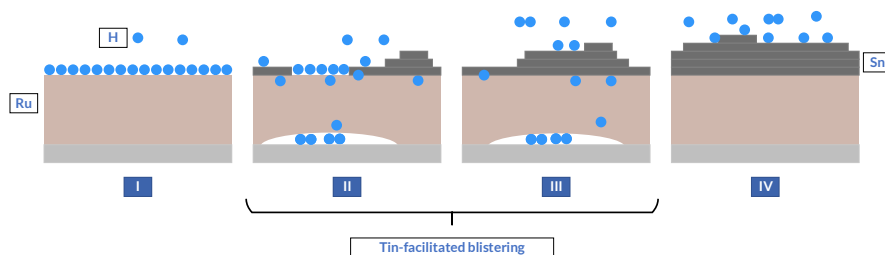


Figure 5.6: Four states of tin deposition on ruthenium and their effect on the likelihood of tin-facilitated blistering.

### 5.3.5. ATOMIC HYDROGEN AND BLISTERING

The main motivation for this study is the blistering of multi-layer mirrors observed when tin debris from the EUV source is deposited on the ruthenium surface. Hydrogen is used to etch Sn contamination from the surface of the optics, and the removal of contamination from the mirror surface with plasma is the subject of numerous publications. The energies reported and discussed in the preceding section are calculated relative to molecular hydrogen, the reference state to which H from the Sn/Ru returns via recombination and desorption. However, EUV-induced plasma is present in the lithographic machines, with the result that atomic hydrogen can make contact with the ruthenium-capped mirrors.

As the H radicals are at a higher energy level, all the states in Figure 5.4 are more accessible. Therefore, with low enough Sn coverage and exposure to hydrogen plasma, a large number of H atoms will reach the Ru surface, and thereafter the subsurface. In view of the inhibition of out-diffusion by adsorbates, the right amount of tin will lead to blistering.

The Stranski-Krastanov growth mode implies that further tin deposition onto the first Sn wetting layer will leave part of the Sn overlayer uncovered up to a certain point, after which continued deposition of tin will fill in the “valleys”. Working in the opposite direction, etching of Sn layers with H radicals will likely proceed without blistering, until the last, tightly-bound wetting layer is exposed, at which point H entry into Ru is enabled. We can therefore delineate four (4) different states for the Ru/Sn/H system, with differ-

ing probabilities of significant H penetration, and the implications for blistering in each (see Figure 5.6):

- I pristine Ru – surface is saturated with dissociated H atoms, no blistering;
- II incomplete Sn overlayer – H atoms penetrate Ru through the porous Sn layer and at the edges, in proximity to Sn atoms, blistering;
- III complete Sn wetting layer with 3D mounds – H atoms penetrate Ru through the porous Sn layer, blistering;
- IV multiple Sn layers covering Ru surface – Sn layers provide additional obstacles to H diffusion, no blistering.

## 5.4. CONCLUSION

We have carried out a computational study of the deposition of tin on the ruthenium surface, through calculation of the structures and energies of various amounts of tin, from one layer to several. The calculations have shown that tin will spread to form a single-layer film on the ruthenium, and thereafter grow by forming three-dimensional islands. We show also that tin does not adsorb strongly on a hydrogen-covered ruthenium surface. We have performed transition state calculations for the hydrogen diffusion paths through a tin film consisting from one to several layers to the ruthenium surface and subsurface. The results show that multiple layers of Sn will obstruct the hydrogen atoms, whereas a single or incomplete layer will allow and facilitate hydrogen permeation.

## REFERENCES

- [1] Y. B. He, A. Goriachko, C. Korte, A. Farkas, G. Mellau, P. Dudin, L. Gregoratti, A. Barinov, M. Kiskinova, A. Stierle, N. Kasper, S. Bajt, and H. Over, *Oxidation and reduction of ultrathin nanocrystalline Ru films on silicon: Model system for Ru-capped extreme ultraviolet lithography optics*, *Journal of Physical Chemistry C* **111**, 10988 (2007).
- [2] S. Bajt, H. N. Chapman, N. Nguyen, J. B. Alameda, J. C. Robinson, M. E. Malinowski, E. Gullikson, A. Aquila, C. Tarrío, and S. Grantham, *Design and performance of capping layers for EUV multilayer mirrors*, *Proc. SPIE* **5037**, 236 (2003).
- [3] M. M. J. W. van Herpen, D. J. W. Klunder, W. A. Soer, R. Moors, and V. Banine, *Sn etching with hydrogen radicals to clean EUV optics*, *Chemical Physics Letters* **484**, 197 (2010).
- [4] D. T. Elg, G. A. Panici, S. N. Srivastava, and D. N. Ruzic, *Collector optic cleaning by in-situ hydrogen plasma*, *Extreme Ultraviolet (EUV) Lithography VI* **9422**, 94222H (2015).
- [5] D. Qerimi, G. Panici, A. Jain, D. Jacobson, and D. N. Ruzic, *Study of a linear surface wave plasma source for tin removal in an extreme ultraviolet source*, *Journal of Vacuum Science & Technology B* **38**, 052601 (2020).
- [6] A. S. Kuznetsov, R. W. E. van de Kruijs, M. A. Gleeson, K. Schmid, and F. Bijkerk, *Hydrogen interaction with EUVL-relevant optical materials*, *Journal of Surface Investigation. X-ray, Synchrotron and Neutron Techniques* **4**, 563 (2010).
- [7] A. S. Kuznetsov, M. A. Gleeson, and F. Bijkerk, *Temperature dependencies of hydrogen-induced blistering of thin film multilayers*, *Journal of Applied Physics* **115**, 173510 (2014).
- [8] C. Onwudinanti, I. Tranca, T. Morgan, and S. Tao, *Tin, The Enabler—Hydrogen Diffusion into Ruthenium*, *Nanomaterials* **9**, 129 (2019).
- [9] C. Onwudinanti, G. Brocks, V. Koelman, T. Morgan, and S. Tao, *Hydrogen diffusion out of ruthenium—an ab initio study of the role of adsorbates*, *Physical Chemistry Chemical Physics* **22**, 7935 (2020).
- [10] B. N. Popov, J.-W. Lee, and M. B. Djukic, *Hydrogen Permeation and Hydrogen-Induced Cracking*, in *Handbook of Environmental Degradation of Materials* (Elsevier, 2018) third edit ed., pp. 133–162.
- [11] M. T. Paffett, A. D. Logan, and T. N. Taylor, *Tin deposition on ruthenium (001): a multitechnique surface science study*, *The Journal of Physical Chemistry* **97**, 690 (1993).

- [12] J. Yuhara, Y. Ishikawa, and T. Matsui, *Two-dimensional alloy of immiscible Pb and Sn atoms on Ru(0001)*, *Surface Science* **616**, 131 (2013).
- [13] R. Topolnicki and R. Kucharczyk, *Structural and electronic properties of submonolayer-thick Sn films on Ru(0001)*, *Applied Surface Science* **329**, 376 (2015).
- [14] M. Pachecka, J. M. Sturm, R. W. E. van de Kruijs, C. J. Lee, and F. Bijkerk, *Electronegativity-dependent tin etching from thin films*, *AIP Advances* **6**, 075222 (2016).
- [15] D. T. Elg, J. R. Sporre, G. A. Panici, S. N. Srivastava, and D. N. Ruzic, *In situ collector cleaning and extreme ultraviolet reflectivity restoration by hydrogen plasma for extreme ultraviolet sources*, *Journal of Vacuum Science & Technology A: Vacuum, Surfaces, and Films* **34**, 021305 (2016).
- [16] D. T. Elg, G. A. Panici, S. N. Srivastava, and D. N. Ruzic, *Study of Sn removal processes for in-situ collector cleaning*, *Extreme Ultraviolet (EUV) Lithography VII* **9776**, 97760M (2016).
- [17] G. Kresse and J. Hafner, *Ab initio molecular-dynamics simulation of the liquid-metalamorphous- semiconductor transition in germanium*, *Physical Review B* **49**, 14251 (1994).
- [18] G. Kresse and J. Furthmüller, *Efficiency of ab-initio total energy calculations for metals and semiconductors using a plane-wave basis set*, *Computational Materials Science* **6**, 15 (1996).
- [19] D. Joubert, *From ultrasoft pseudopotentials to the projector augmented-wave method*, *Physical Review B - Condensed Matter and Materials Physics* **59**, 1758 (1999).
- [20] J. D. Perdew, K. Burke, and M. Ernzerhof, *Generalized Gradient Approximation Made Simple*, *Physical Review Letters* **77**, 3865 (1996).
- [21] G. Henkelman, B. P. Uberuaga, and H. Jónsson, *Climbing image nudged elastic band method for finding saddle points and minimum energy paths*, *Journal of Chemical Physics* **113**, 9901 (2000).
- [22] H. King, *Crystal structures and lattice parameters of allotropes of the elements*, in *CRC Handbook of Chemistry and Physics* (CRC Press, 2012) pp. 15–18.
- [23] K. K. Irikura, *Experimental Vibrational Zero-Point Energies: Diatomic Molecules*, *Journal of Physical and Chemical Reference Data* **36**, 389 (2007).

- [24] I. Del Rosal, L. Truflandier, R. Poteau, and I. C. Gerber, *A density functional theory study of spectroscopic and thermodynamic properties of surfacic hydrides on Ru (0001) model surface: The influence of the coordination modes and the coverage*, *Journal of Physical Chemistry C* **115**, 2169 (2011).
- [25] N. Faradzhev and V. Sidorkin, *Hydrogen mediated transport of Sn to Ru film surface*, *Journal of Vacuum Science & Technology A: Vacuum, Surfaces, and Films* **27**, 306 (2009).

## APPENDIX

### PROJECTED DENSITY OF STATES (PDOS)

Figure 5.A2 shows the PDOS for the surface atoms on the Ru(0001) slab with and without Sn and H. The difference between the top (Ru slab) panel and the second ( $\frac{2}{3}$  ML Sn on Ru) suggests metallic bonding. Sn has  $5s^2p^2$  occupation. There is little change from the second ( $\frac{2}{3}$  ML Sn on Ru) panel to the third (H &  $\frac{2}{3}$  ML Sn on Ru). The presence of the H layer in the fourth ( $\frac{2}{3}$  ML Sn & 1ML H on Ru) panel has resulted in Ru d-H s bonding states around  $-7.0$  eV.

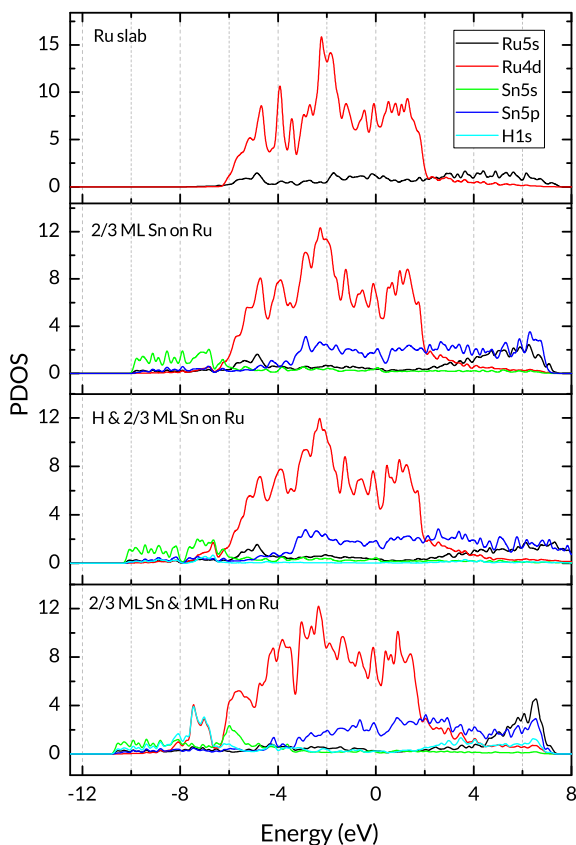


Figure 5.A1: PDOS for (a) surface Ru atoms in Ru slab, (b) surface Ru atoms and  $\frac{2}{3}$  ML Sn on Ru, (c) surface Ru atoms,  $\frac{2}{3}$  ML Sn and H, and (d) surface Ru atoms, 1 ML H (6 H atoms) and  $\frac{2}{3}$  ML Sn.

## FREE SN SLABS

The 4-layer Sn overlayer slab was put through geometry optimisation without the Ru substrate. This free Sn slab has an energy of  $-3.67$  eV/atom, against  $-3.68$  eV/atom for a  $\beta$ -Sn(001) slab. The energy difference is small, which indicates minimal strain.

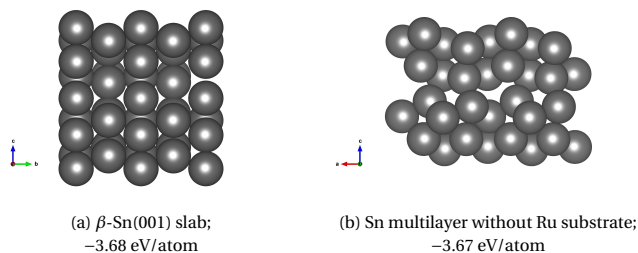


Figure 5.A2: Sn slabs after geometry optimisation.

## MINIMUM ENERGY PATHS FOR TRANSITION STATE CALCULATIONS

The transition states are found with CINEB calculations using 5-7 images. The energies are plotted without zero-point energy adjustments.

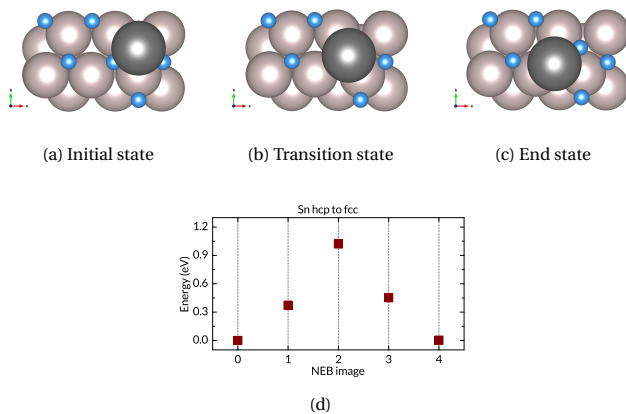


Figure 5.A3: (a) Minimum energy path of Sn atom from *hcp* site to *fcc* site on H/Ru(0001); (b)-(d) NEB images 0, 2, and 4 respectively.

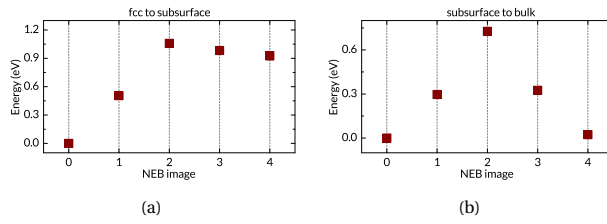


Figure 5.A4: Minimum energy paths for H diffusion on clean Ru

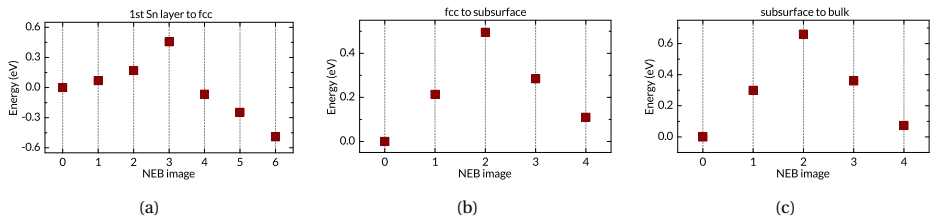
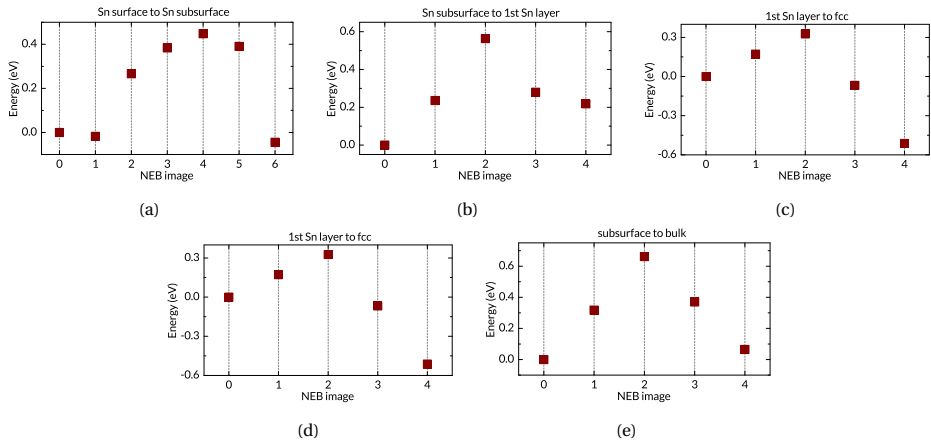
Figure 5.A5: Minimum energy paths for H diffusion on  $\frac{1}{3}$  ML Sn on Ru

Figure 5.A6: Minimum energy paths for H diffusion on 2 ML Sn on Ru

# 6

## A MOLECULAR DYNAMICS STUDY OF HYDROGEN DIFFUSION IN RUTHENIUM

*Ruthenium thin films serve as a protective cap for multi-layer mirrors exposed to atomic hydrogen. Molecular dynamics simulations have been performed of hydrogen atom diffusion through ruthenium, to study the effect of grain boundaries on the mechanism and rates of permeation. In addition to H diffusion through a perfect crystal, two different grain boundaries were studied:  $\Sigma 7$  tilt and  $\Sigma 7$  twist grain boundaries. A ReaxFF force field was parametrised for the Ru-H system which reproduces grain boundary formation energies and hydrogen trapping energies from quantum-mechanical calculations. Dynamic simulations show anisotropic diffusion in hcp ruthenium, favouring transport in the c direction of the lattice. The tilt and twist grain boundaries host energetically favourable sites for hydrogen atoms, and both types of grain boundary were shown to block H transport across their planes, with the result being accumulation of hydrogen at the grain boundaries. Diffusion within the plane of each grain boundary was shown to be slightly more rapid, with a number of trapping sites present in each. However, at room temperature and low concentration, the GBs likely retard H diffusion. Because of the strong effect of the grain boundaries on the dynamics of hydrogen diffusion, the morphology of ruthenium thin films will have the deciding influence on the rate of hydrogen permeation.*

## 6.1. INTRODUCTION

The effects of hydrogen inclusion within various materials are often detrimental to their desirable properties. Hydrogen-induced damage[1] poses a problem in many diverse fields, including hydrogen (H) transport and storage[2, 3], nuclear fusion[4], and extreme ultraviolet (EUV) lithography[5]. The latter application employs multi-layer reflective optics which are susceptible to hydrogen-induced damage. Ruthenium serves as a capping layer in these mirrors, therefore the transport of H through the metal is an important factor in determining the operational lifetime of the optical elements.

H diffusion in metals typically occurs via hopping of H atoms through the interstitial sites in the metal lattice. A central feature of H diffusion and hydrogen-induced damage is the interaction of the H atoms with defects, such as vacancies, voids, phase boundaries and grain boundaries (GBs) in the crystal lattice[6]. These defects provide microstructural trap sites for H – sites at which the energy of inclusion of the solute atom is significantly lower, and residence time longer, than at the usual interstitial sites. The number and nature of these traps is therefore a determining factor in the overall diffusion of the hydrogen in the films. GBs usually host such traps, and have been shown to affect the solubility and diffusion of H in metals. For example, in nickel GBs are reported to retard diffusion[7]. In aluminium, GBs have been shown to enhance or suppress H diffusion depending on the size of the grains[8], and to block H diffusion across the boundary plane while enhancing diffusion along it[9]. In hydrogen storage, the rate of hydrogenation of magnesium was shown to increase with grain size[10].

Although the interaction of H with ruthenium (Ru) surfaces is well-represented in the literature[11–13] in the field of catalysis, research on H in the Ru bulk is sparse, and limited to the H solubility in Ru and the thermodynamics of hydride formation[14, 15]. The diffusion of H in Ru has received little attention, in contrast to other metals[6]. The solubility of H in Ru is quite low, which makes experimental study of H diffusion through Ru technically challenging. One indirect measurement of the diffusion rate of H through Ru thin films has been reported[16], using optical changes in an yttrium hydride substrate; notably, the diffusion model in that publication assumes GB transport to be dominant.

Molecular dynamics (MD) provide a means to study H diffusion in Ru. The trajectories of all the atoms in the system are determined per Newton's equation of motion, so that the evolution of the system in time can be tracked with atomistic resolution. This allows many properties and phenomena to be studied which are inaccessible to experimental techniques. MD is especially suited to the determination of transport properties, such as diffusion rates. It also allows detailed visualisations of diffusion dynamics, thereby rendering useful insights into diffusion mechanisms. In practice, the technique is limited only by computational resources and, most importantly, the availability and accuracy of the interatomic potential (force field) used to model the atom interactions. Molecular dynamics has been applied to the study of H diffusion in diverse metals. These studies have included simulations of transport along GBs, and have shed light on the mechanisms of H diffusion. In nickel, grain boundaries have been shown to enhance

diffusion along their plane and to hinder diffusion across it[17]. In  $\alpha$ -iron, GBs have been shown to slow diffusion by trapping H atoms[18]. These MD studies illustrate that the GB effects in – enhancement and retardation of diffusion – depend strongly on the specific grain boundary in consideration; in tungsten, certain GBs provide deep traps which hold H atoms in place[19], while others provide paths of low resistance[20].

In earlier work, we calculated the energy barrier to H jumps within the perfect Ru lattice using *ab initio* methods[21]. However, the computational cost of dynamic simulations with quantum-mechanical methods is prohibitive. Moreover, grain boundaries disrupt the periodicity of a crystal lattice, so large unit cells are required to model them accurately. They also come in a large variety of possible configurations, and due to the complexity of the interfaces, the potential energy surface may be quite complicated. Therefore a technique which balances accuracy with reasonable computational load is required for a simulation of these structures. With its dynamic bond breaking and bond formation, the bond-order-based ReaxFF method is well-suited to the study of such features as GBs, and can sample the potential energy surface to an extent which is not accessible to *ab initio* methods.

In this study, we develop a ReaxFF force field for the Ru-H system which reproduces the energies and properties obtained with quantum-mechanical methods. The force field is used for molecular dynamics simulations of the diffusion of H through the intact Ru crystal lattice, and through structures with different grain boundaries. We show the effect of these GBs on the rate and pattern of H transport through Ru, and report diffusion coefficients for the simulated structures. We find that GBs have a profound effect on the H diffusion dynamics in Ru at all simulated temperatures. We discuss the implications of these findings for H transport through Ru bulk and thin films.

## 6.2. COMPUTATIONAL METHODS

The critical component of a molecular dynamics simulation is the force field. This work employs ReaxFF[22–24], a bond-order-based force field method which allows the formation and breaking of bonds in a dynamic simulation. We have developed a set of force field parameters for the Ru-H system using a Monte Carlo global optimisation algorithm[25], which minimises an objective function of the form:

$$Error = \sum_{i=1}^n \left[ \frac{x_{i,ref} - x_{i,ReaxFF}}{\sigma_i} \right]^2 \quad (6.1)$$

where  $x_{i,ref}$  and  $x_{i,ReaxFF}$  are the reference value of the property and the value computed with ReaxFF respectively,  $\sigma_i$  represents the weighting of the property, and the sum is over all the entries in the training set.

The force field parameters are optimised against energies and charges obtained from first-principles calculations. The Vienna Ab Initio Simulation Package (VASP) [26–28] is used for all Density Functional Theory (DFT) calculations, which are performed with the generalized gradient approach as proposed by Perdew, Burke, and Ernzerhof (PBE) [29].

The convergence parameters are as follows: energy cutoff of 400 eV; residual force criterion of  $1 \times 10^{-2}$  eV/Å; energy convergence criterion of  $1 \times 10^{-5}$  eV. Slab calculations are performed with a  $(9 \times 9 \times 1)$   $\Gamma$ -centred  $k$ -points grid, while bulk calculations are done with a  $(9 \times 9 \times 9)$  grid; all atoms are allowed to relax in the optimization process. The training set includes Ru equations of state for multiple crystal structures, surface formation energies, H adsorption energies on Ru surfaces, hydride formation energies, and bond length scans. The parameters for H are taken from the set developed by Senftle et al[30] as a starting point, while the Ru and Ru-H parameters were newly-generated for this study. More information on the force field parameters and training set can be found in the Supporting Information.

The ReaxFF MD calculations are performed in the AMS2020 software package (version 2020.101) under licence from SCM[31]. All the MD simulations employ periodic boundary conditions in three directions, and are carried out with a velocity Verlet integrator with a timestep of 0.25 fs. The atom locations as a function of time are tracked at intervals of 250 fs, i.e. every 1000 timesteps. Initial velocities of the atoms are set according to a Maxwell-Boltzmann distribution at the target temperature. The system is then brought to equilibrium in a preparatory simulation of at least 0.1 ns duration. The main diffusion simulation is performed in an NVT ensemble with a Nosé–Hoover thermostat, for a duration of 10 to 12 ns. We extract from the NVT simulation trajectory the mean squared displacement (MSD) of the H atoms, using the MDAnalysis package[32–36]. Diffusion coefficients are calculated from the slope of the MSDs according to the Einstein-Smoluchowski relation:

$$D = \frac{\langle |\mathbf{r}_i(t + \tau) - \mathbf{r}_i(t)|^2 \rangle}{2d\tau}. \quad (6.2)$$

where  $\mathbf{r}$  is the position of the H atom,  $\tau$  is the elapsed time, and  $d$  is the dimensionality of the system. The average is taken over time steps and all H atoms. The temperature-dependent diffusion coefficients are fitted to the Arrhenius expression

$$D = D_0 e^{(-E_a/k_B T)}, \quad (6.3)$$

which yields a pre-exponential factor  $D_0$  and activation energy  $E_a$ , where  $k_B$  is the Boltzmann constant and  $T$  is the temperature. Hydrogen diffusion data are generated from MD simulations and analysed for three (3) representative structures: the pristine Ru crystal and the two (2) different types of GBs described below. The simulated structures are summarised in Table 6.1.

The crystallography of a GB can be described completely in terms of 5 parameters: 3 to describe the misorientation of the of the two grains, and 2 to describe the inclination of the boundary relative to the axes of either of the crystals. The misorientation is determined by the rotation axis, e.g. [0001] and  $38.21^\circ$  for the tilt GB, [0001] and  $21.79^\circ$  for the twist GB. The inclination of the boundary is defined by the GB plane, (01 $\bar{1}$ 0) for the tilt GB, (0001) for the twist GB. The coincidence site lattice (CSL) concept is a convenient way to denote special misorientations, rotation angles at which superposition

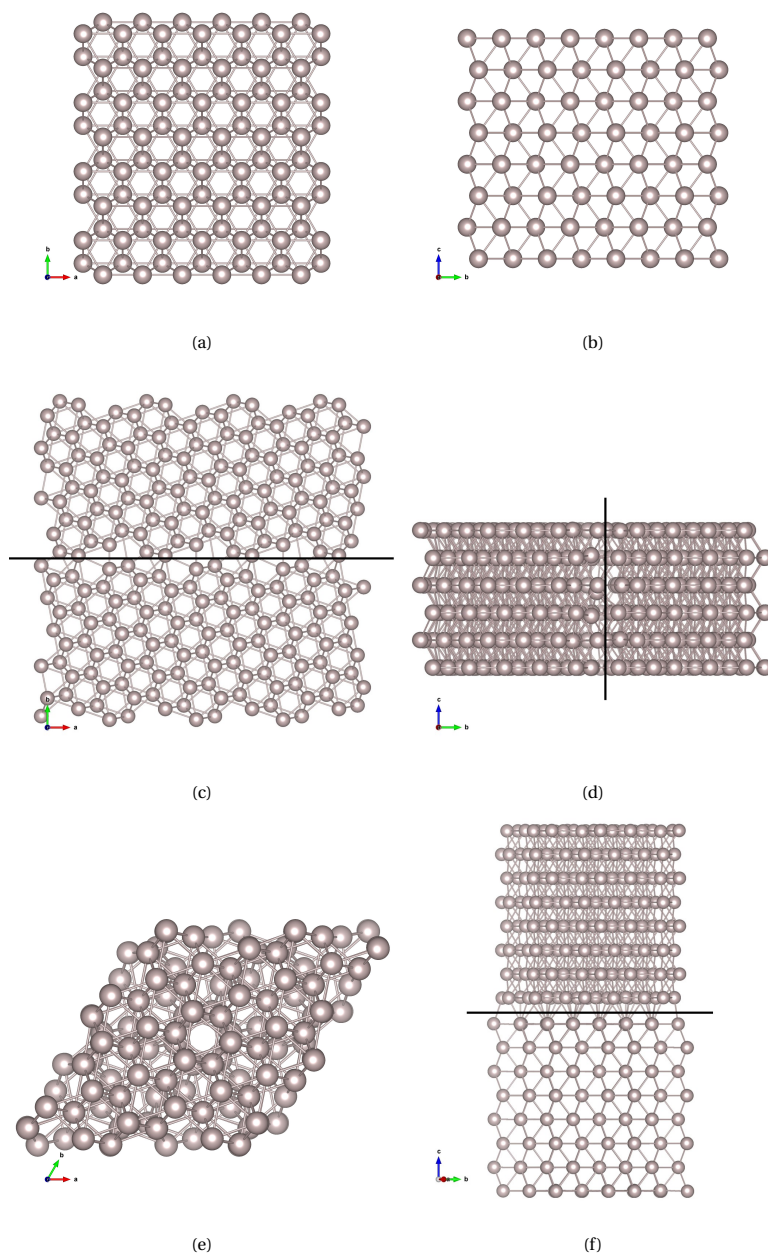


Figure 6.1: (a) Top view and (b) side view of pristine hcp Ru; (c) top view and (d) side view of  $\Sigma 7$  symmetric tilt GB; (e) top view and (f) side view of  $\Sigma 7$  twist GB. The black line marks the GB plane.

Table 6.1: Simulated Ru structures

Structure	Box dimensions (Å)	Number of Ru atoms	Number of H atoms
Pristine	40.6 × 37.5 × 34.3	3840	40
Σ7 tilt GB	27.0 × 46.8 × 42.8	3690	40
Σ7 twist GB	36.1 × 36.1 × 34.8	2800	28

of two crystals results in a number of lattice points coinciding and forming a sublattice of the two crystal lattices. The CSL is characterised by its  $\Sigma$  value, the ratio of the CSL's unit cell volume to the volume of the generating bulk lattice cell. Because the number of feasible GBs is very large, a thorough exploration of all types is impractical. Therefore, a selection of representative structures is necessary. The first requirement is low formation energy, which implies a high likelihood of occurrence. Another factor is the difference between the selected structures; the more dissimilar the systems simulated, the more information can be extracted. We have selected the  $\Sigma 7$  symmetric tilt GB and the  $\Sigma 7$  twist GB, with rotation about [0001]; they are generated with the free and open-source Atoms software[37] and illustrated in Figure 6.1. For a more thorough discussion of the chosen GBs and their properties, see Bruggeman et al[38] and Zheng et al[39].

## 6

## 6.3. RESULTS AND DISCUSSION

### 6.3.1. FORCE FIELD VALIDATION

We have performed a series of calculations to assess the accuracy of the Ru/H force field. The test cases include evaluation of the lattice parameters for the hexagonal close-packed (hcp) Ru crystal and mechanical properties. A comparison of the Ru bulk properties from ReaxFF and DFT is shown in Table 6.2. To demonstrate the predictive power of the parameters, an additional comparison of the energies of various surfaces (slab models) is also included.

The ReaxFF-computed lattice parameters  $a$  (2.73 Å) and  $c/a$  (1.60) for hexagonal close-packed (hcp) ruthenium are in good agreement with the DFT-computed values, and with the experimental data, 2.71 Å and 1.58, respectively [40]. The equilibrium volume per atom  $V_0$  is overestimated slightly, by 4%. Mechanical properties from the reference Density Functional Theory (DFT) calculations are also reproduced to a good standard as shown in Figure 6.2a. Bulk moduli calculated from Birch-Murnaghan equations of state are 313 and 333 GPa for ReaxFF and DFT respectively. The force field also shows

Table 6.2: HCP Ru properties from ReaxFF and DFT.

Method	$a$ (Å)	$c/a$	$V_0$ (Å) <sup>3</sup>	$B$ (GPa)
ReaxFF	2.73	1.60	14.2	332
DFT	2.72	1.58	13.7	312

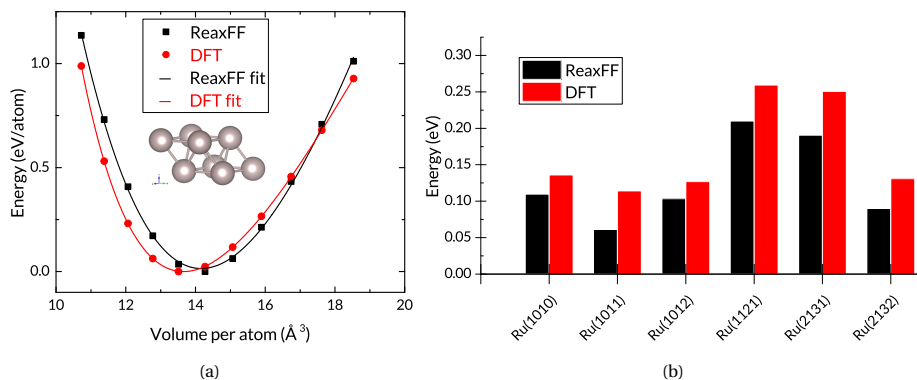


Figure 6.2: (a) Equations of state for hcp Ru from ReaxFF force field and DFT; and (b) energy per atom relative to Ru(0001)

a good qualitative reproduction of relative energies for a number of Ru slabs with different exposed facets. As shown in Figure 6.2b, although the absolute values are almost uniformly underestimated, the trend is fairly well-matched. The largest mismatch does not exceed 0.06 eV. It should be noted that these slabs were not included in the training set for the parametrisation, so they serve as a test of the force field's performance outside the training space.

6

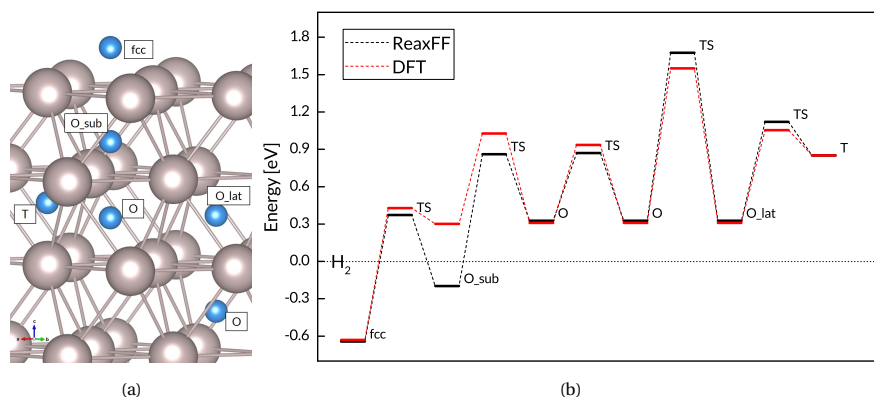


Figure 6.3: A comparison of adsorption energies and hydride formation energies (hydrogen at interstitial sites) on and in Ru, and energies of the transition states along the diffusion paths, obtained with the ReaxFF force field and the DFT reference[21].

For the diffusion simulations, it is especially important that the force field reproduce the energies of H in the interstitial states within the Ru bulk. Figure 6.3 shows a comparison of ReaxFF and DFT energies for key sites of H in Ru. The interstitial hydride

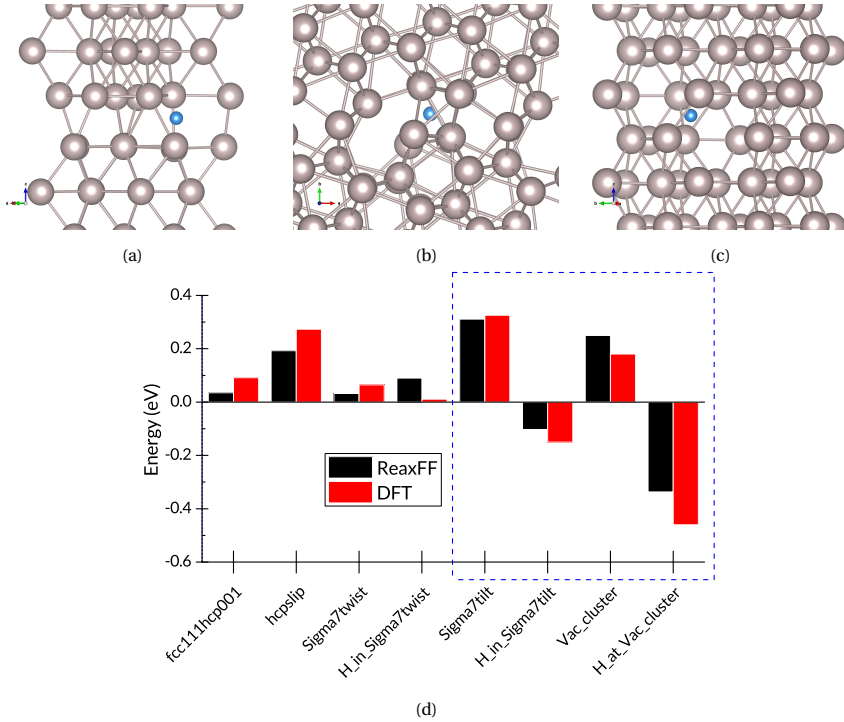


Figure 6.4: (a) H in twist GB, (b) H in tilt GB, (c) H at vacancy cluster, and (d) energy per atom for Ru stacking faults, GBs, and vacancy clusters; and hydride formation energies for H sites at defects.

formation energies are calculated as

$$\Delta E_H = \left( E_{M_xH_y} - E_M - \frac{y}{2} E_{H_2} \right), \quad (6.4)$$

where  $y$  is the number of H atoms, while  $E_{M_xH_y}$ ,  $E_M$ , and  $E_{H_2}$  stand respectively for the total energy of the metal hydride, the energy of the host metal structure, and the energy of a  $H_2$  molecule.

The agreement is good, within 0.15 eV for all but the octahedral site in the near-surface region, which is lower in energy than the  $H_2$  reference. The main deviation is found near the Ru(0001) surface. However, the discrepancy is unlikely to have a large impact on the simulated bulk diffusion. This conclusion is further strengthened by the force field's reproduction of GBs and defect formation energies. Figure 6.4d shows the energies of GBs and stacking faults, as well as the energies of H sites at the two GBs and at a vacancy cluster. The structures and energies within the blue rectangle are outside the training set. The reproduction of DFT energies is successful for all except two data points (H in twist GB and H at vacancy cluster), which differ by less than 0.1 eV.

## 6.3.2. H DIFFUSION IN PRISTINE RU

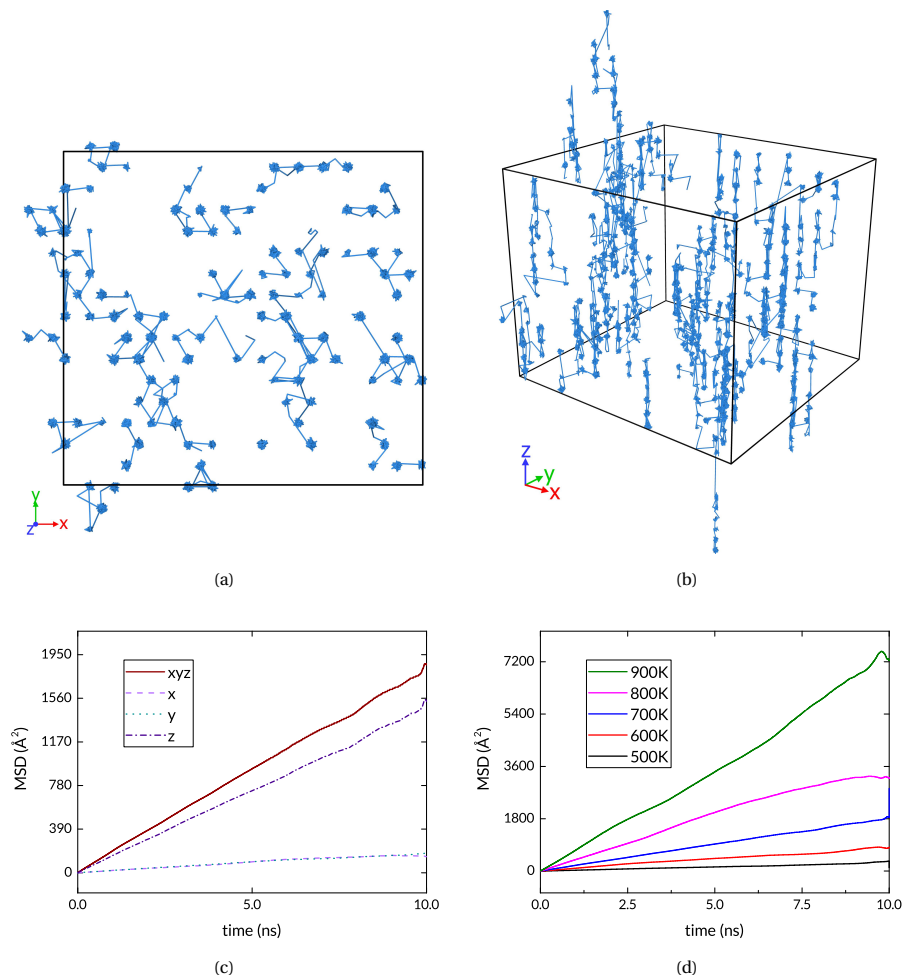


Figure 6.5: (a) & (b) H trajectories in pristine hcp Ru simulation at 700 K. (c) MSD at 700K; (d) MSD for all simulated temperatures.

H transport in Ru proceeds via a series of jumps between interstitial sites, over the energy barriers shown in Figure 6.3. The barriers indicate a preference for octahedral-to-octahedral jumps in the  $c$  direction of the hcp lattice, which is always the  $z$  direction in our coordinate system. This can be seen from the trajectories and the MSD plot in Figure 6.5. First we observe that the H paths include nodes situated at the octahedral sites, confirming that the solute atoms indeed spend many timesteps at these sites between successful hops. It is also apparent that more successful jumps occur in the  $z$  direction. The trajectories are unwrapped from the periodic translation into the simulation box, so the extent of the map in Figure 6.5b shows the disparity in vertical and horizontal

displacement. Figure 6.5c shows the MSD for the 700K NVT simulation. In the diffusive regime, a three-dimensional random walk through the interstitial sites, the MSD has a linear dependence on the elapsed time. The diffusive regime is reached quickly, as the H atoms quickly reach an equilibrium distribution in the intact lattice. The fluctuation at the long time scales is due to the progressively smaller number of data points with the large time lags. The MSD contribution of each of the spatial dimensions is also plotted; the full MSD is the sum of the MSDs in each spatial dimension. In keeping with the observed difference in trajectories, the MSD contribution of the  $x$  and  $y$  directions is much smaller than that of the  $z$  component. As expected, there is a monotonic increase in MSD as the temperature is increased, as shown in Figure 6.5d.

### 6.3.3. H DIFFUSION IN RU WITH TILT GB

The introduction of a tilt grain boundary has a marked effect on the rate and direction of H transport in Ru. As the trajectories in Figure 6.6 show, here too the extent of the unwrapped trajectories in the XY plane is much smaller than in the  $z$  direction. In each of the grains, the predominance of jumps along the  $z$  direction remains, and is overall enhanced within the GB. Here the atoms end up in channels, within which they remain, travelling mainly along the  $z$  direction. The MSD over the same duration as the pristine structure is doubled. Furthermore, it can be seen that there is a much smaller, essentially negligible contribution from diffusion in the  $xy$  plane.

The low energy of the GB sites (Figure 6.4) suggests that the H atoms will tend to be trapped at these sites, and this is reflected in the trajectory maps of Figure 6.6. There is little transport across the plane of the grain boundary, from one grain to the other. It follows that the equilibrium diffusive regime in this structure is reached only when the population of these GB sites stabilises. Figures 6.6e and 6.6f show the distribution of H atoms in the structure at the beginning and end of the NVT simulation. It can be seen that the interstitial sites in the grains are depleted, with the H population at the boundary rising accordingly. Figure 6.6g is a log-log plot of the MSD for all the simulated temperatures. It shows that the diffusive regime is reached quickly at the higher temperatures, with all the plots reaching a slope of unity by 500 ps; the exception is the 500K simulation which shows a rough match. This is likely because at such relatively low temperature (a) the H distribution is still out of equilibrium, and/or (b) the number of diffusion events being averaged is small. A closer view is shown in Figure 6.7 in which the region with the greatest density of trajectory lines can be seen. The tilt GB has channels with larger volume than the native hcp lattice allows, which explains their accommodation of the solute atoms. The image suggests a significant difference in the energy barriers for hops between sites within the channels, and the barrier to exit, with the latter being higher. Figure 6.7b shows a close-up of the side view of the tilt GB, in which 3 separate channels can be demarcated. No hopping between the middle and leftmost channel can be seen in the depicted region.

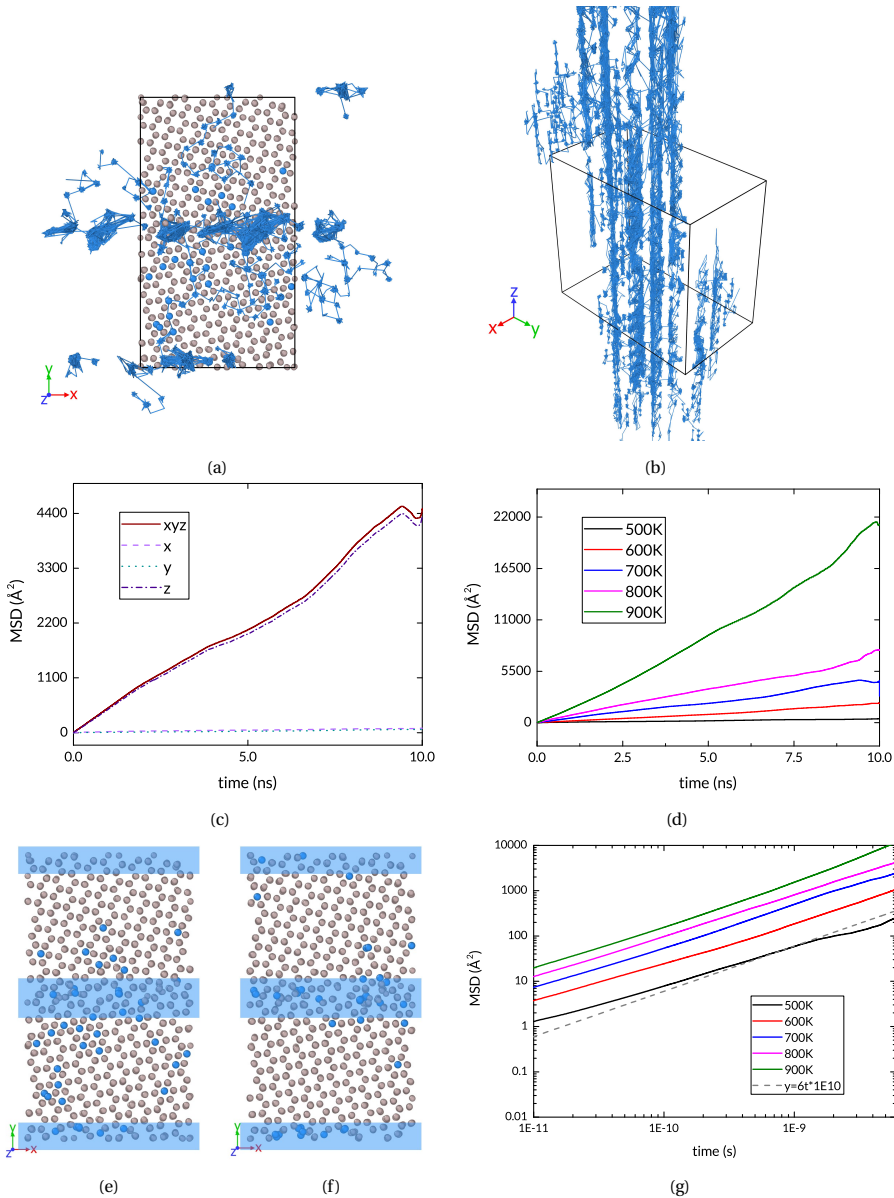


Figure 6.6: (a) & (b) H trajectories in tilt GB simulation at 700 K; (c) MSD at 700K; (d) MSD for all simulated temperatures; snapshots of (e) start and (f) end of tilt GB NVT simulation at 700 K, blue bands show GBs; (g) log-log MSD plot for all simulated temperatures of tilt GB. The dashed line has a slope of 1, which indicates a diffusive regime.

### 6.3.4. H DIFFUSION IN RU WITH TWIST GB

The second grain boundary structure also influences the diffusion process significantly. The plane of the boundary is horizontal, and the sites in the boundary put H atoms lower

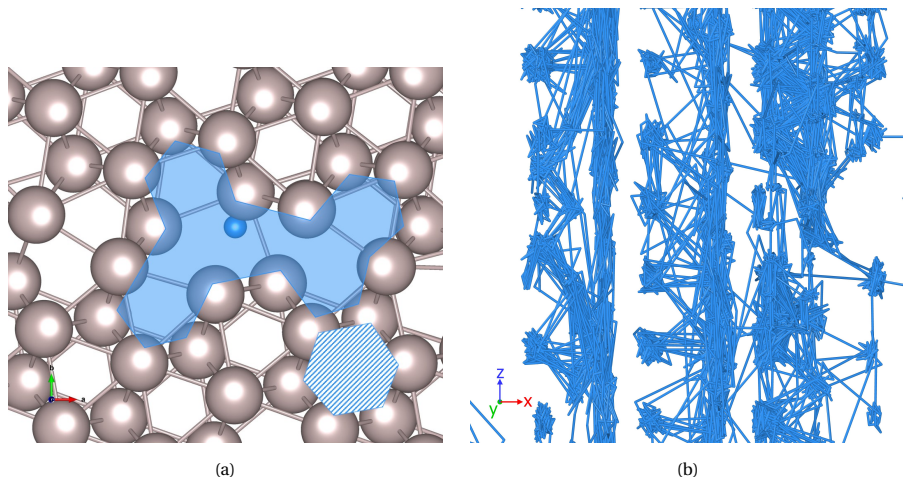


Figure 6.7: (a) Top view of H channel at tilt GB plane: the shaded hexagon shows the span of the octahedral site, while the semi-transparent irregular polygon shows the Ru-depleted GB channel; and (b) enlarged side view of tilt GB trajectory.

## 6

in energy than the octahedral site.

Figure 6.8 shows the H trajectories, which lie predominantly in the plane of the boundary. The movement of H atoms at the twist GB sites contrasts strongly with the tightly-bound vibrations at the octahedral site; the nodes of the latter are quite small, compared to the broadly-smeared loci at the former. Most importantly for the overall transport, this structure obstructs the otherwise dominant diffusion along the  $z$  direction, with the horizontal reach of the trajectory now greater. The MSD plot reflects this, with the  $z$  contribution practically zero, while the overall MSD magnitude is halfway between the values for the pristine structure and the tilt GB. The diffusion in the grains ultimately leads the solute atoms to accumulate at the boundary (Figure 6.8f). This proceeds at a temperature-dependent rate. The NVT simulation at 500 K does not reach the slope of a random-walk diffusive regime within the 12 ns duration of the run; all the higher-temperature simulations reach this by the 1 ns mark (Figure 6.8g). Figure 6.9 offers a closer look at the GB plane. The trajectory lines show that H atoms have a strong affinity for the sites in the GB plane. The twist GB has formed hexagonal “wheels” between the top and bottom grains, within which the H atom moves, jumping intermittently to an identical neighbouring region. These traps show up in the trajectory lines of Figure 6.8a as the large nodes. The hexagonal symmetry of the interfacing grains is reflected in the paths around and between these traps.

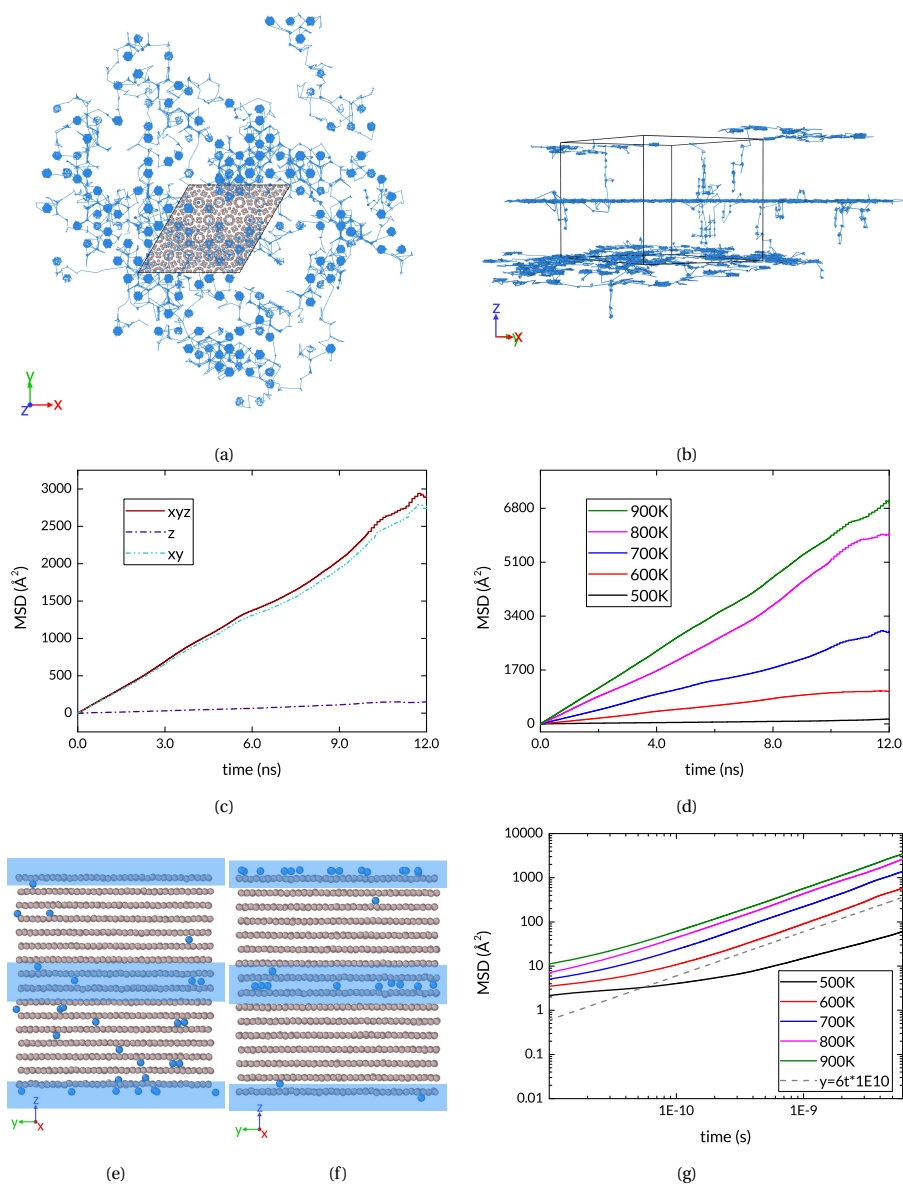


Figure 6.8: (a) & (b) H trajectories in twist GB simulation at 700 K; (c) MSD at 700K; (d) MSD for all simulated temperatures; snapshots of (e) start and (f) end of tilt GB NVT simulation at 700 K, blue bands show GBs; (g) log-log MSD plot for all simulated temperatures of twist GB. The dashed line has a slope of 1, which indicates a diffusive regime.

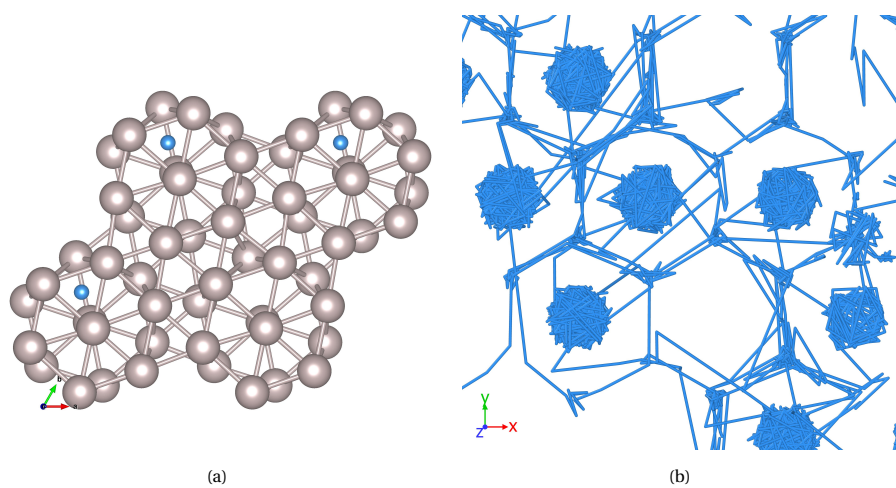


Figure 6.9: (a) H sites at twist GB plane: the wheels are formed by atoms from the interfacing grains; and (b) enlarged top view of twist GB trajectory.

### 6.3.5. DIFFUSION COEFFICIENTS

The MSD for each of the diffusion simulations yields the diffusion coefficient at each temperature, according to Equation 6.2. In both GBs, the diffusion is mostly restricted to the plane, such that the random-walk dimensionality is reduced to 2. Figure 6.5d shows a linear dependence of MSD on time for the entire duration of the simulation of the pristine Ru. However, the inhomogeneous GB structures do not reach a diffusive regime as rapidly. They also exhibit greater variation in the slope. Therefore the MSD slope is taken only after 40% of the simulation time has elapsed, and the slope of the MSD has matched that of a random walk. Furthermore, to account for the noise, the diffusion coefficient is averaged from 10 overlapping intervals between the 40% mark and the end of the simulation. The diffusion coefficients are plotted in Figure 6.10. We fit

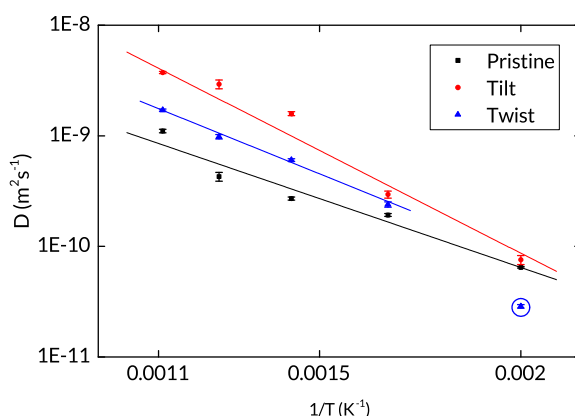


Figure 6.10: Diffusion coefficients for all simulated structures and temperatures; the point circled in blue is excluded from the fit, as it does not represent a diffusive regime.

the temperature-dependent diffusion coefficients to the Arrhenius expression. As shown in Figure 6.8g, the 500K twist GB simulation does not reach the diffusive regime; the diffusion coefficient is therefore not included in the fit. We obtain a pre-exponential factor  $D_0$  and activation energy  $Q$  for temperature-dependent H diffusion in each of the simulated structures. These are, in  $\text{m}^2\text{s}^{-1}$  and eV respectively:  $2.0 \times 10^{-8}$  and 0.25 for the pristine hcp Ru;  $4.5 \times 10^{-7}$  and 0.37 for the tilt GB structure; and  $7.3 \times 10^{-8}$  and 0.29 for the twist GB structure.

### 6.3.6. CONCLUSION

We have developed a ReaxFF force field for the Ru/H system which reproduces DFT energies with high accuracy. We have applied the force field to the study of H diffusion in Ru, a topic previously under-represented in literature. We performed simulations of H diffusion through a perfect Ru crystal and through tilt and twist GBs, which have yielded diffusion coefficients for H in hcp Ru crystal and in GBs. While they do not cover all pos-

sible GBS and defects which can influence H transport through polycrystalline Ru, the diffusion coefficients and the trajectory maps indicate that the character of H diffusion in Ru depends largely on the number and nature of GBs present.

Both the static calculations and the dynamic simulations show the presence of energetically favourable sites for H atoms in the boundary region. Also important is the fact that diffusion across the GBs is inhibited. These findings are similar to the results obtained for H in Al GBs[9]. However, although Pedersen et al. observed diffusion through H hopping from the GB site out into the grain, we find that the main trajectories lie within the GB. The diffusion coefficients we have extracted imply that at 300K, the diffusion rates in the tilt and twist GBs are slightly lower than that of the perfect crystal. We can surmise that in moving through polycrystalline Ru, H atoms will hop between interstitial sites until they reach a GB, within which they become confined. If the sites at the GB are occupied, an arriving H atom is repelled, as we observed minimal transport across GBs. For thin films, transport through the Ru will depend greatly on the morphology of the film. Since the Ru capping layers are mostly of (0001) orientation[41], the accumulation of H and preferential transport along the plane of the tilt GB suggests that this type of GB will dominate H diffusion through the films, enabling the so-called short-circuit diffusion through the film.

These results point to film morphology control as an important tool in preventing the permeation of hydrogen into multilayer mirrors. The results also give insight into the trapping and diffusion of H and other impurities in metal grain boundaries. The developed force field can be applied to the study of other phenomena, including surface interactions, while the results of the diffusion study will be of interest both for research and for technological applications.

## REFERENCES

- [1] S. K. Dwivedi and M. Vishwakarma, *Hydrogen embrittlement in different materials: A review*, International Journal of Hydrogen Energy **43**, 21603 (2018).
- [2] D. Herlach, C. Kottler, T. Wider, and K. Maier, *Hydrogen embrittlement of metals*, Physica B: Condensed Matter **290**, 443 (2000).
- [3] N. E. Nanninga, Y. S. Levy, E. S. Drexler, R. T. Condon, A. E. Stevenson, and A. J. Slifka, *Comparison of hydrogen embrittlement in three pipeline steels in high pressure gaseous hydrogen environments*, Corrosion Science **59**, 1 (2012).
- [4] Y. Ueda, J. Coenen, G. De Temmerman, R. Doerner, J. Linke, V. Philipps, and E. Tsitrone, *Research status and issues of tungsten plasma facing materials for ITER and beyond*, Fusion Engineering and Design **89**, 901 (2014).
- [5] A. S. Kuznetsov, M. A. Gleeson, and F. Bijkerk, *Temperature dependencies of hydrogen-induced blistering of thin film multilayers*, Journal of Applied Physics **115**, 173510 (2014).
- [6] A. Turnbull, *Hydrogen diffusion and trapping in metals*, in *Gaseous Hydrogen Embrittlement of Materials in Energy Technologies* (Elsevier, 2012) pp. 89–128.
- [7] J. Yao and J. Cahoon, *Experimental studies of grain boundary diffusion of hydrogen in metals*, Acta Metallurgica et Materialia **39**, 119 (1991).
- [8] M. Ichimura, Y. Sasajima, and M. Imabayashi, *Grain Boundary Effect on Diffusion of Hydrogen in Pure Aluminum*, Materials Transactions, JIM **32**, 1109 (1991).
- [9] A. Pedersen and H. Jónsson, *Simulations of hydrogen diffusion at grain boundaries in aluminum*, Acta Materialia **57**, 4036 (2009).
- [10] X. Yao, Z. H. Zhu, H. M. Cheng, and G. Q. Lu, *Hydrogen diffusion and effect of grain size on hydrogenation kinetics in magnesium hydrides*, Journal of Materials Research **23**, 336 (2008).
- [11] P. Feulner and D. Menzel, *The adsorption of hydrogen on ruthenium (001): Adsorption states, dipole moments and kinetics of adsorption and desorption*, Surface Science **154**, 465 (1985).
- [12] M. Luppi, R. A. Olsen, and E. J. Baerends, *Six-dimensional potential energy surface for H<sub>2</sub> at Ru(0001)*, Phys. Chem. Chem. Phys. **8**, 688 (2006).
- [13] C. Bruneau and P. H. Dixneuf, *Topics in Organometallic Chemistry*, Topics in Organometallic Chemistry, Vol. 48 (Springer International Publishing, 2014).
- [14] R. B. McLellan and W. A. Oates, *The solubility of hydrogen in rhodium, ruthenium, iridium and nickel*, Acta Metallurgica **21**, 181 (1973).

- [15] A. Driessen, P. Sanger, H. Hemmes, and R. Griessen, *Metal hydride formation at pressures up to 1 Mbar*, *Journal of Physics: Condensed Matter* **2**, 9797 (1990).
- [16] O. Soroka, J. M. Sturm, C. J. Lee, H. Schreuders, B. Dam, and F. Bijkerk, *Hydrogen diffusion through Ru thin films*, *International Journal of Hydrogen Energy* **45**, 15003 (2020).
- [17] X. W. Zhou, R. Dingreville, and R. A. Karnesky, *Molecular dynamics studies of irradiation effects on hydrogen isotope diffusion through nickel crystals and grain boundaries*, *Physical Chemistry Chemical Physics* **20**, 520 (2017).
- [18] S. M. Teus and V. G. Gavriljuk, *Grain-boundary diffusion of hydrogen atoms in the  $\alpha$ -iron*, *Metallofizika i Noveishie Tekhnologii* **36**, 1399 (2014).
- [19] Y. Yu, X. Shu, Y. N. Liu, and G. H. Lu, *Molecular dynamics simulation of hydrogen dissolution and diffusion in a tungsten grain boundary*, *Journal of Nuclear Materials* **455**, 91 (2014).
- [20] U. Von Toussaint, S. Gori, A. Manhard, T. Höschen, and C. Höschen, *Molecular dynamics study of grain boundary diffusion of hydrogen in tungsten*, *Physica Scripta T* **T145** (2011), 10.1088/0031-8949/2011/T145/014036.
- [21] C. Onwudinanti, I. Tranca, T. Morgan, and S. Tao, *Tin, The Enabler—Hydrogen Diffusion into Ruthenium*, *Nanomaterials* **9**, 129 (2019).
- [22] A. C. T. van Duin, S. Dasgupta, F. Lorant, and W. A. Goddard, *ReaxFF: A Reactive Force Field for Hydrocarbons*, *The Journal of Physical Chemistry A* **105**, 9396 (2001).
- [23] K. Chenoweth, A. C. Van Duin, P. Persson, M. J. Cheng, J. Oxgaard, and W. A. Goddard, *Development and application of a ReaxFF reactive force field for oxidative dehydrogenation on vanadium oxide catalysts*, *Journal of Physical Chemistry C* **112**, 14645 (2008).
- [24] M. F. Russo and A. C. Van Duin, *Atomistic-scale simulations of chemical reactions: Bridging from quantum chemistry to engineering*, *Nuclear Instruments and Methods in Physics Research, Section B: Beam Interactions with Materials and Atoms* **269**, 1549 (2011).
- [25] E. Iype, M. Hütter, A. P. Jansen, S. V. Nedeia, and C. C. Rindt, *Parameterization of a reactive force field using a monte carlo algorithm*, *Journal of Computational Chemistry* **34**, 1143 (2013).
- [26] G. Kresse and J. Hafner, *Ab initio molecular-dynamics simulation of the liquid-metalamorphous- semiconductor transition in germanium*, *Physical Review B* **49**, 14251 (1994).

- [27] G. Kresse and J. Furthmüller, *Efficiency of ab-initio total energy calculations for metals and semiconductors using a plane-wave basis set*, Computational Materials Science **6**, 15 (1996).
- [28] D. Joubert, *From ultrasoft pseudopotentials to the projector augmented-wave method*, Physical Review B - Condensed Matter and Materials Physics **59**, 1758 (1999).
- [29] J. D. Perdew, K. Burke, and M. Ernzerhof, *Generalized Gradient Approximation Made Simple*, Physical Review Letters **77**, 3865 (1996).
- [30] T. P. Senftle, M. J. Janik, and A. C. T. van Duin, *A ReaxFF Investigation of Hydride Formation in Palladium Nanoclusters via Monte Carlo and Molecular Dynamics Simulations*, The Journal of Physical Chemistry C **118**, 4967 (2014).
- [31] R. Rüger, M. Franchini, T. Trnka, A. Yakovlev, E. Van Lenthe, P. Philippen, T. Van Vuren, B. Klumpers, and T. Soini, *AMS 2021.1, SCM, Theoretical Chemistry, Vrije Universiteit, Amsterdam, The Netherlands*, <http://www.scm.com>. (2021).
- [32] N. Michaud-Agrawal, E. J. Denning, T. B. Woolf, and O. Beckstein, *MDAnalysis: A toolkit for the analysis of molecular dynamics simulations*, Journal of Computational Chemistry **32**, 2319 (2011).
- [33] R. Gowers, M. Linke, J. Barnoud, T. Reddy, M. Melo, S. Seyler, J. Domański, D. Dotson, S. Buchoux, I. Kenney, and O. Beckstein, *MDAnalysis: A Python Package for the Rapid Analysis of Molecular Dynamics Simulations*, in *Proceedings of the 15th Python in Science Conference, Scipy* (2016) pp. 98–105.
- [34] E. J. Maginn, R. A. Messerly, D. J. Carlson, D. R. Roe, and J. R. Elliott, *Best Practices for Computing Transport Properties I. Self-Diffusivity and Viscosity from Equilibrium Molecular Dynamics [Article v1.0]*, Living Journal of Computational Molecular Science **1**, 1 (2019).
- [35] V. Calandrini, E. Pellegrini, P. Calligari, K. Hinsens, and G. Kneller, *nMoldyn - Interfacing spectroscopic experiments, molecular dynamics simulations and models for time correlation functions*, École thématique de la Société Française de la Neutronique **12**, 201 (2011).
- [36] P. de Buyl, *tidynamics: A tiny package to compute the dynamics of stochastic and molecular simulations*, Journal of Open Source Software **3**, 877 (2018).
- [37] P. Hirel, *Atomsk: A tool for manipulating and converting atomic data files*, Computer Physics Communications **197**, 212 (2015).
- [38] G. A. Bruggeman, G. H. Bishop, and W. H. Hartt, *Coincidence and Near-Coincidence Grain Boundaries in HCP Metals*, in *The Nature and Behavior of Grain Boundaries*, 1 (Springer US, New York, NY, 1972) pp. 83–122.

- [39] H. Zheng, X. G. Li, R. Tran, C. Chen, M. Horton, D. Winston, K. A. Persson, and S. P. Ong, *Grain boundary properties of elemental metals*, *Acta Materialia* **186**, 40 (2020).
- [40] H. King, *Crystal structures and lattice parameters of allotropes of the elements*, in *CRC Handbook of Chemistry and Physics* (CRC Press, 2012) pp. 15–18.
- [41] S. Bajt, N. V. Edwards, and T. E. Madey, *Properties of ultrathin films appropriate for optics capping layers exposed to high energy photon irradiation*, *Surface Science Reports* **63**, 73 (2008).

## APPENDIX

## FORCE FIELD PARAMETERS

```

Reactive MD force field: RuH
39      ! Number of general parameters
50.0000 !p_boc1 Eq(4c): Overcoordination parameter
9.5469  !p_boc2 Eq(4d): Overcoordination parameter
1.6725  !p_coa2 Eq(15): Valency angle conjugation
1.7224  !p_trip4 Eq(20): Triple bond stabilisation
6.8702  !p_trip3 Eq(20): Triple bond stabilisation
60.4850 !k_c2 Eq(19): C2-correction
1.0588  !p_ovun6 Eq(12): Undercoordination
4.6000  !p_trip2 Eq(20): Triple bond stabilisation
12.1176 !p_ovun7 Eq(12): Undercoordination
13.3056 !p_ovun8 Eq(12): Undercoordination
-70.5044 !p_trip1 Eq(20): Triple bond stabilization
0.0000  !Lower Taper-radius (must be 0)
10.0000 !R cut Eq(21): Upper Taper-radius
2.8793  !p_fe1 Eq(6a): Fe dimer correction
33.8667 !p_val6 Eq(13c): Valency undercoordination
6.0891  !p_lpl Eq(8): Lone pair param
1.0563  !p_val9 Eq(13f): Valency angle exponent
2.0384  !p_val10 Eq(13g): Valency angle parameter
6.1431  !p_fe2 Eq(6a): Fe dimer correction
6.9290  !p_pen2 Eq(14a): Double bond/angle param
0.3989  !p_pen3 Eq(14a): Double bond/angle param
3.9954  !p_pen4 Eq(14a): Double bond/angle param
-2.4837 !p_fe3 Eq(6a): Fe dimer correction
5.7796  !p_tor2 Eq(16b): Torsion/BO parameter
10.0000 !p_tor3 Eq(16c): Torsion overcoordination
1.9487  !p_tor4 Eq(16c): Torsion overcoordination
-1.2327 !p_elho Eq(26a): electron-hole interaction
2.1645  !p_cot2 Eq(17b): Conjugation if torsl3=0
1.5591  !p_vdW1 Eq(23b): vdWals shielding
0.1000  !Cutoff for bond order (*100)
1.7602  !p_coa4 Eq(15): Valency angle conjugation
0.6991  !p_ovun4 Eq(11b): Over/Undercoordination
50.0000 !p_ovun3 Eq(11b): Over/Undercoordination
1.8512  !p_val8 Eq(13d): Valency/lone pair param
0.5000  !X soft Eq(25): ACKS2 softness for X ij
20.0000 !d Eq(23d): Scale factor in lg-dispersion
5.0000  !p_val Eq(27): Gauss exponent for electrons
0.0000  !l Eq(13e): disable undecoord in val angle
0.7903  !p_coa3 Eq(15): Valency angle conjugation
2      ! Nr of atoms; cov.r; valency;a.m;Rvdw;Evdw;gammaEEM;cov.r2;#
      alfa;gammavdW;valency;Eunder;Eover;chiEEM;etaEEM;n.u.
      cov r3;EIp;Heat inc.;bol131;bol132;bol133;softcut;n.u.
      ov/un;val1;n.u.;val3,vval4
H      0.8930  1.0000  1.0080  1.3550  0.0930  0.8203  -0.1000  1.0000
      8.2230  33.2894  1.0000  0.0000  121.1250  3.7248  9.6093  1.0000
      -0.1000  0.0000  55.1878  3.0408  2.4197  0.0003  1.0698  0.0000
      -19.4571  4.2733  1.0338  1.0000  2.8793  0.0000  0.0000  0.0000
Ru     2.6757  4.0000  101.0700  3.7443  0.0394  0.8412  -1.0000  4.0000
      11.0901  41.5093  4.0000  0.0000  0.0000  3.0356  6.7556  0.0000
      -1.0000  0.0000  10.1626  109.5355  76.2738  0.0009  0.8563  0.0000
      -1.0840  0.8894  1.0338  8.0000  2.5791  0.0000  0.0000  0.0000
3      ! Nr of bonds; Edis1;Lppen;n.u.;pbel;pbo5;l3corr;pbo6
      pbe2;pbo3;pbo4;n.u.;pbo1;pbo2;ovcorr
1 1 153.3934  0.0000  0.0000  -0.4600  0.0000  1.0000  6.0000  0.7300
      6.2500  1.0000  0.0000  1.0000  -0.0790  6.0552  0.0000  0.0000
1 2 110.8446  0.0000  0.0000  -0.6157  0.0000  1.0000  16.0000  0.5137
      0.1307  1.0000  0.0000  1.0000  -0.4436  6.1985  0.0000  0.0000
2 2 117.1478  0.0000  0.0000  -0.6450  -0.2000  0.0000  16.0000  0.1685
      15.8671  -0.2000  15.0000  1.0000  -0.0221  9.5113  0.0000  0.0000
1      ! Nr of off-diagonal terms; Ediss;Ro;gamma;rsigma;rpi;rpi2
1 2 0.2510  1.2762  10.8237  2.2667  -1.0000  -1.0000
5      ! Nr of angles;at1;at2;at3;Theta,o;ka;kb;pv1;pv2
1 1 1 0.0000  7.9213  0.8635  0.0000  0.0000  0.0000  1.0400
1 2 1 -0.2670  0.2116  1.7042  0.0000  1.4791  0.0000  3.1294
2 1 2 0.0000  1.7341  2.1648  0.0000  0.8397  0.0000  2.7364
1 1 2 0.0000  25.3724  7.3597  0.0000  2.5136  0.0000  3.1412
1 2 2 64.6157  27.9453  0.0199  0.0000  0.0948  0.0000  3.5155
0      ! Nr of torsions;at1;at2;at3;at4;;V1;V2;V3;V2(BO);vconj;n.u;n
0      ! Nr of hydrogen bonds;at1;at2;at3;Rhb;Dehb;vhl

```

### REAXFF TRAINING SET

The fitting of parameters for the force field was done with a training set which includes Ru equations of state for multiple crystal structures (hcp, fcc, bcc, sc), surface formation energies (slabs of hcp Ru, fcc Ru, bcc Ru), H adsorption energies on the same slabs, interstitial hydride formation energies (up to 0.25 H/Ru concentration), and bond length scans (Ru-Ru and Ru-H in RuH<sub>4</sub>). Figures 6.A1 and 6.A2 show samples of the training set.

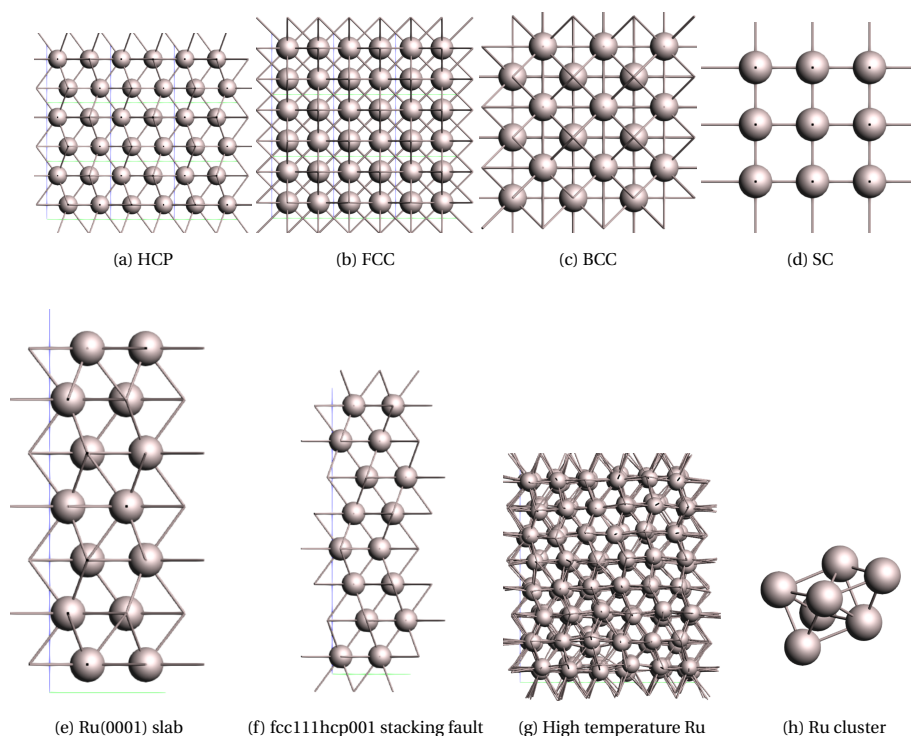


Figure 6.A1: Examples of structures included in the Ru training set.

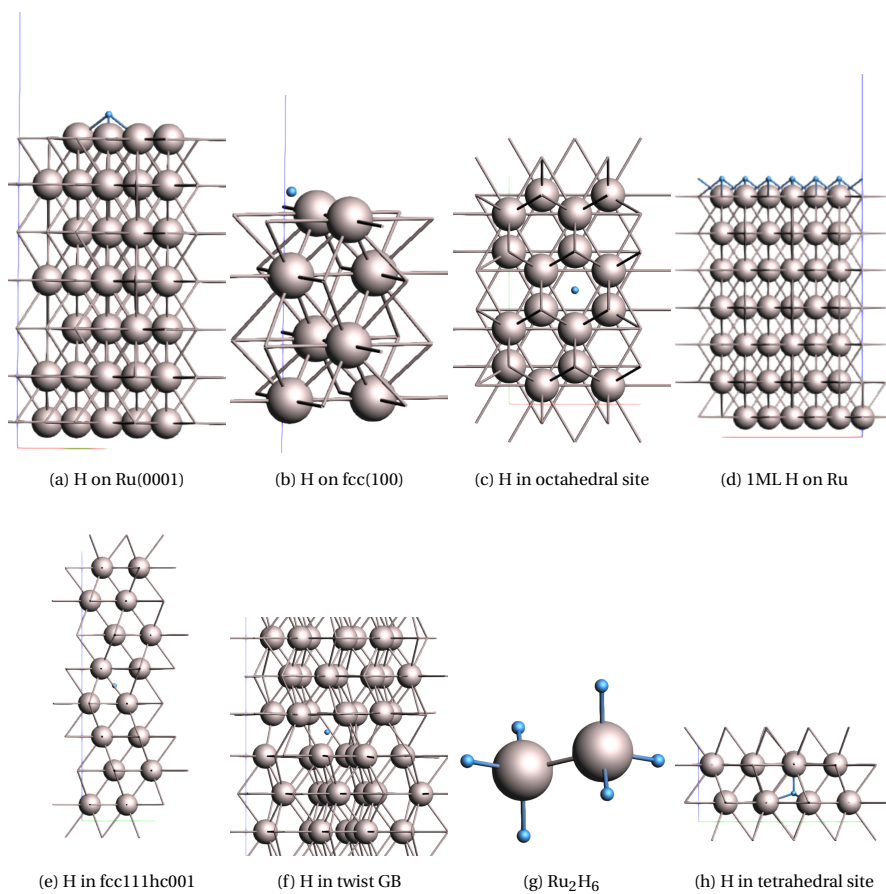


Figure 6.A2: Examples of structures included in the Ru-H training set.

## MSD PLOTS

In this section are MSD plots for each of the simulated structures at temperatures 500, 600, 800, and 900K. Note that the scales on the vertical axis differ significantly.

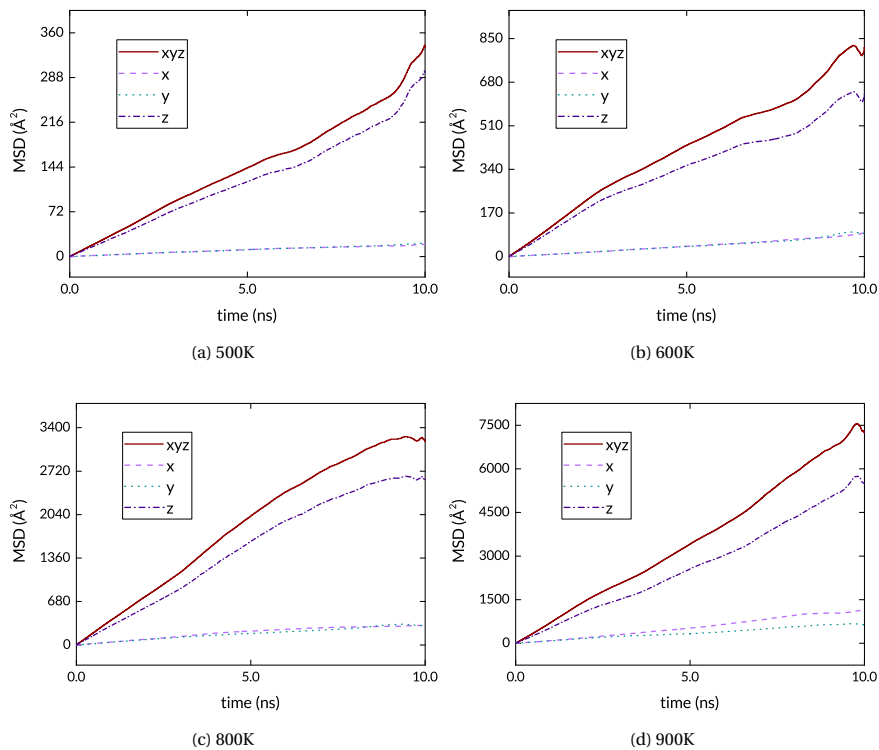


Figure 6.A3: MSD plots for NVT simulations of H in pristine Ru.

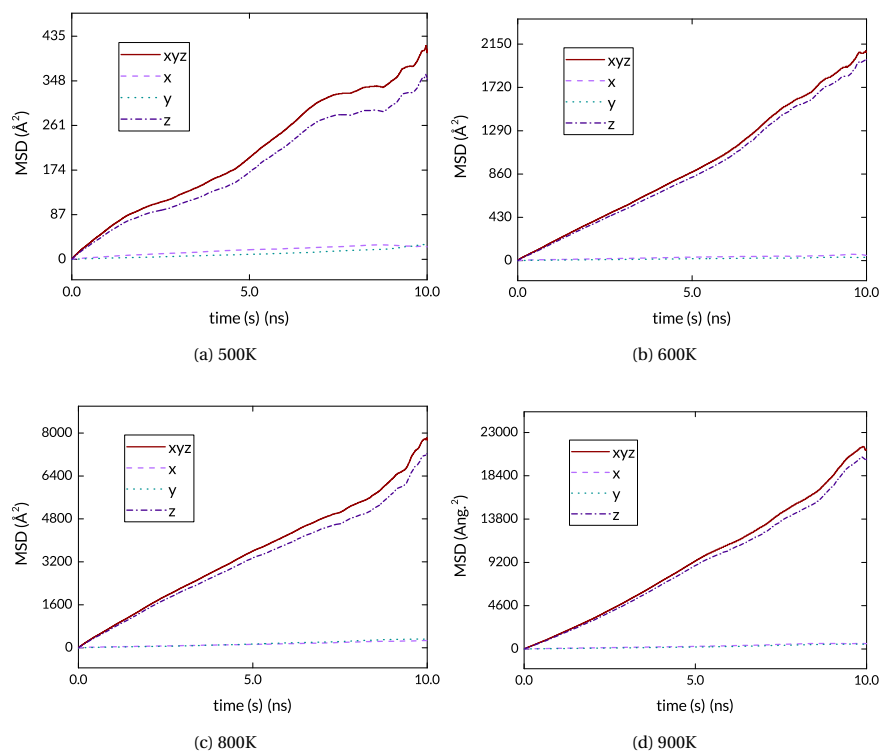


Figure 6.A4: MSD plots for NVT simulations of H in Ru tilt GB.

For the twist GB, at the lower temperature of 500K, the square root of the MSD is less than half the dimension of the simulation box. This heuristic implies that longer simulations are necessary to properly sample diffusion at this temperature.

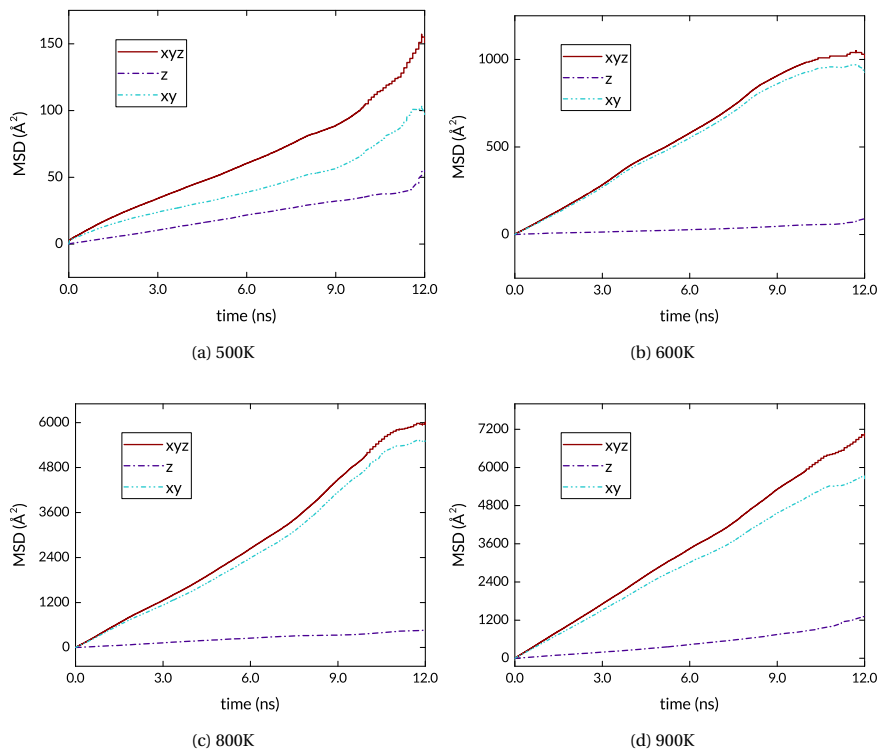


Figure 6.A5: MSD plots for NVT simulations of H in Ru twist GB.

# 7

## CONCLUSIONS AND OUTLOOK

The enormous demand for faster, smaller, cheaper, and more efficient microprocessors in the present and the foreseeable future has led to the development of extreme ultraviolet lithography, in a bid to extend Moore's law. The technological complexity of EUV machines has led to intense scientific research in many fields, including the study of hydrogen interaction with metals. The damaging effect of hydrogen on ruthenium-capped multilayer mirrors with tin contaminants leads to reduced productivity and higher costs. Therefore, a thorough understanding of the mechanism via which tin facilitates hydrogen-induced blistering is of great importance. This dissertation contributes an atomistic explanation of the ruthenium-tin-hydrogen interaction which ultimately leads to hydrogen accumulation in blisters.

The study begins with first-principles calculations of H interaction with the surfaces and crystals of Ru and Sn. We find that the energies of H adsorption on Ru and Sn surfaces are negative and positive respectively. These results establish that H adsorption on Ru is favourable, whereas on Sn it is unlikely. Indeed, the  $H_2$  molecule will dissociate into discrete H atoms on the Ru surface. This indicates that Sn is not increasing the supply of atomic H on the Ru surface via dissociation. Our calculations of H in the Ru and Sn crystals showed positive formation energies, i.e. low solubility in both. Since a first step to blistering would necessarily be penetration into the top layer, the energy barrier was tested in a number of different Sn-H configurations on the Ru surface. The energy barrier to H penetration into the subsurface is found to be reduced in the presence of tin. With  $SnH_4$  present, the barrier is found to be as low as 25% of the value without tin. An analysis of the bonding interactions shows complex and subtle electron transfer at the surface; from Sn to Ru and H. The electron density accumulation at the surface can explain the tendency of the system to minimize energy with H in the subsurface.

As the early calculations showed, H solubility in Ru is generally low, and significant

quantities of H in Ru are observed only at high temperatures and pressures. However, the formation of high-pressure pockets of H<sub>2</sub> indicates that a large quantity passes through the Ru film. An investigation of H diffusion in the near-surface region of Ru explains why H does not exit the Ru film, but diffuses to the underlying interface. The competition for surface adsorption sites between H in the subsurface and atomic H above the surface favours the latter, with the result that access to the saturated H surface is blocked. The co-adsorption of Sn exacerbates the site-blocking effect. Direct recombination with surface H also faces a large energy barrier. In other words, not only does Sn promote H into the subsurface, it also inhibits its return to the surface, making it more likely to diffuse to the opposite interface, where it contributes to blistering.

The two factors described above – lowering the barrier and blocking the exit – are demonstrated for separate or isolated Sn atoms. These effects are shown to occur in proximity to an adsorbed Sn atom or SnH<sub>4</sub> molecule. The case with larger amounts of Sn is also examined in this work. First it is shown that a mono-atomic layer of Sn forms readily on the Ru surface, with a strong adsorption energy of  $-1.2$  eV/atom. Subsequent layers do not bind to the layer beneath as strongly, indicating a preference to form three-dimensional islands after the first wetting layer. Thus the Stranski-Krastanov growth mode is demonstrated. Further calculations investigate the passage of H through multiple Sn layers on Ru. The results show that while a single layer of Sn allows H to pass through to the Ru surface and below, multiple layers impede the progress of H. On the basis of the results obtained, the conditions for H penetration to the Ru subsurface can then be summarized as follows: penetration is absent or negligible through a bare Ru surface, since the energy barrier is high, but a Ru surface with Sn atoms, Sn hydrides, or a Sn layer will result in a lowering of the barrier to entry.

The next step in the blistering process is the transport of H through the Ru film, which is studied in a series of molecular dynamics simulations. First-principles calculations give the energy barriers for each of the elementary jumps of H atoms from one interstitial site to another, and thus give a general indication of the kinetics of H transport. Quantitative evaluation of transport properties, in this case diffusion coefficients, require observation of the system's time evolution. MD offers the possibility of direct simulation of H transport not only in the perfect Ru crystal, but also in defective structures, primarily grain boundaries. To make such simulations possible, an interatomic potential (force field) in the ReaxFF method was developed on the basis of the previously acquired first-principles data and new calculations performed specifically for the development of the force field. Simulations of H transport are performed in three structures: pristine hcp Ru, Ru with a symmetric tilt grain boundary, and Ru with a twist grain boundary. The pristine crystal shows the H hopping between interstitial sites in the manner which is typical for metals, with a marked preference for the direction parallel to the *c* crystal lattice direction. Further simulation of H diffusion in defective structures shows the importance of grain boundaries for overall transport. Grain boundaries are shown to be very favourable for H occupation. The consequence is that both types of grain bound-

aries act as sinks and highways; the low-energy sites bind H such that H trajectories lie predominantly within the grain boundaries. The diffusion coefficients suggest that grain boundaries may slow diffusion at the temperatures of relevance to EUV systems.

The research findings have a number of implications for the issue of H-induced blistering of Ru in the presence of Sn. The immediate and trivial solution would be a change in the capping material. Sn binds strongly to Ru, and also makes it less impervious to H. Alternative materials such as oxides or nitrides are unlikely to interact with Sn and H in the same way as ruthenium. However, the material choice depends on numerous other factors, such as optical, mechanical, and chemical properties. The most obvious constraint is that reflectivity must be maintained at a high level. Moreover, the replacement material must be hard and resistant to sputtering and EUV-induced damage. The atoms must have low mobility, to reduce intermixing with the underlying layer(s). Finally, it must not be chemically active; oxides for instance may be reduced by the atomic H quite readily. Considering this long list of requirements, it becomes clear that an alternative capping layer is not so easily found.

Two other possibilities present themselves, given the fact that it is diffusible hydrogen which causes damage. First, the Ru thin film can be fabricated in such a manner as to reduce H mobility within it. As the MD simulations indicate, grain boundaries have low-energy sites which reduce H mobility at low temperatures. It may well be that polycrystalline films with desirable grain boundary properties will obstruct the passage of H through the film, slowing the accumulation of H atoms at the interface. In the ultimate case, amorphous Ru films might provide such an H-blocking layer. A second option is the use of alloying elements to improve the capping layer's performance. In the case of steel, for instance, certain alloying elements have proven to improve the material's resistance to H-induced damage by retarding H transport through the lattice, slowing the coalescence in voids and cracks which leads to embrittlement[1, 2]. This direction is worth exploring, particularly in combination with tailored film morphology.

Beyond EUV lithography, the Ru-Sn-H interaction holds promise. The sustainable hydrogen economy will likely require cost-effective methods of extracting pure H<sub>2</sub> from a mixture of gases. Contrasting with the deleterious effect on multilayer mirrors, the increased permeation of H through Ru could serve as a separation technique. Currently, palladium (Pd) is the standard material used in metal membranes for H separation[3]. H<sub>2</sub> dissociates on the Pd surface, then passes through the Pd film to recombine on the opposite side of the membrane. This process is driven by the large difference in partial pressure on the upstream and downstream sides of the membrane. One could imagine a separation membrane made of a thin Ru film with a (sub-)monolayer Sn coating on the upstream side which would result in a similar selective permeation of H. Assuming a flux comparable to Pd membranes – a substantial assumption, presumably – such a membrane would be an attractive alternative due to the high cost of Pd compared to Sn and Ru.

Although much has been made clear in the course of this research project, questions

remain, and new ones have arisen. One of these is the effect of tin on grain boundaries. We have demonstrated a promotion of blistering for the Ru(0001) surface, and have noted the influence of grain boundaries on the overall transport of hydrogen through ruthenium. It is yet to be seen what occurs between the three elements at such regions as triple junctions, which might play a large role in blister formation. Other questions include the time evolution of the blistering process; the sensitivity to different parameters such as pressure, flux, temperature; and the extent to which small-scale DFT and MD calculations are representative of the real systems. To begin with, more techniques can be applied to the system, building on the results reported here. The kinetic Monte Carlo (KMC) method offers the opportunity to go beyond the time constraints of molecular dynamics. The different states on the surface and in the bulk, as well as the transition rates between the states, can serve as input into a Monte Carlo model which simulates the time evolution of the penetration, diffusion, and blistering. With a more complete list of states and rates, extracted from DFT and MD, quantitative measures can be taken of how blistering depends on various parameters. Yet another avenue is considering this interaction for non-ideal Ru surfaces. Due to the limitations of *ab initio* methods, they cannot be applied to the study of defective, disordered structures without enormous computational expense, so the surface is modelled as a static, ordered entity. Steps, terraces, adatoms, and grain boundaries are examples of such features which may occur, but cannot be explored thoroughly. Since any real multilayer mirror or experimental sample will likely have or eventually develop imperfections, the effects of such imperfections call for closer examination. *Ab initio* thermodynamics, first-principles microkinetics, and molecular dynamics simulations can be particularly useful here, as they have been in the study of catalysis and surface science in general. Combining these techniques with new information and insights from real-world testing and examples will lead to a more complete mechanistic and macroscopic understanding of hydrogen-induced blistering.

**REFERENCES**

- [1] H. K. D. H. Bhadeshia, *Prevention of Hydrogen Embrittlement in Steels*, ISIJ International **56**, 24 (2016).
- [2] M. He, C. Onwudinanti, Y. Zheng, X. Wu, Z. Zhang, and S. Tao, *Ab initio study of metal carbide hydrides in the 2.25Cr1Mo0.25V steel*, Physical Chemistry Chemical Physics **23**, 5199 (2021).
- [3] N. A. Al-Mufachi, N. V. Rees, and R. Steinberger-Wilkens, *Hydrogen selective membranes: A review of palladium-based dense metal membranes*, Renewable and Sustainable Energy Reviews **47**, 540 (2015).



# LIST OF PUBLICATIONS

## Publications, first author:

- Onwudinanti, C., Tranca, I., Morgan, T., & Tao, S. (2019). Tin, the enabler – hydrogen diffusion into ruthenium. *Nanomaterials*, 9(1), 129. <https://doi.org/10.3390/nano9010129>
- Onwudinanti, C., Brocks, G., Koelman, V., Morgan, T., & Tao, S. (2020). Hydrogen diffusion out of ruthenium—an ab initio study of the role of adsorbates. *Physical Chemistry Chemical Physics*, 22(15), 7935–7941. <https://doi.org/10.1039/d0cp00448k>
- Onwudinanti, C., Brocks, G., Koelman, V., Morgan, T., & Tao, S. (2021). Tin deposition on ruthenium and its influence on blistering in multi-layer mirrors. *Physical Chemistry Chemical Physics*. <https://doi.org/10.1039/D1CP01082D>
- Onwudinanti, C., Pols, M., Brocks, G., Koelman, V., Van Duin, A., Morgan, T., & Tao, S. (2021). A molecular dynamics study of hydrogen diffusion in ruthenium (Submitted)

## Publications, co-author:

- He, M., Onwudinanti, C., Zheng, Y., Wu, X., Zhang, Z., & Tao, S. (2021). Ab initio study of metal carbide hydrides in the 2.25Cr1Mo0.25V steel. *Physical Chemistry Chemical Physics*, 23(9), 5199–5206. <https://doi.org/10.1039/D0CP04833J>
- Li, N., Tao, S., Chen, Y., Niu, X., Onwudinanti, C. K., Hu, C., ... & Zhou, H. (2019). Cation and anion immobilization through chemical bonding enhancement with fluorides for stable halide perovskite solar cells. *Nature energy*, 4(5), 408-415.
- Jiang, J., Onwudinanti, C. K., Hatton, R. A., Bobbert, P. A., & Tao, S. (2018). Stabilizing lead-free all-inorganic tin halide perovskites by ion exchange. *The Journal of Physical Chemistry C*, 122(31), 17660-17667.



# ACKNOWLEDGEMENTS

It is no great revelation that a doctoral thesis has one author, but many creators. Although most adventures end up as pleasant memories, they are often as difficult as they are exhilarating, and at certain moments in the thick of it, progress is so slow as to seem entirely absent. I wish to express my gratitude to some of those who have helped me to make it to the end.

To Shuxia Tao, my supervisor, my heartfelt thanks, both for taking me on, and for making the Ph.D a truly enjoyable and educational experience. I am fortunate to have been a part of your research group, and I wish you ever greater success in your quest to finally figure out perovskites. I do not know what it is like to do a Ph.D research project without ever-present support and trust from one's supervisor, and now, fortunately, I shall never know!

I am grateful to my promotors, Vianney Koelman and Geert Brocks, for always giving me new perspectives. I see your influence on nearly every page of this book, and it is that much better for your efforts. It is, of course, a little intimidating to present one's work and ideas every other week to such a concentration of experience and expertise, but I always left the meetings with you and Shuxia having learned something, and one could not really ask for more.

Thank you, Thomas Morgan, my group leader at Plasma Materials Interactions. Despite the difference between my research and the group's fusion focus, and my inability to quote Stangeby at length – every PMI conversation apparently has to include at least one mention of Stangeby –, I benefited greatly from the meetings and discussions with you and the group.

I would like to thank the members of my doctoral committee, Professors Sofia Calero, Yves Ferro, Joost Frenken, and Kai Nordlund, for devoting their time to reading and evaluating my work.

To the people of DIFFER, thank you for making it such a wonderful place to work. To Jan-Willem, present at the very beginning and the very end, and at various points in between. To Marco de Baar, for your boundless cheer. To my fellow members of the OR past and present, for your earnest efforts towards continuous improvement.

To Maarten, Daniele, and Shih-Chi, the members of our DIFFER-ASML coterie, thank you for being among the select few who are genuinely interested in and knowledgeable about all things blistering. Our discussions always helped to nudge me in the right direction.

I am grateful to the members of the Materials Simulation and Modelling (MSM) group, and to its predecessor the Computational Materials Physics Group (CMPG) – Junke, Ze-

hua, Haibo, Qihua, Min, Sofia, Mike, Vicent. Thank you for your questions and answers, for patiently listening to a certain someone discussing ruthenium-hydrogen-tin ad nauseam, when all you really wanted to talk about was FA-MA-defects. It was a pleasure working alongside you all, not just a brain trust I could always access when I was stuck, but also friends in the true sense of the word.

To my paranymphs, Subash and Rucheet, thank you for your symbolic support on the day, and for your very real friendship for years before and, I hope, after.

Most of all, I am grateful to those who are closest to my heart, who have guided me, and made it so that all my life, I have never been alone. Thank you Mum and Dad, my first teachers and advisers, who fed my curiosity always, for your high expectations and unwavering belief. To my siblings, thank you for being such good examples, and for holding me up, no matter the distance across which you have to reach. To Vicki, who has been with me every step of the way, thank you for all the ways in which you enrich my life; this work would not exist without you.

# CURRICULUM VITÆ

Chidozie Onwudinanti was born on the 28<sup>th</sup> of January, 1982 in Umuahia, Nigeria. Having completed his schooling in 1998 at Suleja Academy in Suleja, Nigeria, he moved to Moscow, Russia, for higher education. He acquired his Bachelor (2005) and Master (2008) degrees in Electrical and Electronic Engineering from the Moscow Power Engineering Institute on a Federal Government scholarship. After spending several years employed as a tutor, translator, and teacher of English as a foreign language, he relocated to the Netherlands, where in 2015 he completed a Master degree programme in Sustainable Energy Technology at the Delft University of Technology. His Master's research project was an investigation of nanostructures for light management in CIGS photovoltaic devices. In 2017, he started a PhD research project at the Dutch Institute for Fundamental Energy Research (NWO-I DIFFER) in Eindhoven, the Netherlands. The results of the doctoral research are presented in this dissertation.